

UNIVERSIDADE FEDERAL DO ESPÍRITO SANTO
PROGRAMA DE PÓS GRADUAÇÃO EM ENGENHARIA MECÂNICA

**A TWO-PHASE FLOW CIRCUIT CHARACTERIZATION BY PRESSURE DROP
MECHANISTIC MODELS, IMAGE PROCESSING TECHNIQUE AND FLOW
PATTERN MAPPING**

TIAGO GUERZET SARDENBERG LIMA

Vitória

2022

TIAGO GUERZET SARDENBERG LIMA

**TWO-PHASE FLOW CIRCUIT CHARACTERIZATION BY PRESSURE DROP
MECHANISTIC MODELS, IMAGE PROCESSING TECHNIQUE AND FLOW
PATTERN MAPPING**

A dissertation submitted in partial fulfilment of the requirements for the degree of Master of Science in Mechanical Engineering.

Supervisor: Professor Rogério Ramos

Co-supervisor: Professor Francisco Júlio do Nascimento

Vitória

2022

Ficha catalográfica disponibilizada pelo Sistema Integrado de Bibliotecas - SIBI/UFES e elaborada pelo autor

L732t lima, tiago guerzet sardenberg, 1994-
Two-phase flow circuit characterization by pressure drop mechanistic models, image processing technique and flow pattern mapping / tiago guerzet sardenberg lima. - 2022.
119 f. : il.

Orientador: Rogério Ramos.
Coorientador: Francisco Júlio do Nascimento.
Dissertação (Mestrado em Engenharia Mecânica) -
Universidade Federal do Espírito Santo, Centro Tecnológico.

1. Multiphase flow. 2. Pressure drop. 3. Mechanistic models. 4. Image processing techniques. 5. Two-phase flow modeling. 6. Flow pattern map. I. Ramos, Rogério. II. do Nascimento, Francisco Júlio. III. Universidade Federal do Espírito Santo. Centro Tecnológico. IV. Título.

CDU: 621



PROGRAMA DE PÓS-GRADUAÇÃO EM ENGENHARIA MECÂNICA
CENTRO TECNOLÓGICO
UNIVERSIDADE FEDERAL DO ESPÍRITO SANTO

A TWO-PHASE FLOW CIRCUIT CHARACTERIZATION BY PRESSURE DROP MECHANISTIC MODELS, IMAGE PROCESSING TECHNIQUE AND FLOW PATTERN MAPPING

TIAGO GUERZET SARDENBERG LIMA

COMISSÃO EXAMINADORA

Prof. Dr. Rogério Ramos
Orientador PPGEM/UFES

Prof. Dr. Francisco Júlio do Nascimento
Coorientador UNIFESP

Prof. Dr. Renato do Nascimento Siqueira
Examinador Interno – PPGEM/UFES

Prof. Dr. Ramon Silva Martins
Examinador Externo – DEM/UFES

Dissertação apresentada ao Programa de Pós-Graduação em Engenharia Mecânica da Universidade Federal do Espírito Santo como parte dos requisitos necessários à obtenção do título de Mestre em Engenharia Mecânica

Vitória (ES), 01 de agosto de 2022.





Aprovação banca TIAGO GUERZET SARDENBERG LIMA

Data e Hora de Criação: 01/08/2022 às 16:20:27

Documentos que originaram esse envelope:

- Aprovação banca TIAGO GUERZET SARDENBERG LIMA.pdf (Arquivo PDF) - 1 página(s)
- Ata 306 Tiago Guerzet Sardenberg Lima.pdf (Arquivo PDF) - 1 página(s)
- Questionário CAPES - Tiago Guerzet Sardenberg Lima.pdf (Arquivo PDF) - 2 página(s)



Hashs únicas referente à esse envelope de documentos

[SHA256]: 87a637c5c02b97fa193f56a97fdbbf6e268cdb61a913bb35fe711990d5223352

[SHA512]: 6e42f7d43fac5ccae56b6f2143092ebcf3dde638858ea9e2229fe3a15487588c15e28a9d79c1690bb45d788ac6df9eb9a0272007ed5afabedbee8693773b1cf6

Lista de assinaturas solicitadas e associadas à esse envelope



ASSINADO - Ramon Silva Martins (ramon.martins@ufes.br)

Data/Hora: 01/08/2022 - 16:37:54, IP: 177.104.235.70

[SHA256]: f493731ceafee93e6a8647061b8a463a7cffd96091fd412511584db63fd22dec



ASSINADO - Renato do Nascimento Siqueira (renatons.ifes@gmail.com)

Data/Hora: 01/08/2022 - 21:02:38, IP: 186.10.248.42

[SHA256]: ba6ef88f7d5e64ba6e5ad3dc9b32cfd74f46cdd34e78e2d86ae0c528d91e448f



ASSINADO - Francisco Julio do Nascimento (fjascimento@unifesp.br)

Data/Hora: 02/08/2022 - 07:39:44, IP: 191.0.16.46

[SHA256]: 9faed72bf6a9eb2634650d0bc4b53e232c0e072dbb09a62d4d45105c3b4ef153



ASSINADO - Rogerio Ramos (rogerio.ramos@ufes.br)

Data/Hora: 02/08/2022 - 09:33:40, IP: 200.137.65.104

[SHA256]: 7b663033caca9a01ab1c9a769db7f1485c89a46eb51695d2179a526fd52a9814

Histórico de eventos registrados neste envelope

02/08/2022 09:33:40 - Envelope finalizado por rogerio.ramos@ufes.br, IP 200.137.65.104

02/08/2022 09:33:40 - Assinatura realizada por rogerio.ramos@ufes.br, IP 200.137.65.104

02/08/2022 09:33:16 - Envelope visualizado por rogerio.ramos@ufes.br, IP 200.137.65.104

02/08/2022 07:39:44 - Assinatura realizada por fjascimento@unifesp.br, IP 191.0.16.46

01/08/2022 21:02:38 - Assinatura realizada por renatons.ifes@gmail.com, IP 186.10.248.42

01/08/2022 16:37:54 - Assinatura realizada por ramon.martins@ufes.br, IP 177.104.235.70

01/08/2022 16:25:35 - Envelope registrado na Blockchain por rogerio.ramos@ufes.br, IP 200.137.65.104

01/08/2022 16:25:32 - Envelope encaminhado para assinaturas por rogerio.ramos@ufes.br, IP 200.137.65.104

01/08/2022 16:20:31 - Envelope criado por rogerio.ramos@ufes.br, IP 200.137.65.104

ACKNOWLEDGEMENTS

I would like to devote this work to the scientific community and to the achievement and opportunity of accomplishing a Master's degree.

I am extremely grateful for all the support provided by my parents, Eduardo and Rita, during this journey, you are quite examples of amazing human beings. Also, gratitude is the correct word for my partner Maria Alice for the endless days and nights of brainstorming and studying that she witnessed and assisted. Without those ones, I am sure that I could not be where I am today.

Not last, but I also would like to thank my entire family and long date friends for always being there and never skip a good discussion. You are surely responsible for what I have become.

I would also like to say thanks for my supervisor, Professor Rogério Ramos, for giving me the opportunity of doing a research degree and always providing all necessary equipment and support for any situation. Even when something went wrong or appeared to be difficult, he could manage to quickly find a solution. Additionally, I thank my co-supervisor, Professor Francisco, for all the hours of discussion and developments we shared. Even though we did not personally meet until this date, he always made himself present and willing to help in any situation. Both of you represent a fundamental part of all I have achieved here.

I would like to thank my research partners and friends Renan, Ligia, Marciellyo, Filipe, Ulysses and Lucca. I am sure that all our discussions and groupwork were crucial for the development of many tools and results here presented. From a code development to a multiphase flow circuit setup, you were there and helped me with all I needed. Also, I am grateful for the support of Maurício and 2Solve team in making the circuit operational and for the disposal to solve any emergent problem.

At last, my gratitude to CAPES for the scholarship awarded, especially during the pandemic moment, to PPGEM for the great Master's degree course, and to the Professors for all knowledge shared.

ABSTRACT

Two-phase flow phenomenon is considerably present in many industry sectors and plays an important role in multiple operations, processes and equipment projecting. Literature has shown that modeling these occurrences is not completely well understood and it is still a technological and conceptual challenge. In this way, predictions of flow pattern and friction loss are compared with visual observations and meters' measurements, considering also an extensive bibliographic review on models for predicting patterns and behavior of multiphase flows. Further, such development is applied aiming to estimate the operational envelop of NEMOG's multiphase flow circuit. A set of experiments is planned to verify the real operational capacity of the facility and results are further compared to predictions provided by models. In parallel, an image processing algorithm is developed to identify the liquid height through high-frame rate video recordings of a translucent test's section. Using a selected region of interest, the output of liquid plug height over time is then used to calculate the gas velocity by two different approaches for intermittent flow patterns: geometrical and frequency shift. Furthermore, single-sided amplitude spectrum and power spectral density are studied in order to supply an additional tool to evaluate flow patterns. Capabilities and limitations of the algorithm are discussed, and possible future developments are indeed suggested. This study concluded that, selected mechanistic models are quite capable of providing an estimation of present flow patterns and pressure drop. However, localized pressure drop is not considered in these models, and it may be an issue for certain facilities. The image processing algorithm performed well for definite intermittent pattern and is a valid approach for collecting additional information of a two-phase flow. Situations in which the flow is not intermittent or liquid fraction and Reynolds number is high, represented a challenge to be overcome. Lastly, amplitude spectrum is considered an additional tool to identify two-phase flow patterns based on higher amplitude frequencies.

Keywords: Multiphase flow, mechanistic model, two-phase flow modeling, pressure drop, flow pattern map, high-speed video, image processing, spectral analysis.

RESUMO

O fenômeno de escoamento bifásico é consideravelmente presente em diversos setores da indústria e representa um fator de importância em operações, processos e projetos de equipamentos. A literatura tem mostrado que modelar a ocorrência desse tipo de escoamento ainda não é completamente compreendido e é um desafio tecnológico e conceitual. Dessa forma, previsões de padrão de escoamento e perda de carga são comparadas com observações visuais e medições realizadas, considerando também uma extensiva revisão bibliográfica de modelos utilizados para previsão de padrões e comportamento do escoamento multifásico. Além disso, o presente desenvolvimento é utilizado para estimar o envelope operacional do circuito multifásico do NEMOG. Uma bateria de experimentos é planejada para verificar a real capacidade da instalação e os resultados são comparados com as previsões obtidas ao utilizar os modelos em questão. Em paralelo, um algoritmo de processamento de imagem é desenvolvido com o objetivo de identificar o nível de líquido por meio de vídeos de alta velocidade de uma seção translúcida do circuito de testes. Utilizando a seleção de uma região de interesse, o dado de saída contendo a altura do líquido ao longo do tempo é então usado para calcular a velocidade do gás por duas diferentes abordagens: geométrica e por defasagem de sinais. De maneira complementar, o espectro de amplitude unilateral e a densidade espectral de potência são estudados com o intuito de obter ferramentas adicionais para avaliar os padrões de escoamento. Capacidade e limitações do algoritmo são discutidos e possíveis futuros desenvolvimentos são sugeridos. O presente estudo concluiu que os modelos mecanicistas selecionados são consideravelmente capazes de fornecer uma estimativa de padrões de escoamento e perda de carga. Porém, as perdas de carga localizadas não são consideradas nesses modelos e isso pode representar uma desvantagem a depender da instalação a serem aplicados. O algoritmo de processamento de imagem teve um bom desempenho para o padrão de escoamento intermitente, se bem definido, e representa uma abordagem válida para coletar informações adicionais do escoamento. Situações em que o padrão de escoamento difere de intermitente ou em que a fração de líquido e número de Reynolds são elevados, representam um fator a ser futuramente desenvolvido. Por fim, o espectro de amplitude foi considerado como uma ferramenta adicional para identificar padrões de escoamento bifásico baseado nas frequências correspondentes aos eventos de maiores amplitudes.

LIST OF FIGURES

Figure 1 – Classical vertical upward flow patterns according to Hewitt and Hall-Taylor (1970).	22
Figure 2 – Vertical downward flow patterns according to Barnea et al. (1982).	23
Figure 3 – Horizontal flow patterns according to Taitel and Dukler (1976).....	24
Figure 4 – Horizontal flow pattern map comparison of theory (defined by lines) and experiment (//////) as published in Taitel and Dukler (1976) . Water-air at $T = 25^{\circ}\text{C}$, $P = 1 \text{ atm}$ and $D = 2.5$ cm.....	29
Figure 5 – Flow pattern determination algorithm based on Taitel and Dukler (1976).	36
Figure 6 – Flow pattern determination algorithm inspired by Petalas and Aziz (2000).	37
Figure 7 – Overview of NEMOG’s multiphase flow closed loop.....	41
Figure 8 – NEMOG’s test section and experimental setup. (1-5) Differential pressure transducers, (2) high-speed camera, (3) translucent section, (4) manometric pressure transducer and (6) thermocouple.	42
Figure 9 – Sketch of high-speed camera installation in NEMOG multiphase flow circuit.	46
Figure 10 – High-speed camera used in the experiment: <i>Hot Shot 512 SC</i> camera (NAC IMAGE TECHNOLOGY, 2006).	46
Figure 11 – Comparison between selected color contrast on a frame.	48
Figure 12 – Binarized image.	48
Figure 13 – Non-treated RGB frame and ROI’s location.	49
Figure 14 – Comparison between height’s output and real video.	49
Figure 15 – Cross section geometrical approach scheme.	50
Figure 16 – Comparison of current implementation represented by colored dots and author’s provided data identified by boundary lines (TAITEL; DUKLER, 1976).	53
Figure 17 – Comparison of current implementation represented by colored dots and author’s provided data identified by boundary lines (PETALAS; AZIZ, 2000).	54
Figure 18 – Xiao et al. (1990) model’s predictions compared with experimental data by Payne et al. (1979). (a) Full databank, (b) Stratified wavy flow pattern, (c) Intermittent flow pattern, (d) Annular-dispersed liquid flow pattern.	55
Figure 19 – Petalas and Aziz (2000) model’s predictions compared with experimental data by Payne et al. (1979). (e) Full databank, (f) Stratified wavy flow pattern, (g) Intermittent (EB and S) flow pattern and (h) Annular-mist flow pattern.	56
Figure 20 – Single-phase pressure drop measurements compared to calculated pressure drop.	57
Figure 21 – Calculated pressure drop at $P = 270 \text{ kPa}$ by the model of Xiao et al. (1990) for all pairs of superficial velocities.	59

Figure 22 – Calculated pressure drop at $P = 485$ kPa by the model of Xiao et al. (1990) for all pairs of superficial velocities.	60
Figure 23 – Calculated pressure drop at $P = 700$ kPa by the model of Xiao et al. (1990) for all pairs of superficial velocities.	60
Figure 24 – Calculated pressure drop at $P = 270$ kPa by model the of Petalas and Aziz (2000) for all pairs of superficial velocities.....	61
Figure 25 – Calculated pressure drop at $P = 485$ kPa by the model of Petalas and Aziz (2000) for all pairs of superficial velocities.....	61
Figure 26 – Calculated pressure drop at $P = 700$ kPa by the model of Petalas and Aziz (2000) for all pairs of superficial velocities.....	62
Figure 27 – NEMOG’s envelop at $P = 270$ kPa for experimental points 1 to 9. Flow pattern map based on Taitel and Dukler (1976) and friction loss on Xiao et al. (1990).....	63
Figure 28 – NEMOG’s envelop at $P = 485$ kPa for experimental points 10 to 18. Flow pattern map based on Taitel and Dukler (1976) and friction loss on Xiao et al. (1990).....	64
Figure 29 – NEMOG’s envelop at $P = 700$ kPa for experimental points 19 to 27. Flow pattern map based on Taitel and Dukler (1976) and friction loss on Xiao et al. (1990).....	64
Figure 30 – NEMOG’s envelop at $P = 270$ kPa for experimental points 1 to 9. Flow pattern map based on Petalas and Aziz (2000).	65
Figure 31 – NEMOG’s envelop at $P = 485$ kPa for experimental points 10 to 18. Flow pattern map based on Petalas and Aziz (2000).	65
Figure 32 – NEMOG’s envelop at $P = 700$ kPa for experimental points 19 to 27. Flow pattern map based on Petalas and Aziz (2000).	66
Figure 33 – Overall pressure drop predictions in comparison to measured values, considering all experimental points. Data segmentation according to mechanistic model and predicted flow pattern.	69
Figure 34 – Pressure drop relative error of Petalas and Aziz (2000) and Xiao et al. (1990) models predictions compared to experimental measurements.....	70
Figure 35 – Pressure drop at $P = 270$ kPa.	71
Figure 36 – Pressure drop at $P = 485$ kPa.	72
Figure 37 – Pressure drop at $P = 700$ kPa.	73
Figure 38 – Pressure drops at same superficial velocities. A) $JG = 2.53$ m/s and $JL = 0.27$ m/s. B) $JG = 2.43$ m/s and $JL = 3.00$ m/s. C) $JG = 4.83$ m/s and $JL = 0.27$ m/s. D) $JG = 4.75$ m/s and $JL = 2.98$ m/s.....	73
Figure 39 – Comparison of measured pressure drop considering same superficial velocities at different absolute pressure P	74
Figure 40 – Evaluation of signal shift and gas velocity over distance.	76
Figure 41 – Height over time (red line) and video integration (background) comparison for selected experimental points (Table 12).....	80

Figure 42 – Comparison of measured liquid height respectively by ROI A (red) and B (blue) at a distance of 2D.....	82
Figure 43 – Binary liquid height representing slug passage from ROI A and B.....	83
Figure 44 – Single-sided amplitude spectrum of hi using FFT tool on MATLAB (2019). Higher amplitude events located at lower frequencies in experimental points 19, 30, 32, 28 and 10 in agreement with lower number of slug passages.	85
Figure 45 – Power spectral density PSD of hi processed on MATLAB (2019) using single-sided amplitude spectrum.	87
Figure 46 – Linear adjustment applied to liquid phase superficial velocity and measured pressure drop.....	89
Figure 47 – Gas and liquid superficial velocities influence on pressure drop and flow pattern.	90
Figure 48 – Slug frequency influence on measured pressure drop.....	91
Figure 49 – PCA analysis in terms of observed flow pattern classification and its influence on data variance mostly indicated by PC_1 (S and SW) and PC_2 (AD).....	92
Figure 50 - PCA analysis in terms of ranges of measured pressure drop and its influence on data variance mostly indicated by PC_1	92
Figure 51 - PCA analysis in terms of measured slug frequency and its influence on data variance mostly indicated by PC_1	93
Figure 52 - PCA analysis in terms of liquid superficial velocity ranges and its influence on data variance mostly indicated by PC_1	93
Figure 53 - PCA analysis in terms of gas superficial velocity ranges and its influence on data variance mostly indicated by PC_2	94

LIST OF TABLES

Table 1 – Multiphase flow mechanistic models applicable to predict flow pattern map or pressure drop in non-specific configurations (straight tubes).....	31
Table 2 – Conditions used to generate flow pattern map of Taitel and Dukler (1976).....	35
Table 3 – Conditions used to generate flow pattern map of Petalas and Aziz (2000).	36
Table 4 – Operational conditions based on NEMOG’s facility capacity.	39
Table 5 – Example of factorial central compost planning.	44
Table 6 – Example of factorial planning.	45
Table 7 – Pressure drop measurement for single-phase validation and pressure transducer uncertainty.	58
Table 8 – Flow pattern map prediction by models and visual classification.	67
Table 9 – Error and standard deviation of experimental points 28 - 39.....	74
Table 10 – Averaged absolute relative error and error standard deviation segmented on flow pattern determined by mechanistic models.	75
Table 11 – Averaged absolute relative error and error standard deviation based on models’ flow pattern predictions in agreement with observations.	76
Table 12 – Selected experimental points based on accuracy criteria (E_{VGS}).....	78
Table 13 – Frequency in which largest amplitude waves occur by <i>FFT</i>	86

LIST OF SYMBOLS

Abbreviations

A	Annular
AD	Annular dispersed liquid
AM	Annular mist
B	Bubble
CFD	Computer fluid dynamics
CH	Churn
CNPq	Conselho Nacional de Desenvolvimento Científico e Tecnológico
DB	Dispersed Bubble
EB	Elongated Bubble
F	Froth
FFT	Fast Fourier Transform
I	Intermittent
NEMOG	Núcleo de Estudos em Escoamentos de Óleo e Gás
PSD	Power spectral density
ROI	Region of interest
S	Slug
SS	Stratified smooth
SW	Stratified wavy

Latin Symbols

A	Pipe cross section area [m ²]
D	Internal diameter [m]
E	Absolute relative error [%]
e_w	Absolute pipe roughness [m]
f	Friction factor
FE	Entrainment fraction

g	Gravity's acceleration [m/s^2]
h	Liquid height [m]
J	Mixture superficial velocity [m/s]
M	Mass flow rate [kg/h]
P	Pressure [Pa]
Q	Volumetric flow rate [m^3/h]
R	Universal gas constant [$\text{J}\cdot\text{kg}^{-1}\cdot\text{K}^{-1}$] or linear cross-correlation coefficient
Re	Reynolds number
s	Sheltering coefficient
S	Perimeter [m]
T	Temperature [$^{\circ}\text{C}$]
V	Velocity [m/s]
Y	Amplitude of Fourier transform [m]
ΔP	Differential pressure or pressure drop [Pa]

Greek Symbols

α	Volumetric fraction
δ	Liquid film thickness on annular flow [m]
θ	Pipe slope [$^{\circ}$]
μ	Dynamic viscosity [Pa.s]
ρ	Density [kg/m^3]
σ	Water superficial tension [N/m]
τ	Shear stress [Pa]

Subscripts and Superscripts

0	Absolute
c	Referred to the core region on annular flow
f	Referred to the film region on annular and intermittent flows
G	Gas phase

G_h	Calculated by geometrical approach
G_s	Calculated by frequency shift approach
i	Interfacial or variable's index
L	Liquid phase
M	Mixture
V_{Gs}	Related to gas velocity obtained from frequency shift and geometrical approach
w	Referred to the pipe's wall
WG	Wall-gas
WL	Wall-liquid

CONTENTS

ACKNOWLEDGEMENTS.....	VI
ABSTRACT.....	VII
RESUMO.....	VIII
LIST OF FIGURES.....	IX
LIST OF TABLES.....	XII
LIST OF SYMBOLS.....	XIII
1 INTRODUCTION.....	18
1.1 MOTIVATION.....	18
1.2 OBJECTIVE.....	20
2 BIBLIOGRAPHIC REVIEW.....	20
2.1 MULTIPHASE FLOW.....	21
2.2 EMPIRICAL AND SIMPLIFIED MODELS: TWO-PHASE MULTIPLIER.....	27
2.3 MECHANISTIC MODELS FOR FLOW PATTERN AND PRESSURE DROP.....	28
2.4 IMAGE PROCESSING TECHNIQUES APPLIED TO MULTIPHASE FLOW.....	31
2.5 OUTCOMES.....	34
3 MATERIALS AND METHODS.....	34
3.1 IMPLEMENTATION AND VALIDATION OF MECHANISTIC MODELS.....	34
3.2 NEMOG'S MULTIPHASE FLOW CIRCUIT ENVELOPE ESTIMATION.....	38
3.3 EXPERIMENTAL CIRCUIT SETUP.....	40
3.4 SINGLE PHASE FRICTION LOSS VALIDATION.....	42
3.5 TEST'S MATRIX.....	43
3.6 VIDEO RECORDING SETUP.....	45
3.7 VISUAL CLASSIFICATION PARAMETERS.....	46
3.8 IMAGE PROCESSING ALGORITHM.....	47
3.9 OUTCOMES.....	52
4 RESULTS AND DISCUSSION.....	53
4.1 VALIDATION OF MECHANISTIC MODELS CODE.....	53
4.2 SINGLE-PHASE VALIDATION OF PRESSURE DROP MEASUREMENTS.....	57
4.3 ESTIMATED AND ACTUAL OPERATIONAL RANGE OF NEMOG'S MULTIPHASE FLOW CIRCUIT.....	59
4.4 FLOW PATTERN MAP: VISUAL CLASSIFICATION AND PREDICTIONS PROVIDED BY MODELS.....	66
4.5 TWO-PHASE FRICTION LOSS: COMPARISON BETWEEN MEASUREMENTS AND PREDICTIONS.....	68
4.6 CODE PARAMETERS PERFORMANCE FOR IMAGE PROCESSING IN TERMS OF FREQUENCY SHIFT TECHNIQUE.....	76
4.7 ROI OUTPUT.....	77
4.8 STATISTICAL PARAMETERS EVALUATION.....	89

5 CONCLUSION	94
5.1 FINAL CONSIDERATIONS	94
5.2 FUTURE PERSPECTIVES.....	96
6 REFERENCES	98
7 APPENDIX	103

1 INTRODUCTION

1.1 MOTIVATION

Two-phase flow occurrence is a phenomenon that happens commonly but is not always noticed during a daily routine of many people. Furthermore, numerous industry sectors count on multiphase flow for operations, modeling and projecting new components. According to Taitel and Barnea (2015), equipment such as heat exchangers depends on the occurrence of liquid and gas phases to properly work being considered useful and quite present on industry processes. These machineries are essential for nuclear reactors, climate control in space vehicles, solar energy, and geothermal power plants. Not only in industry but, micro electronic devices, coffee percolator, brew gasification are also examples of a two-phase flow presence at a non-industrial site.

Considering oil and gas transport, its production depends on the capacity of pumping two or more phases over long distances. For example, an offshore production system requires that phases flow through a wellbore from the reservoir to the platform. It is also important to notice that such processes may have considerable variations in pressure and temperature, therefore, phase changes may occur. Consequently, in order to design, operate and develop prevention routines for these plants, it is essential to predict flow characteristics, estimate fluid properties and account for possible phenomena.

As reported by Wallis (1969), over half of all chemical engineering is concerned with multiphase flows. It means that security and performance of many industrial processes, such as desalination, depends directly on the two-phase fluids applied technology. Furthermore, pollution of distinct natures may occur due to poor predictions of two-phase flows in industries as food processing, papermaking, and steelworks. These types of pollution are indeed contaminants that can exist on air, water and food.

In terms of single-phase fluid dynamics, it is possible to consider this subject relatively well understood. On the other hand, two-phase flow and thermo-fluid dynamics may be an order of magnitude more complex, according to Ishii and Hikibi (2011). As a result, due to the high industry demand and materiality upon events related to multiphase flows, several efforts have been made to derivate correspondent formulations based on fundamental physical principles. These formulations are studied with the objective of composing mechanistic and computational models that can, accurately, represent the flow itself, describe interfacial transfer, morphological structures and provide predictive tools (ISHII; HIKIBI, 2011).

Considering mechanistic models, it is usually necessary to numerically solve a one-dimensional momentum equation to obtain valid predictions about the flow, including void fraction, instantaneous velocity of each phase, flow pattern and pressure

drop. However, solving these equations require certain computational effort and empirical correlations as closure models. In this way, properties of multiphase flow and the spatial phase distribution must be well known containing a large amount of valid data. Therefore, the development and use of instrumentation capable of measure parameters of two-phase flows is a critical aspect to be disclosed.

Since the complexity of multiphase flows are elevated and this is an actual subject for industries, study and experiment different configurations is quite relevant to improve the understanding of these events. Furthermore, experimental data can be used to verify analytical solutions, discover new phenomena, compose empirical correlations and supply relevant information for CFD simulations. In particular, gas-liquid flow occurrences seems to compose a large industry demand for pipeline transportation of gas and oil mixtures and in the flow of steam and water in boiler tubes, steam generators and in boiling water reactors (ROUHANI; SOHAL, 1983). In this way, it can be understood that two-phase flows compose an important subtopic of the multiphase flow study.

According to Jerez-Carrizales et al. (2015), during the period between 1950 and 1975 some of the first empirical correlations applied to two-phase flows were developed based on a few experiments on laboratories and fields. As a result, predictive tools for flow pattern and pressure drop started to be adopted by industries and tested by researchers. Later, more experiments were carried out with improved instruments, and physics involved in two-phase flow was better understood, resulting in the development of mechanistic models. In general, the knowledge regarding two-phase flows seems to be associated with the interaction between experimental results and theoretical approach.

Given this scenario, two-phase flow experiments are carried out in a multiphase flow circuit constructed in the facility of the Research Group for Studies on Oil&Gas Flow and Measurement (NEMOG). The circuit is tested for the first time and uses a gas-liquid flow mixture. Additionally, as an experimental facility, it is designed to work within a theoretical operational range, which limits the maximum and minimum values for flow rates and absolute pressure. Therefore, the first characterization of the actual operational range of the circuit and comparison with predictions obtained using mechanistic models found in the literature is of great importance for future developments that will use the facility as a source of experimental data. Lastly, obtained results can be used to verify the performance of mechanistic models and to develop tools to study two-phase flows.

1.2 OBJECTIVE

General objectives

The general objective of this work is the study of two-phase flow, containing air and water, on the multiphase flow circuit of NEMOG's facility (Research Group for Studies on Oil&Gas Flow and Measurement - NEMOG, in Portuguese), located at Federal University of Espírito Santo, Vitória, Brazil. Additionally, mechanistic models and facility equipment are tested against different experimental configurations to evaluate its feasibility and efficiency.

Specific objectives

Concerning the main objective of this work, it is necessary to point out and accomplish specific objectives as listed below.

- Selection of mechanistic models for two-phase flow pattern and pressure drop predictions (at least two models of each), based on a literature review.
- Implementation and validation of flow pattern map and friction loss selected models.
- Estimation of NEMOG'S multiphase flow circuit operational envelope using facility's limiting aspects and friction loss predictions provided by selected mechanistic models.
- Performance evaluation of mechanistic models compared to experimental measurements of pressure drop and observed flow patterns.
- Maturation, validation, and implementation of image processing algorithm applied to recorded videos.

2 BIBLIOGRAPHIC REVIEW

Prediction of multiphase flow properties has been an important task for many industry fields and technologies. To this extent, it is objectified to select best mechanistic models based on a literature review, which predictions it can supply in horizontal configurations and reported accurate results. In a complementary way, the literature of optical instrumentation capable of measuring properties of the flow is explored in order to develop an image processing algorithm that aggregate more data analysis to this work.

2.1 MULTIPHASE FLOW

In a general context, multiphase flows can be found in nature in many forms. Fog, smoke, smog, rain, clouds, snow, icebergs, quicksand, dust storms, mug, boiling water, egg scrambling, mayonnaise, beer and jam are examples of two-phase systems given by Wallis (1969) . Biological fluids also include two-phase flows such as blood, semen, and milk. Considering processes, fire extinguishers aerosols, fires, automobile engines, rockets, refrigeration cycles, soil erosion, physics of clouds, rain droplets, ice formation, landslides and snowslides can be taken as multiphase processes (ISHII; HIKIBI, 2011).

According to Wallis (1969), it is said that essentially all systems and components listed above can be modelled with the same physical laws of mass transport, momentum and energy. Considering that two-phase flows are widely present in different sectors, describing these events are concerns of environmental solutions and predictions, efficiency and safety of processes for engineering, and economical aspects.

Definition

To define a multiphase flow, it is important to account for the combinations of phases present in the mixture. Restricting it to combinations of two immiscible phases and following the lead of Wallis (1969), it is possible to define as two-phase flows:

- Gas – solid mixture.
- Gas – liquid mixture.
- Liquid – solid mixture.
- Immiscible liquid – liquid mixture.

In this way, in this text, it is adopted that a multiphase flow is a combination of gas-liquid mixture of immiscible phases, forming an interface between the flowing fluids.

Flow patterns

Two-phase flows can be classified by different interface configurations. These configurations are defined differently depending on the author, slope, and pipe diameter. In this section, basic flow pattern classification will be detailed according to the literature. However, different authors may consider subdivisions of a single pattern into two or more configurations.

For upward vertical configurations, Hewitt and Hall-Taylor (1970) designated four basic patterns according to Figure 1.

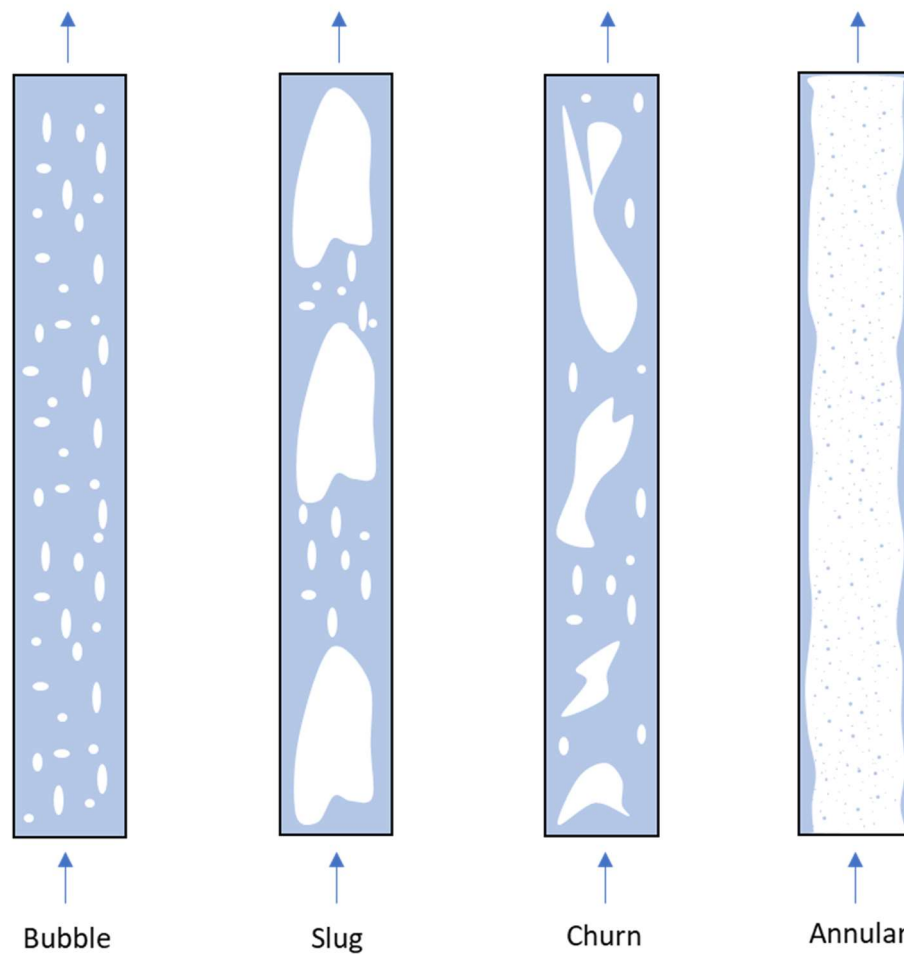


Figure 1 – Classical vertical upward flow patterns according to Hewitt and Hall-Taylor (1970).

Following authors' classification, it can be defined some parameters for each flow pattern.

- Bubble: Small bubbles homogeneously distributed in a continuous liquid phase.
- Slug: Majority of gas volume is concentrated in large bubbles (approximately the diameter size) with a thin liquid film on the pipe wall. These large bubbles are also called as Taylor Bubbles and are separated of each other by a liquid region called slug. Also, slug region may present small and dispersed bubbles.
- Churn: This flow pattern is somewhat like slug flow. However, turbulence is a strong influence on avoiding bubble coalescence and breaking large bubbles. In sum, it is more chaotic with characteristic oscillatory motion of the flow.
- Annular: In this case, an important characteristic is the continuity of gas phase on the core of the pipe. Liquid phase is concentrated as a liquid film on the pipe wall and in form of small droplets entrained in the gas core.

Additionally, vertical downward flow patterns are shown in Figure 2 as defined by Barnea et al. (1982).

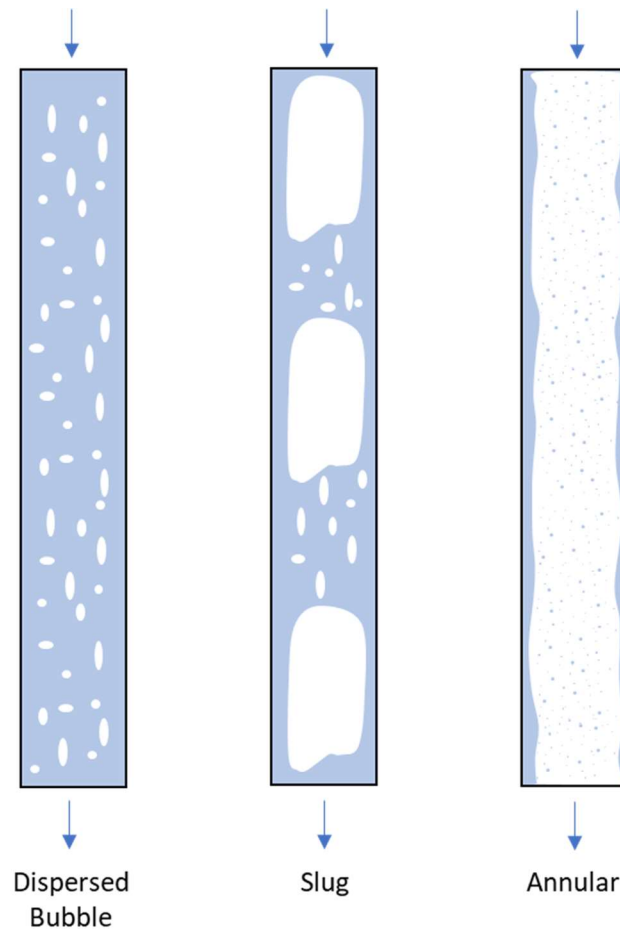


Figure 2 – Vertical downward flow patterns according to Barnea et al. (1982).

For this configuration, it is important to highlight that the buoyant force is acting against the flux for the gas phase and each flow pattern is explained as follows.

- Dispersed bubble: Turbulence intensity is highly elevated, liquid phase velocity is high enough to overcome buoyant forces and bubble coalescence, transporting dispersed bubbles downward.
- Slug: Some of the gas phase coalesces into large bubbles. These Taylor bubbles are transported downward. Dispersed bubbles may be present in the slug region.
- Annular: It can occur in two ways, the first consists of a falling liquid film on pipe wall and continuous core of gas with low volumetric flow. The second form takes place when the gas rate is high, and droplets permeates the core.

On the other hand, dealing with horizontal flows, new patterns emerge, and some may slightly change shape due to gravity acceleration and buoyancy factors. Classifications for this setup are given by Taitel and Dukler (1976) and detailed in Figure 3.

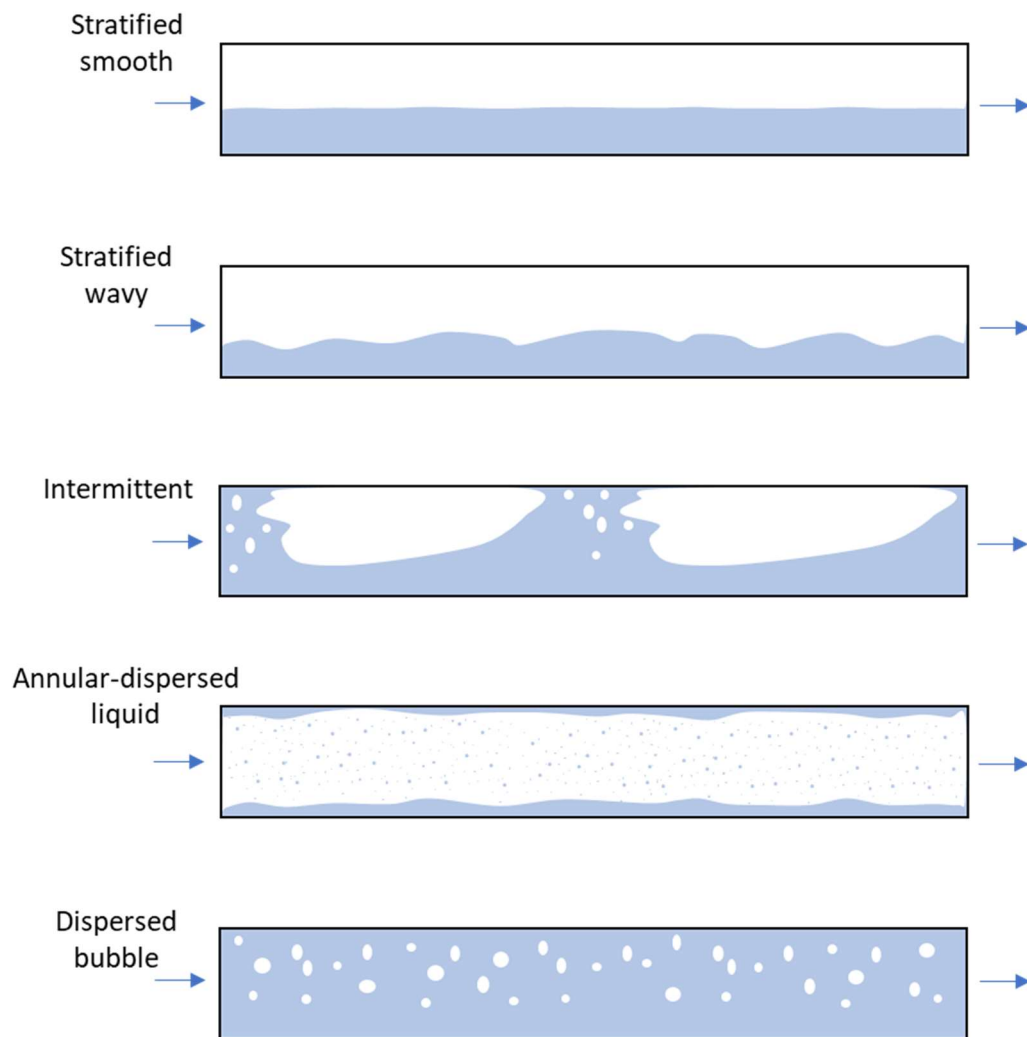


Figure 3 – Horizontal flow patterns according to Taitel and Dukler (1976).

In this way, it is pointed out:

- Stratified smooth: This regime is characterized by the gas phase (or lighter phase) flowing above the liquid (or heavier phase). Moreover, gas velocity is not fast enough to cause large perturbations on the interface.
- Stratified wavy: It has almost the same definition as the stratified smooth, nonetheless, gas velocity is sufficient to create perturbations and the formation of interfacial waves but does not reach the top of the pipe.
- Intermittent: Can be described quite like the slug flow on vertical configuration (which is an intermittent pattern). However, buoyancy tends to keep large bubbles on the top of the pipe. Both large bubbles and slug regions are inclined to occur with a periodic frequency.
- Annular-dispersed liquid: Composed of a liquid film attached on pipe wall and a core of gas and water droplets. Gravity acceleration influences the thickness of the film, even so, film region on the top is thinner and on the bottom is thicker.

- Dispersed bubble: Turbulence intensity is strong enough to break large bubbles and overcome buoyant forces, bubbles can be considered homogeneously distributed.

At last, considering that some authors may adopt different flow pattern definitions, it is relevant to point out additional regimes:

- Plug: This flow pattern consists in a portion of intermittent regime for vertical configurations, being characterized by the well definition of gas and liquid boundaries at low flow rates (TAITEL et al., 1980). For conditions where boundaries are less clear at higher flow rates, the intermittent flow pattern may be defined as slug.
- Elongated bubble: It is a portion of an intermittent flow pattern for both horizontal and vertical configurations, representing the regime in which the liquid slug contains no dispersed gas bubbles (PETALAS; AZIZ, 2000).
- Froth: Represents a transition zone between dispersed bubble and annular-mist, and between slug and annular mist flow regimes that occur in vertical and horizontal configurations (PETALAS; AZIZ, 2000).

Single-phase and multiphase friction loss

For single-phase flows, the frictional pressure drop is considerably well established and correlations for the friction factor are widely tested and validated. These correlations are based upon the relation of wall roughness, diameter, and Reynolds number. Examples of methods to calculate single-phase pressure drop are given by Darcy-Weisbach and Coolebrook-White apud Fox et al. (2014).

On the other hand, in terms of two-phase flows, more complex events should be considered. First, each phase can be partially in contact with the pipe wall and influence the value of the friction factor. Second, phases have an interface, and an interfacial friction factor may be necessary to account for. Additionally, according to literature review on multiphase flows done by Rouhani and Sohal (1983), wall roughness and friction in general can impact on flow pattern transitions. Consequently, it can lead to the selection of an erroneous method to calculate pressure drop if not correctly considered.

Basic definitions for two-phase flows

Basic definitions on the multiphase flow modeling, are defined by Wallis (1969) for both equations and notations basis. The first important variable to be detailed is the mixture superficial velocity or volumetric flux J , given by Equation 1. Also, Q_G and Q_L represents respectively the volumetric flow rate of the gas and liquid phase, while A is the cross-sectional pipe area.

$$J = \frac{Q_G + Q_L}{A} \quad (1)$$

Also, each phase has its own superficial velocity indicated by J_G and J_L , as demonstrated on Equations 2 and 3.

$$J_G = \frac{Q_G}{A} \quad (2)$$

$$J_L = \frac{Q_L}{A} \quad (3)$$

It is important to highlight that these definitions do not represent the *in-situ* phase velocity. The volumetric flow rate is divided by the entire area of the pipe, therefore superficial velocity is describing a volumetric flux. For this reason, Equations 4 and 5 take place, respectively, representing gas and liquid phases velocity by V_G and V_L .

$$V_G = \frac{Q_G}{A_G} \quad (4)$$

$$V_L = \frac{Q_L}{A_L} \quad (5)$$

Additionally, instantaneous volumetric fraction of phases, α_G and α_L , can be represented in a transversal section of the pipe by Equations 6 and 7, in which i is the index referred to one measurement or vector index.

$$\alpha_G^i = \frac{A_G^i}{A} \quad (6)$$

$$\alpha_L^i = \frac{A_L^i}{A} \quad (7)$$

The averaged value of volumetric fraction along a certain pipe length or over a specified time (on the same transversal section), where n is the number of equally spaced (in length or time) measurements and i is the index, can be calculated as:

$$\langle \alpha \rangle_G = \frac{1}{n} \sum_{i=1}^{i=n} \alpha_G^i \quad (8)$$

$$\langle \alpha \rangle_L = \frac{1}{n} \sum_{i=1}^{i=n} \alpha_L^i \quad (9)$$

As a result, considering above equations, it is convenient to represent gas and liquid velocity in terms of superficial velocity and averaged volumetric fraction.

$$V_G = \frac{J_G}{\langle \alpha \rangle_G} \quad (10)$$

$$V_L = \frac{J_G}{\langle \alpha \rangle_L} \quad (11)$$

Furthermore, some relevant properties of the mixture (or pseudo fluid) can be approximated using the volumetric fraction. In this way, it is given for mixture density ρ_m and mixture dynamic viscosity μ_m on Equations 12 and 13.

$$\rho_m = \rho_G \langle \alpha \rangle_G + \rho_L \langle \alpha \rangle_L \quad (12)$$

$$\mu_m = \mu_G \langle \alpha \rangle_G + \mu_L \langle \alpha \rangle_L \quad (13)$$

It should be highlighted that Equation 12 is capable of properly represent the mixture density considering an averaged phase volumetric fraction. Depending on the flow pattern, it may not describe the mixture density on a transversal section of the pipe. Additionally, Wallis (1969) explains that the virtual viscosity (or apparent viscosity) of a pseudo fluid is built upon the pattern, interfacial area and geometry of the flow, which means that one relation may not correctly represent the mixture viscosity for all studied situations. Consequently, many authors proposed different correlations in order to estimate the viscosity, including Cicchitti et al. (1960), Dukler et al. (1964a), Einstein (1906) and Mcadams et al. (1942). However, in selected multiphase flow models, Equation 13 is adopted by authors Petalas and Aziz (2000), Taitel and Dukler (1976) and Xiao et al. (1990).

2.2 EMPIRICAL AND SIMPLIFIED MODELS: TWO-PHASE MULTIPLIER

Before the development of a robust model capable of physically describe phases in different flow patterns, some authors based their work on establishing empirical correlations and tuning them by experimental data sets. One example is the work published by Lockhart and Martinelli (1949) that proposed a correlation capable of predicting pressure drop in horizontal two-phase flows. Later, Hoogendord (1959) developed correlations for flow pattern prediction, considering Lockhart-Martinelli parameter to calculate pressure drop of certain situations. Additionally, Hoogendord

(1959) highlighted that for some cases, the proposed correlation for pressure drop could not give precise predictions: if gas density differs from the atmospheric pressure on slug, plug and froth flow; for stratified and annular flows in general conditions.

Another work that investigated Lockhart-Martinelli correlation was developed by Hughmark and Pressburg (1961). The authors tested the horizontal correlation on a vertical experimental circuit. Conclusions suggested that data was not in agreement with predictions. As emphasized by Jerez-Carrizales et al. (2015), empirical correlations not necessarily have a physical basis, what can directly impact on practical situations that differs from the data set used for the adjustment of relations.

2.3 MECHANISTIC MODELS FOR FLOW PATTERN AND PRESSURE DROP

In a general way, a literature review presented by Jerez-Carrizales et al. (2015) highlighted that mechanistic models present a momentum balance equation for flow patterns separately and that the objective consists in predict one or more physical phenomenon related to a specific situation. These equations are based on the physics of the problem and fluid dynamics modeling, relying on empirical correlations as enclosing parameters. Additionally, to solve the equations, some models require a numerical method while others can be done by hand calculations (analytically).

The development of Taitel and Dukler (1976) may be one of the first works to present a complete mechanistic model capable of predicting two-phase flow patterns based on fluid properties, pipe diameter and superficial velocities. This model is based on the equilibrium of a stratified flow and a numerical solution of a two-phase momentum equation to obtain the liquid height. The algorithm for flow pattern determination relies on physical equilibrium premises and works for gas-liquid horizontal flows. Besides, flow patterns are classified as dispersed bubble (DB), intermittent (I), stratified smooth (SS), stratified wave (SW) and annular-dispersed liquid (AD), as shown in Figure 4.

In sequence, Taitel et al. (1980) developed a model applicable to steady upward gas-liquid flow in vertical tubes. This model is also based on physical mechanisms for flow pattern transition, however, does not need numerical calculations. Flow patterns are determined simply by algebraic equations and defined as: bubble (B), slug (S), dispersed bubble (DB), churn (CH) and annular (A). Considering vertical downward configurations, Barnea et al. (1982) presented a flow pattern map and proposed physical mechanisms for transition boundaries. This study emphasized the lack of investigations for gas-liquid mixtures in downward flows. Besides that, flow patterns were classified into annular (A), slug (S) and dispersed bubble (DB) based on visual observations.

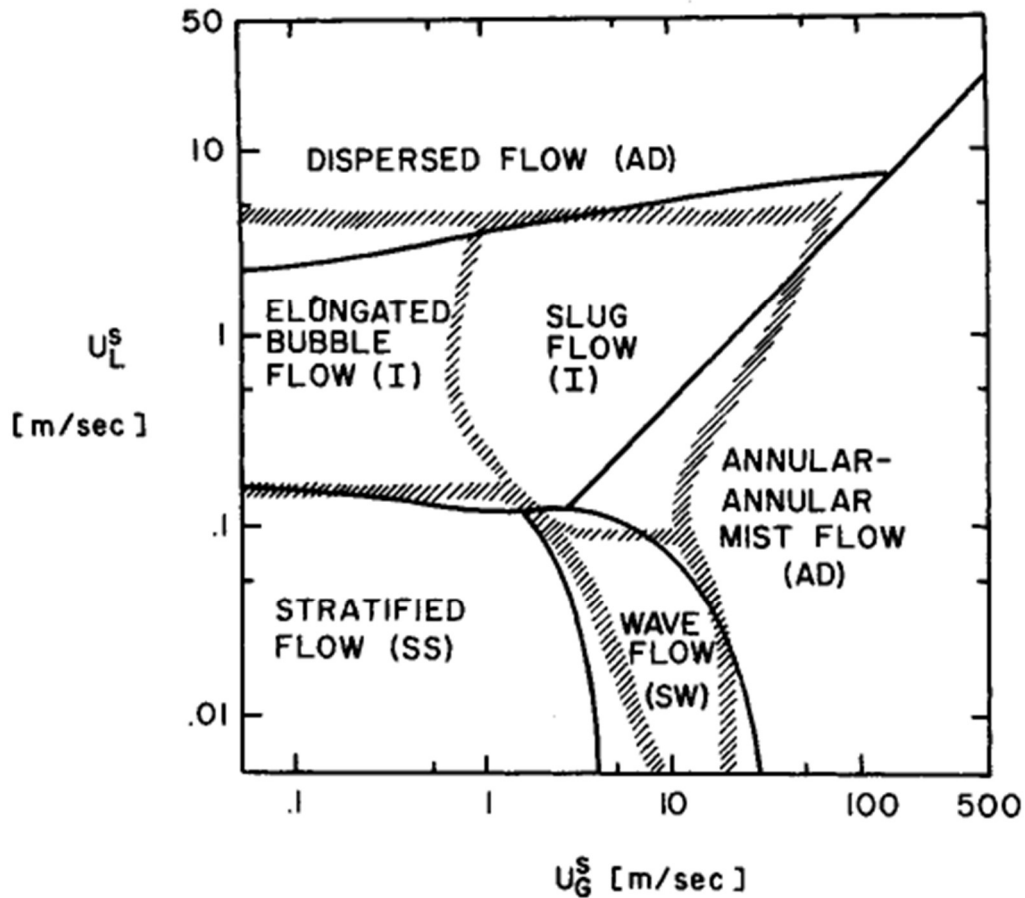


Figure 4 – Horizontal flow pattern map comparison of theory (defined by lines) and experiment (/////////) as published in Taitel and Dukler (1976) . Water-air at $T = 25^{\circ}\text{C}$, $P = 1 \text{ atm}$ and $D = 2.5 \text{ cm}$.

As authors tested existing models against experimental data, transition mechanisms were studied, enhanced and developed. In this way, McQuillan and Whalley (1985) modelled the transition between plug and churn patterns on upward vertical flow and modified the equation of stability for bubble flow presented by Taitel et al. (1980). These modifications were made accounting for possible errors on flow pattern map transition lines for different flow rates and pipe diameters with data provided by several authors.

Furthermore, since transition physical aspects may be different varying pipe slope and most of the data were presented on horizontal or vertical flow, Barnea et al. (1985) experimented and investigated flow pattern occurrence in ranges from 0° to 90° . Additionally, these authors proposed modifications to the models of (TAITEL et al., 1980; TAITEL; DUKLER, 1976) and extended predictions to upward inclined flows. Finally, Barnea (1987) constructed a general method to estimate the flow pattern for any slope.

Considering not only flow pattern predictions, Xiao et al. (1990) developed a mechanistic model capable of predicting friction losses for horizontal and small slopes ($\pm 15^{\circ}$) two-phase flow in pipes. This model was based on the work of Taitel and Dukler

(1976) for flow pattern predictions with slight modifications, and presented equations capable of estimating pressure drop differently for each flow pattern. Another model presented by Ansari et al. (1994) predicts both flow pattern and friction losses for vertical upward flow focused on wellbores. Additionally, this last work was highlighted, with reported consistent performance, by the literature review of Jerez-Carrizales et al. (2015).

One of the latest studies that was accomplished by Petalas and Aziz (2000), consists in a complete model, covering flow pattern map and friction loss calculations up to any slope (-90° to $+90^\circ$). The authors based their work on previously formulations developed by Barnea (1987), Barnea et al. (1985), Taitel and Dukler (1976) and Xiao et al. (1990). Besides that, this model's flow pattern map includes new classifications such as: dispersed bubble (DB), stratified smooth (SS), stratified wavy (SW), annular-mist (AM), elongated bubble (EB), slug (S) and froth (F). It was also pointed out by Petalas and Aziz (2000) that this model has superior performance compared to Beggs and Brill (1973), Dukler et al. (1964b), Mukherjee and Brill (1985) and Xiao et al. (1990). This evaluation was executed by running those models on 5951 experimental points from the Stanford Multiphase Flow Database (PETALAS; AZIZ, 1995). Additionally, Shuard et al. (2016) compared 60 CFD simulations of multiphase flow with this model, reporting valid agreement when it comes to flow pattern and friction loss predictions. After all, another CFD comparison was performed by Krumrick et al. (2016) on 17 different input conditions and consistent results were proclaimed.

During the present literature review, it was found out that recent studies rely on more specific techniques with restricted applications. One example is the work of Thome et al. (2013) that presented a unified mechanistic model applied to microchannels predicting flow patterns. Strictly for applications in petroleum reservoirs, Shahverdi and Sohrabi (2017) modelled the permeability of a three-phase (oil, water and gas) fluid in a porous media. Furthermore, Haider et al. (2017) studied the effect of particles transported by fluid flow on the erosion of industry components (pumps, valves, compressors, elbows and others). Lastly, other mechanistic models were developed for vertical and inclined slug flows by Abdul-Majeed and Al-Mashat (2000), transient state solid-liquid two-phase flows in the work of Zhang et al. (2018), critical heat flux in boiling flows by Huang and Kharangate (2019) and gas-liquid interface shape determination presented by Banafi and Talaie (2012). In sum, the last development found in the literature that predicts flow pattern transitions and allows pressure drop estimation individually for each flow pattern applied to two-phase flows in pipelines, considering a mechanistic approach, was presented by Petalas and Aziz (2000).

At last, on the last few decades machine learning algorithms and data-driven methodologies have been extensively developed and applied on state-of-the-art studies. As a consequence, selection of models using machine learning based on large experimental data sets as training source has demonstrated promising results as shown by Hernandez et al. (2019). Also, not only model selection but the direct

determination of liquid holdup (liquid phase volumetric fraction), flow pattern and pressure drop is estimated by machine learning algorithms trained on laboratory, as accomplished by Kanin et al. (2019).

Considering only mechanistic models capable of predicting the flow pattern or pressure drop for two-phase flows, Table 1 summarize the research works that may fit into the developments of the present work.

Table 1 – Multiphase flow mechanistic models applicable to predict flow pattern map or pressure drop in non-specific configurations (straight tubes).

Authors	Year	Output	Slope
Taitel and Dukler	1976	Flow pattern map	0°
Taitel, Barnea and Dukler	1980	Flow pattern map	+90°
Barnea, Shoham and Taitel	1982	Flow pattern map	-90°
McQuillan and Whalley	1985	Flow pattern map	+90°
Barnea, Shoham, Taitel and Dukler	1985	Flow Pattern Map	0° to +90°
Barnea	1987	Flow pattern map	-90° to +90°
Xiao, Shoham and Brill	1990	Flow pattern map and pressure drop	-15° to +15°
Ansari, Sylvester, Sarica, Shoham and Brill	1994	Flow pattern map and pressure drop	+90°
Petalas and Aziz	2000	Flow pattern map and pressure drop	-90° to +90°

2.4 IMAGE PROCESSING TECHNIQUES APPLIED TO MULTIPHASE FLOW

In order to obtain essential properties of the flow, meters installed at an experimental circuit or plant can be adopted. There is a wide range of meters on the market and on development on research centers capable of identifying void fraction and flow pattern, as studied by Da Silva et al. (2007), Shaban and Tavoularis (2017) and Velasco Peña and Rodriguez (2015). Moreover, Meribout et al. (2020) analyzed advantages and disadvantages of several techniques of multiphase flow measurement, including Pitot tube, venturi, inverted cones, vortex flow meter, Coriolis, positive displacement flow and cross correlation. It is possible to note that each

technique has advantages related to certain operational conditions, while has disadvantages attributed to low flow rates, operational environment, standardization, or Reynolds number. Another literature review work presented by Caliman and Ramos (2022) concluded that the international community recognizes that solving multiphase flows still is a technological challenge.

Considering two-phase flows, it is reasonable to consider its complexity for modeling purposes (even for one-dimensional approach). In many situations, describing the physics involved in each flow pattern formation, characteristic frequencies and pressure drop is still dependent of empirical formulations and directly related to experimental data. Due to this scenario, optical techniques and image analysis technologies are studied for representing non-intrusive and efficient research tools for multiphase flows' data extraction, as concluded by Zhou and Niu (2020). The authors used pre-processing, object detecting and object tracking algorithms applied on a video to measure size and velocity of bubbles on a bubbly flow. They reported consistent results, however, bubble clusters and overlapped bubbles represented a challenge to be overcome.

High-frame rate recorded videos is also a viable option to acquire information of a two-phase flow. To accomplish that, some commonly adopted image processing techniques are often used for contrast enhancement, noise reduction and interface recognition, those which are defined below.

- Binarization (DINARYANTO et al., 2016; KUNTORO et al., 2015; MORALES, 2011): A threshold of pixel values is defined, and the image can be transformed into a black and white one, with no intermediary values (different from a greyscale image).
- Image segmentation (DINARYANTO et al., 2016; DO AMARAL et al., 2013; KUNTORO et al., 2015; WIDYATAMA et al., 2018): The process of splitting the image into object and background, usually using binarization to convert pixel values into 0 or 1 (each one corresponding to background or object).
- Background subtraction (DINARYANTO et al., 2016; MOHMMED et al., 2016; MORALES, 2011; WIDYATAMA et al., 2018): Usually consists in evaluate an image of the background with no object present. In sequence, subtract background pixel values of the real image, isolating the object. This process is commonly used for moving object analysis aiming to have a clearer interface.
- Filters (DINARYANTO et al., 2016; DO AMARAL et al., 2013; KUNTORO et al., 2015; MOHMMED et al., 2016; MORALES, 2011; OLBRICH et al., 2018): This tool is applied to images that present high noise values. To minimize these noises a median filter can be applied, transforming each pixel value into the median of its neighborhood pixels. It is also expected that image sharpness is reduced after applying it.
- Skeletonize (KUNTORO et al., 2015): Used to transform the interface of an object into a line. An example is an image of a horizontal stratified flow. Using

proper filters and binarization process, the interface can be observed as a small region between phases. Then, this region is converted into a line by preserving pixels located exactly between upper and lower limits and filling non-selected pixels with phases' pixels value.

Using proper lightening hardware and a transparent test's section, Widyatama et al. (2018) were able to morphologically characterize the interface between air and water on a video of a slug flow. The authors used techniques of image processing such as image segmentation, background subtraction and binarization to identify water and gas phases. Another accomplished study found a certain degree of difficulty to measure Taylor bubble borders on a slug horizontal flow, mostly on high liquid and gas velocity due to the large amount of dispersed bubbles present (MORALES, 2011). Aiming to minimize these effects, it was applied a median filter to reduce image noise and a further binarization process of each frame. Authors demonstrated the success of the process, however, recognized that the technique used for image treatment requires improvements.

It was found out that there is a considerable variety of works on image processing applied to two-phase slug flows, such as the ones presented by Dinaryanto et al. (2016), Do Amaral et al. (2013) and Mohammed et al. (2016). Those works based a part of the image treatment on the binarization process and correct selection of a threshold value for the interface identification. On the other hand, Kuntoro et al. (2015) used this technique to study interfacial waves in a horizontal stratified gas-liquid flow. Also, to obtain a morphological characteristic of the flow, a skeletonize method was applied after the filtering and binarization process.

The work proposed by Olbrich et al. (2018) compares the output of an image processing algorithm with a CFD simulation. It was accomplished using a high-frame rate video of an intermittent two-phase flow to obtain the liquid level over time. Instead of a morphological method, authors selected a region of interest (ROI) as a line perpendicular to the flow and investigated pixel values binarized with pre-determined threshold. As a result, the interface could be reconstructed frame by frame and the liquid level sharply determined. One advantage of this technique relies on the possibility of reconstructing both the ROI of the real video and the liquid level over time. In this way, it is possible to validate the simulation in terms of characterized parameters of the flow. These parameters were quantified into analysis such as a fast Fourier transform (FFT) to evaluate the frequency spectrum and power spectral density (PSD) applied to both experiment and simulation. There are other works found on the literature that based the comparison between CFD results with experiments in such frequency tools, such as a similar work proposed by Schmelter et al. (2020). It was observed that authors highlighted that FFT do not necessarily represent the slug passage in an intermittent flow, however, it can provide a quantitative description of the dynamics of the flow in terms of the frequency of higher amplitude waves and be used for comparison between experiment and simulation.

2.5 OUTCOMES

Based on the literature review, it is possible to note that there are several multiphase flow models available (Table 1). As follows, three of them are selected for implementation, validation and comparison with experimental data. According to the pre-defined selection criteria for horizontal two-phase flows, it is chosen:

- The model of Taitel and Dukler (1976) for flow pattern determination due to its large number of authors that based their work on to develop new models.
- The model of Xiao et al. (1990) for friction loss predictions, for been based on the work of Taitel and Dukler (1976) and presenting a consistent physical base to calculate pressure drop.
- The model of Petalas and Aziz (2000) for both flow pattern and friction loss predictions, given the author's reported performance, capabilities to predict flow pattern and friction loss at any slope and for been tested by other authors (KRUMRICK et al., 2016; SHUARD et al., 2016).

In terms of the present work, the development of an image processing algorithm, filtering and binarization processes are based on the techniques presented by Dinaryanto et al. (2016), Do Amaral et al. (2013), Kuntoro et al. (2015), Mohmmed et al. (2016), Morales (2011), Olbrich et al. (2018) and Widyatama et al. (2018). Specially for the interface recognition, the works presented by Olbrich et al. (2018) and Schmelter et al. (2020) demonstrated consistent performance and possibility of further analysis such as liquid height over time, power spectral density - PSD and fast Fourier transform - FFT. In this way, the selection of a transversal section using a region of interest - ROI method, is a basis parameter for the current algorithm input data.

3 MATERIALS AND METHODS

This chapter describes the capabilities of the multiphase flow circuit of NEMOG's facility, as well as its estimation and validation, considering a method for experiment planning. Also, describes necessary procedures related to mechanistic models' validation and operation. At last, current section shows and organizes all the essential steps to develop an image processing algorithm applied to two-phase flow.

3.1 IMPLEMENTATION AND VALIDATION OF MECHANISTIC MODELS

The validation of selected flow pattern models was made by a computational code, written on MATLAB (2019). For flow pattern map, the codes were tested for same conditions as authors presented their results. Additionally, considering friction loss results, predictions of the models were compared to 70 experimental horizontal points of air-water flow provided by Payne et al. (1979).

Flow pattern map

The first model validated is proposed by Taitel and Dukler (1976) to horizontal two-phase flow pattern map for air-water. This map is demonstrated by the author selecting fluid properties and varying the superficial velocities J_G for the gas phase versus J_L for the liquid phase on a log-scale plot. It is highlighted that fluid properties such as density and dynamic viscosity values were not provided by authors. In this way, given pressure and temperature conditions, water properties were taken from the U.S. Department of Commerce (2021). Atmospheric air density was calculated by the perfect gas equation and viscosity consulted on Fox et al. (2014). Full information is detailed on Table 2.

Table 2 – Conditions used to generate flow pattern map of Taitel and Dukler (1976).

Variable name	Variable	Value or range	Units
Gas superficial velocity	J_G	0.1 – 500	m/s
Liquid superficial velocity	J_L	0.01 – 50	m/s
Absolute Pressure	P	101.3	kPa
Temperature	T	25.0	°C
Internal diameter	D_{int}	25	mm
Gas density	ρ_G	1.1841	kg/m ³
Liquid density	ρ_L	997.1	kg/m ³
Gas dynamic viscosity	μ_G	1.84E-05	Pa.s
Liquid dynamic viscosity	μ_L	0.00089	Pa.s

Additionally, the Equation 14 is numerically solved in terms of the liquid height h_L for stratified flow pattern and properties of the fluids. After obtaining the liquid height h_L , it is possible to calculate phases cross-sectional areas (A_G and A_L) and perimeters (S_G , S_L and S_i) in terms of geometrical relationships.

$$\tau_{WG} * \frac{S_G}{A_G} - \tau_{WL} * \frac{S_L}{A_L} + \tau_i * S_i * \left(\frac{1}{A_L} + \frac{1}{A_G} \right) + (\rho_L - \rho_G) * g * \sin \theta = 0 \quad (14)$$

In sequence, the following algorithm is applied for flow pattern determination, as shown in Figure 5.

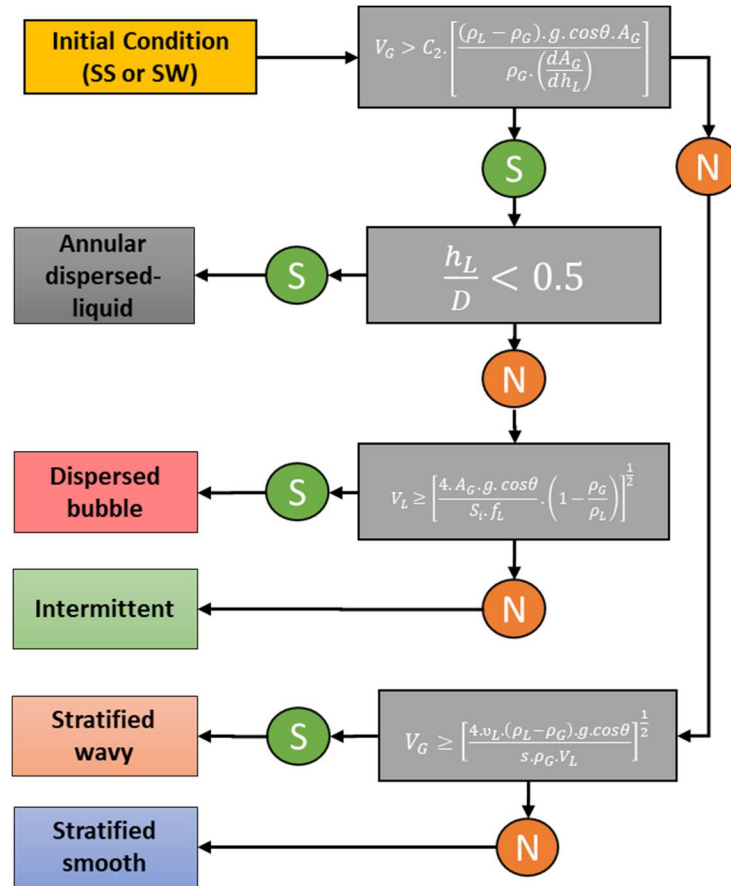


Figure 5 – Flow pattern determination algorithm based on Taitel and Dukler (1976).

The second flow pattern map to be validated is proposed by Petalas and Aziz (2000). The map is plotted also using superficial velocities as axes. However, pressure, temperature and properties values are given by authors according to Table 3.

Table 3 – Conditions used to generate flow pattern map of Petalas and Aziz (2000).

Variable name	Variable	Value or range	Units
Gas superficial velocity	J_G	0.01 – 200	ft/s
Liquid superficial velocity	J_L	0.01 – 100	ft/s
Absolute Pressure	P	101.3	kPa
Temperature	T	25.0	°C
Internal diameter	D_{int}	52	mm
Gas density	ρ_G	1.28	kg/m ³
Liquid density	ρ_L	999.55	kg/m ³
Gas dynamic viscosity	μ_G	0.01	cP
Liquid dynamic viscosity	μ_L	1.0	cP

In this case, the flow pattern map generation requires more than one momentum equation to be solved. For the stratified flow, it is also required to solve Equation 14 for the liquid height h_L . Therefore, annular-mist flow liquid film thickness δ_L is determined by the numerical solution of Equation 15, where the subscript f is related to film region and c to the core region. Additionally, the determination of liquid film thickness δ_L allows the calculation of phases cross-sectional areas (A_f and A_c) and perimeters (S_f and S_i).

$$\tau_{WL} * \frac{S_f}{A_f} - \tau_i * S_i * \left(\frac{1}{A_f} + \frac{1}{A_c} \right) + (\rho_L - \rho_C) * g * \sin \theta = 0 \quad (15)$$

From there on, the sequence of conditionals is tested for flow pattern stability according to the flowchart in Figure 6.

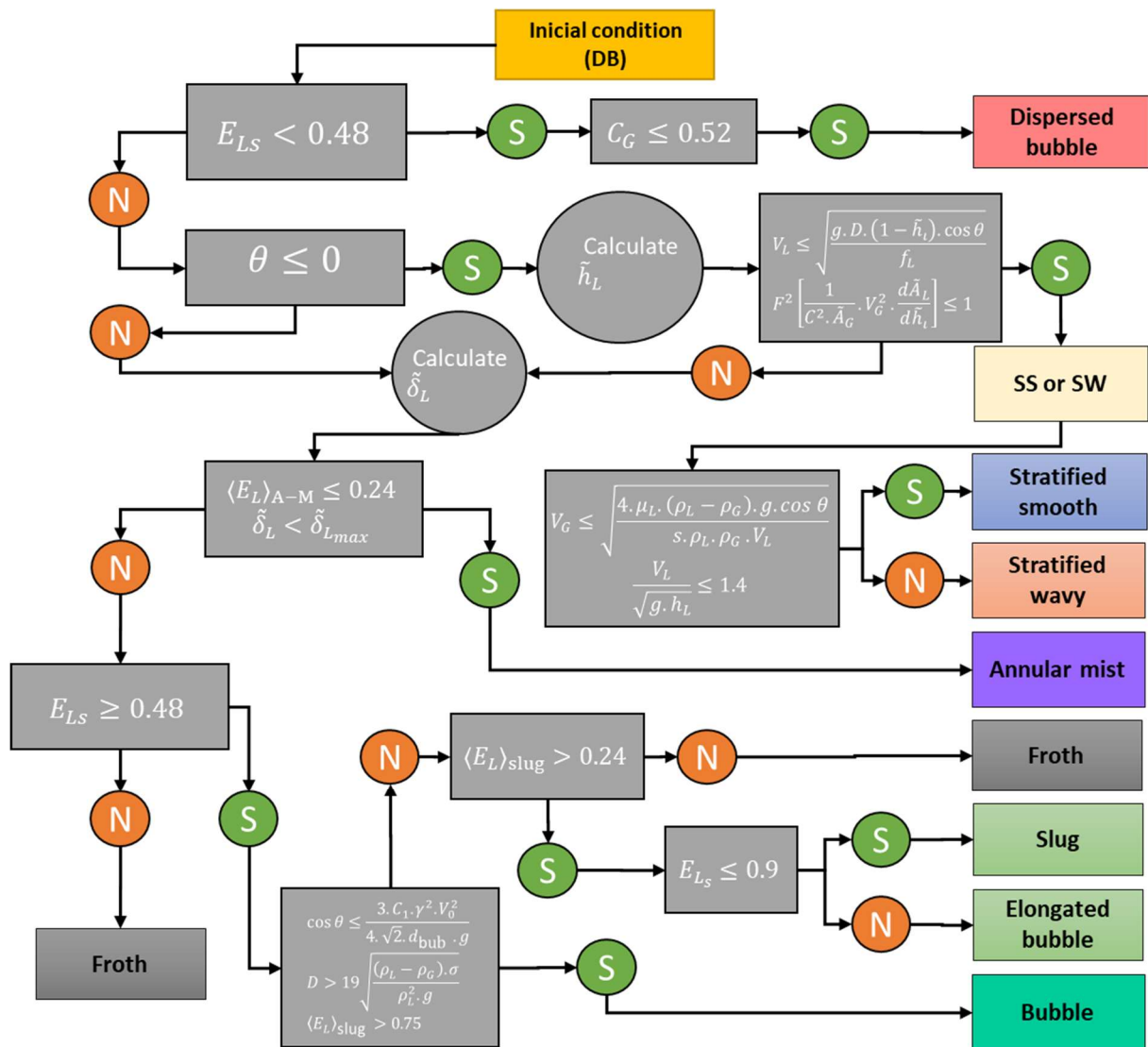


Figure 6 – Flow pattern determination algorithm inspired by Petalas and Aziz (2000).

Friction loss

For the friction loss model's validation, literature research was made in order to find two-phase flow pressure drop experimental points, consisting of a facility that is similar to NEMOG's multiphase flow circuit and presented results for 0° of slope. The work of Petalas and Aziz (2000) used 5951 experimental points present on the Stanford Multiphase Flow Database (PETALAS; AZIZ, 1995). However, the attempt to access those results were not successful.

As a consequence, the work of Payne et al. (1979) was chosen due to its experimental similarity to this work's facility configuration and also the lack of experimental results available on the literature. Also, 70 experimental results comprise different inlet pressures, temperatures, and superficial velocities. In this way, both models of (PETALAS; AZIZ, 2000; XIAO et al., 1990) were tested for pressure drop predictions against those measured points considering the same conditions as presented on the database.

Basically, after models predict a certain flow pattern, a method of pressure drop estimation is suggested in sequence. In this way, the model of Xiao et al. (1990) requires the solution of Equation 15 for the liquid film thickness δ_L for annular flow and Equation 16 is solved in terms of the liquid film height on the slug region h_f for intermittent flow.

$$\tau_f * \frac{S_f}{A_f} - \tau_G * \left[\left(\frac{S_G}{A_G} \right) + \left(\frac{\tau_i}{\tau_G} \right) * \left(\frac{S_i}{A_f} + \frac{S_i}{A_G} \right) \right] + (\rho_L - \rho_G) * g * \sin \theta = 0 \quad (16)$$

On the other hand, the model presented by Petalas and Aziz (2000) does not depend upon a numerical solution of more equations for pressure drop estimation, only the ones already solved for flow pattern determination (Equations 14 and 15).

3.2 NEMOG'S MULTIPHASE FLOW CIRCUIT ENVELOPE ESTIMATION

The theoretical operational capacity of the circuit was first estimated considering the maximum differential pressure generated by the water pump, air compressor and single-phase flow meters calibrated ranges. In this way, the first limiting component is the water pump, which reaches a differential pressure of $\Delta P_{max} = 234.2 \text{ kPa}$. As a result, given a working absolute pressure P , it is considered that the maximum achievable pressure is $P + \Delta P_{max}$.

Furthermore, water single-phase Coriolis flow meters are certified and calibrated according to Associação Brasileira de Normas Técnicas (2015) by METROVAL. For the low flow rate line, a range between 2 – 20 m^3/h is certified, while for the high flow rate line this range is 8 – 80 m^3/h . Considering the orifice plates used on the flow measurement of gas phase, those were calibrated and certified also

according to Associação Brasileira de Normas Técnicas (2015) by ITFLUX. The air line at low flow rate working range is 59 – 236 kg/h and high flow rate is 236 – 1180 kg/h. Therefore, it can be assumed a flow range 2 – 80 m³/h for the water and 59 – 1180 kg/h for the air phase. Table 4 shows circuit's operational capacity based only on restrictions imposed by the current hardware.

Table 4 – Operational conditions based on NEMOG's facility capacity.

Fluid	Operating Conditions	Minimum flow rate	Maximum flow rate
Water	$P + \Delta P_{max} = P + 234.2 \text{ kPa},$ $T = 25^\circ\text{C}$	2 m ³ /h	80 m ³ /h
Air	$P + \Delta P_{max} = P + 234.5 \text{ kPa},$ $T = 25^\circ\text{C}$	59 kg/h	1180 kg/h

Chosen models for operational flow patterns envelop (PETALAS; AZIZ, 2000; XIAO et al., 1990) were used to estimate the maximum theoretical flow rate in which pressure drop would overcome the value of ΔP_{max} .

Considering that those models for friction loss estimation works on a discrete environment, the length domain L [m] of the circuit is divided into n elements and each element has its respective calculated dP/dL . It can be said that this gradient is multiplied by the length of the considered element L/n , resulting in a local value of dP . The local value of dP is then subtracted from the maximum achievable pressure $P + \Delta P_{max}$, resulting in an absolute local pressure P_i . Additionally, it should be highlighted that this process is made all along the length domain L , or if the total pressure drop prediction $\sum_1^i dP$, for $i < n$, reaches the value of the maximum pressure available ΔP_{max} . In other words, if the absolute local pressure of a given element is $P_i \leq P$, the algorithm should stop and skip to the next pair of J_G and J_L .

In this way, for each combination of superficial velocities J_G and J_L , it can be estimated if the pressure drop will overcome the capacity of the water pump. Consequently, indicating a situation in which the pressure gradient is not favorable to the flow, and it should not be considered to the operational envelop of the circuit since a limiting flow rate value is achieved. On the other hand, if $P_i \geq P$ along the entire domain of L , it is considered that this is a valid prediction. Lastly, both theoretical operational capacity and estimated operational envelop are compared with the actual envelop obtained experimentally.

3.3 EXPERIMENTAL CIRCUIT SETUP

The multiphase closed flow loop is dedicated to evaluate the performance of multiphase flow meters, by the comparison to single-phase flow metering of each component: mineral oil, water, and compressed air. Considering the present work, experiments in this circuit consists in air-water two-phase flows. Additionally, each section of the closed loop has its respective functionality and details can be observed in Figure 7.

Single phase fluids are stored in tanks for tap water and mineral oil (Sector I). In addition, after individual measurement and control in Section III, the multiphase flow is generated by mixing single-phase components (Sector IV). The reference technologies for single-phase flow metering are independent of each other. Besides flow rate, fluid densities, pressure, and temperature are monitored as well.

Tubing of test branch is steel made, #150 psi class ($\Phi 2''$ x 12m each straight branch). Additionally, presence of translucent tube spools allows visualization of multiphase flow patterns (Sector V). After passing by the test branch, the components are separated by a large gravimetric three-phase separator vessel with the capacity of 14 m^3 (Sector II).

Specifically in Sector V, many sensors are installed, such as capacitive pressure transducers, temperature sensors and a high-frame rate camera positioned in front of the translucent section. In this way, temperature, differential and absolute pressures are measured at a rate of 4 Hz. For this sector scheme, Figure 8 shows the details and respective location of each equipment. Pressure drop is measured by differential pressure transducers (1-5), high speed camera (2) is used to record two-phase flow videos at the translucent section (3), the manometric pressure is measured by the pressure transducer (4) and further used to calculate fluid properties by considering the absolute pressure and the temperature is measure by a thermocouple (6).

Additionally, despite single-phase flow rate measurements, the section where properties are calculated in terms of measured pressure and temperature is located between elements 1-6 and has a total length of 5100 mm. For the pressure drop measurement, the length is 4800 mm (91.5D) and for the whole test's section the total length is 14400 mm.

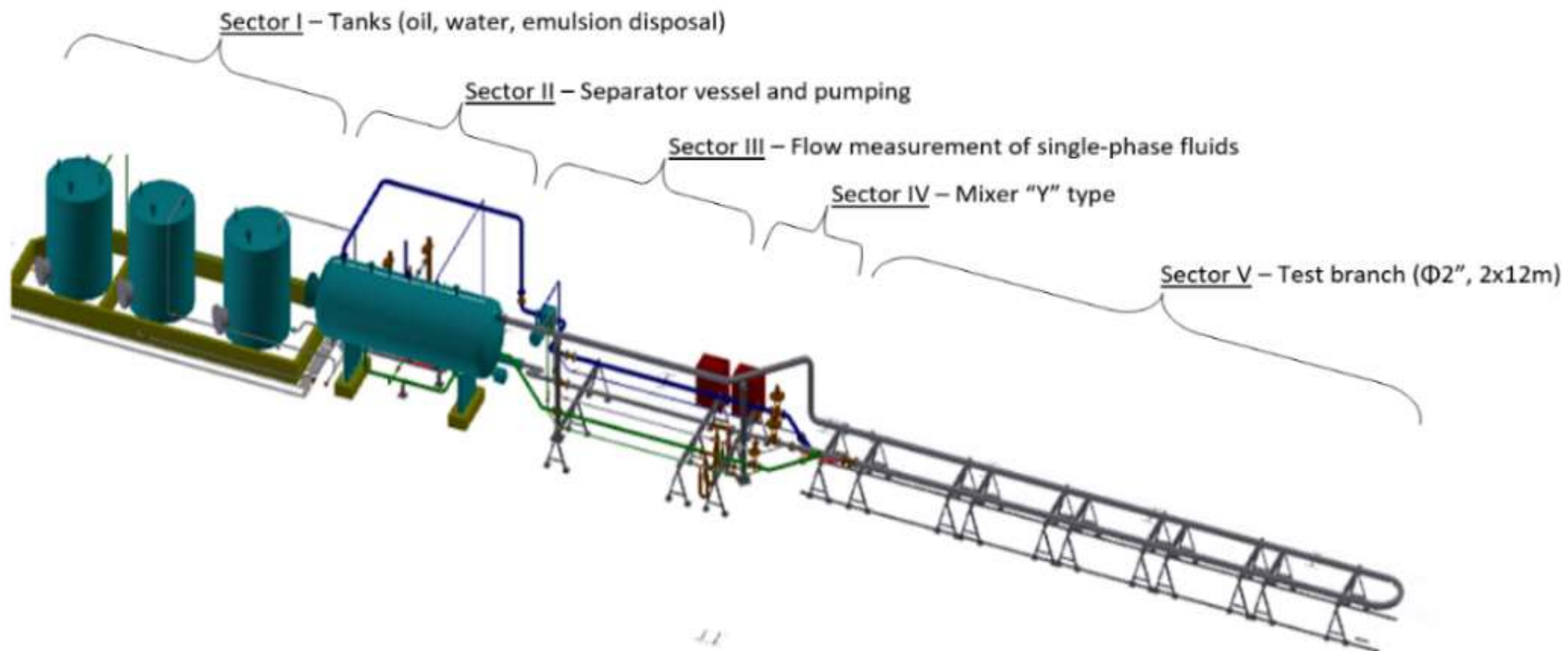


Figure 7 – Overview of NEMOG's multiphase flow closed loop

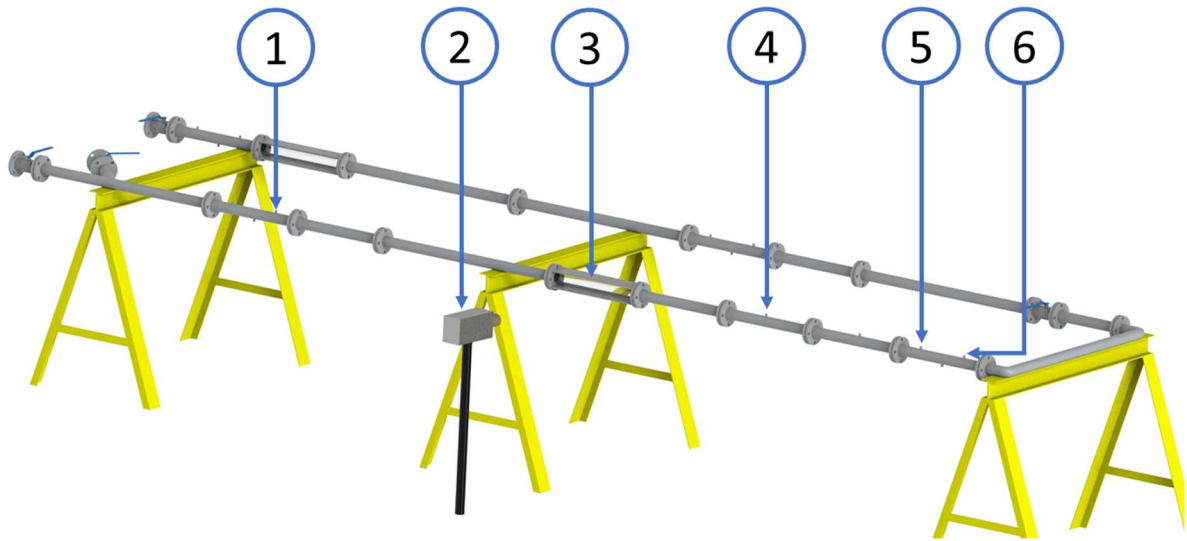


Figure 8 – NEMOG's test section and experimental setup. (1-5) Differential pressure transducers, (2) high-speed camera, (3) translucent section, (4) manometric pressure transducer and (6) thermocouple.

3.4 SINGLE PHASE FRICTION LOSS VALIDATION

First of all, seven rounds of single-phase flow experiments were taken in order to compare the pressure drop measurements with a well-established method to estimate the single-phase friction factor, at different water flow rates. Also, measurements reproducibility is verified by repeating each experiment three times. Selected correlations showed in Equations 17 and 18 were proposed respectively by Coolebrook and Darcy-Weisbach representing a tool to estimate the turbulent friction factor and pressure drop (MINHONI et al., 2020). Additionally, e_w is the wall absolute roughness, D is the internal diameter, L the pipe length, Re the Reynolds number, g is the gravity acceleration and V the fluid velocity.

$$\frac{1}{\sqrt{f}} = -2 * \log \left(\frac{\frac{e_w}{D}}{3.7} + \frac{2.51}{Re * \sqrt{f}} \right) \quad (17)$$

$$\Delta P = f * \frac{L}{D} * \frac{V^2}{2 * g} \quad (18)$$

Therefore, if predictions agree with experimental measurements of pressure drop, the proposed pressure intake configuration (transducer 1-5), as shown in Figure 8, can be considered valid. Additionally, it will possibly identify systematic errors on specific flow rates or where uncertainties may interfere on the results interpretation. It is also important to note that both section length L and absolute pipe wall rugosity

e_w are correspondent values adopted on the mechanistic model's code for two-phase flows. At last, localized pressure drop is considered for this calculation in terms of blind T-junctions present on the circuit, however, flange misalignment is not considered here.

3.5 TEST'S MATRIX

Considering the objective of evaluating the mechanistic model performance and collecting flow information by means of recording and processing high-frame rate videos, a matrix of tests is elaborated following the lead of Montgomery (2013) on the design of experiments. The aim of this planning is being able to strategically extract the largest amount of information with only necessary experimental points. Therefore, NEMOG's circuit is projected to work with absolute pressures varying from the atmospheric reference, 101.3 kPa, to 800 kPa. In such manner, it should be considered that pressurizing the circuit at its limit and activating the water pump in its maximum capacity may lead to safety concerns or potential equipment limiting factors. Consequently, the upper absolute pressure limit is set at 700kPa measured at the test section with component 4 of Figure 8. The lower absolute pressure limit is defined as the maximum absolute pressure achieved at the higher flow rate (water and air simultaneously), letting the separator vessel completely open to atmosphere. Intermediate pressure value is the median between upper and lower limits. In terms of water and air flow rates, minimum values are limited according to Table 4, while the maximum may be limited by water pump capacity overcoming pressure drop along the experimental circuit or single-phase flow meters limits. Since this capacity was not tested before, determining it becomes a task of this work.

The selected experimental matrix is the factorial central compost planning due to its capacity to estimate model curvature. This matrix is shown in Table 5 detailing experimental points in terms of pairing flow rates: minimum flow rate, median flow rate and maximum flow rate. Besides that, there are a total of 27 experimental points for the first round, since it is considered three pressure values to be investigated (minimum, median and maximum pressures), despite flow rate combinations. During this round, maximum capacity of the circuit is tested in terms of flow rate and an actual envelope is defined for each pressure value.

In sequence, a second round of tests is planned in terms of comparing points in which the same superficial velocities can be achieved, but now, submitted to different absolute pressures. It means that, given three operational pressure envelopes, obtained on the first experimental round, there is a common region where it is possible to reproduce experiments relying on same superficial velocities. Additionally, for this second round, a simple factorial planning is designated, and a total of 12 experimental points is specifically selected, being 4 points for each absolute pressure value as shown in Table 6.

Table 5 – Example of factorial central compost planning.

Test Number	Absolute pressure	Gas mass flow rate	Liquid volumetric flow rate
1	Lower	Lower	Lower
2	Lower	Lower	Median
3	Lower	Lower	Higher
4	Lower	Median	Lower
5	Lower	Median	Median
6	Lower	Median	Higher
7	Lower	Higher	Lower
8	Lower	Higher	Median
9	Lower	Higher	Higher
10	Median	Lower	Lower
11	Median	Lower	Median
12	Median	Lower	Higher
13	Median	Median	Lower
14	Median	Median	Median
15	Median	Median	Higher
16	Median	Higher	Lower
17	Median	Higher	Median
18	Median	Higher	Higher
19	Higher	Lower	Lower
20	Higher	Lower	Median
21	Higher	Lower	Higher
22	Higher	Median	Lower
23	Higher	Median	Median
24	Higher	Median	Higher
25	Higher	Higher	Lower
26	Higher	Higher	Median
27	Higher	Higher	Higher

Table 6 – Example of factorial planning.

Test Number	Absolute pressure	Gas mass flow rate	Liquid volumetric flow rate
28	Lower	Lower	Lower
29	Lower	Lower	Higher
30	Lower	Higher	Lower
31	Lower	Higher	Higher
32	Median	Lower	Lower
33	Median	Lower	Higher
34	Median	Higher	Lower
35	Median	Higher	Higher
36	Higher	Lower	Lower
37	Higher	Lower	Higher
38	Higher	Higher	Lower
39	Higher	Higher	Higher

As a result, it is expected that the first round identifies the operational flow circuit limits, possible flow patterns, pressure drop measurements, liquid height, and void fraction. Moreover, second round aim to allow a fair comparison on pressure influence over these variables. Lastly, it is pointed out that this procedure consists in a total of 39 experimental points and all of them are compared with predictions by mechanistic model, recorded and submitted to the image processing algorithm.

3.6 VIDEO RECORDING SETUP

The high-frame rate recorded videos are obtained by the hardware *Hot Shot 512 SC* camera (NAC IMAGE TECHNOLOGY, 2006). Videos are recorded at 1000 *FPS* and 512x512 resolution with a period of 8 seconds, resulting in a total of 8000 frames each video. In addition, to increase contrast, a background direct current *LED* is installed inside a non-reflective black box, behind the translucent visualization section. The camera is positioned on the same height and aligned to the tubing circuit and 1.0 meter apart. Both focus and optical zoom configurations are standardized by limiting markers on the transparent section. Details on recording setup and used hardware are shown in Figure 9 and Figure 10.

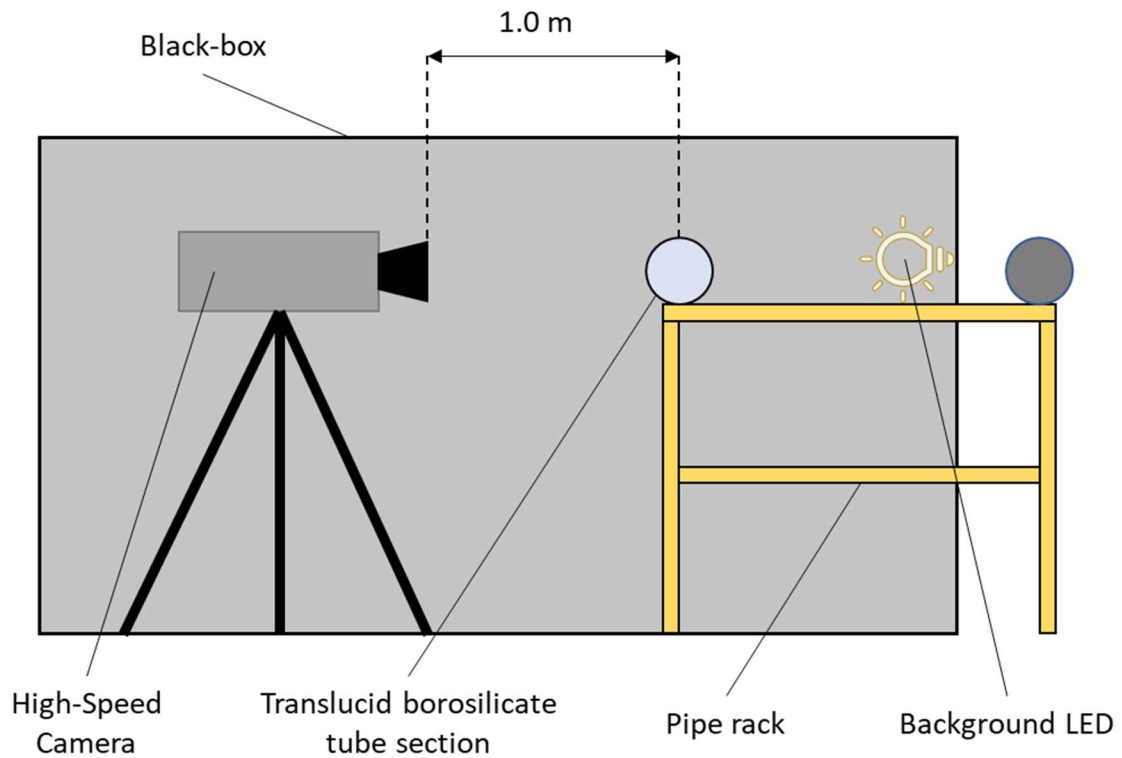


Figure 9 – Sketch of high-speed camera installation in NEMOG multiphase flow circuit.



Figure 10 – High-speed camera used in the experiment: *Hot Shot 512 SC* camera (NAC IMAGE TECHNOLOGY, 2006).

3.7 VISUAL CLASSIFICATION PARAMETERS

For the visual classification parameters, flow patterns defined by Taitel and Dukler (1976) for horizontal two-phase flows were selected as reference. Additionally, since other authors may categorize flow patterns differently, this method represents a

standard already used in this work and the one that has the most well definite classifications. In this way, as shown in Figure 3, possible designations can be:

- Stratified smooth (SS)
- Stratified wavy (SW)
- Dispersed bubble (DB)
- Annular mist (AM)
- Intermittent (I)

Yet, all videos are analyzed by three referees (including this author) without knowing the information of predictions provided by models. It is important to highlight that all referees have worked with or studied two-phase flows and are aware of the values of superficial velocities, pressure and temperature of each experimental point.

3.8 IMAGE PROCESSING ALGORITHM

The image processing algorithm is developed with the first objective of collecting the liquid height over time. Since the recorded video has a large amount of data stored as multiple RGB images, the algorithm must be capable of separately process each one of these images (or frames).

The procedure to treat video files is explained step-by-step as follows:

- 1) Format “.avi” video files are loaded on MATLAB (2019) using the function *videoreader*.
- 2) Height, width, number of frames and recorded FPS information is stored.
- 3) For a reference purpose, each frame data is stored into a vector where the frame number corresponds to the vector index.
- 4) Frames are converted to a third order tensor using *cell2mat* function, in which the first and second indexes correspond to pixels location on screen, while the third refers to the values of red, green, and blue (RGB) intensity varying from 0 to 255.
- 5) Each frame is divided into 3 different images, each one containing information of a specific color.
- 6) From now on, since the objective relies on identifying the interface between water and air, color that presents more contrasting intensities should be selected. Due to the natural yellow-brown coloring of the water, it is expected that the blue image represents the highest contrast, what can be confirmed after analyzing one example of used frame in Figure 11.
- 7) In sequence, as highlighted by Dinaryanto et al. (2016), Do Amaral et al. (2013), Kuntoro et al. (2015), Mohmmed et al. (2016) and Olbrich et al. (2018), a binarization process can be used to, given a selected threshold, transform integer values of light intensity between 0-255 to 0 or 1 (0 representing black and 1 representing white) resulting in a contour image as

shown in Figure 12. However, selecting the correct threshold value required the evaluation of the height over time algorithm's output for each video individually, which is also discussed (see Figure 14 and steps 13 - 16).

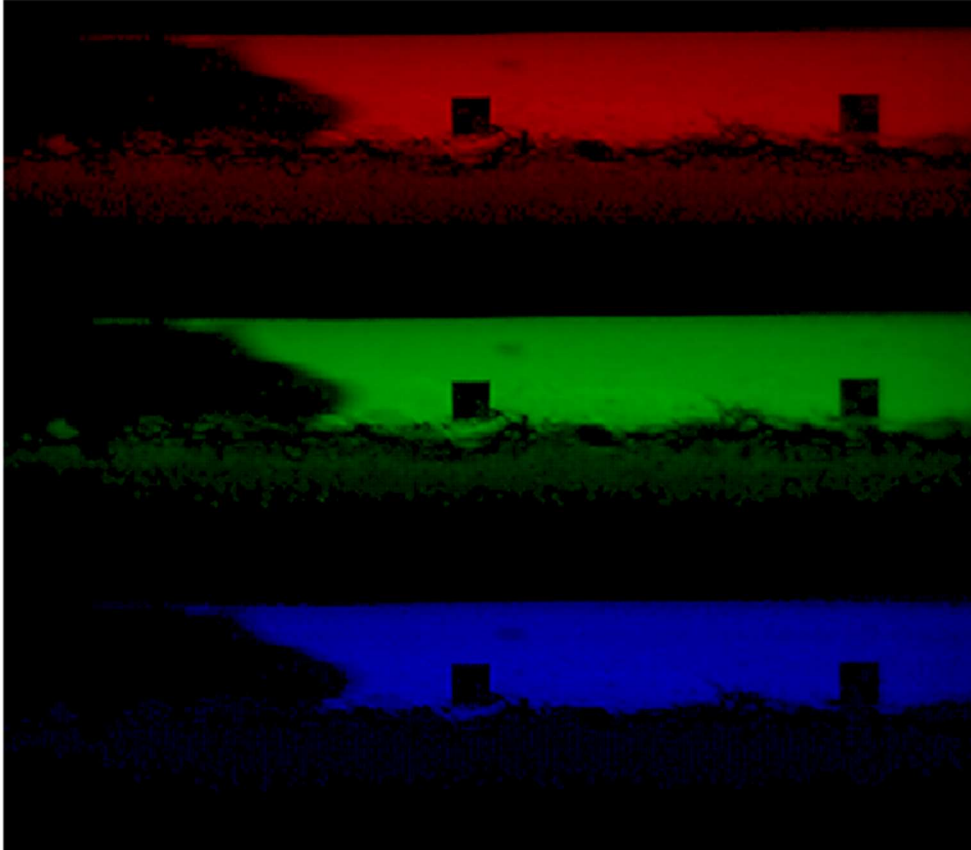


Figure 11 – Comparison between selected color contrast on a frame.



Figure 12 – Binarized image.

- 8) To evaluate the liquid height, a Region of Interest - ROI is defined as a one-dimensional transversal line that covers the whole diameter of the translucent section.
- 9) For the binarization threshold selection, both ROI A or B can be used, and it was defined region B as standard. Furthermore, this region has a certain number of pixels that are equivalent to the pipe's diameter D .

- 10) Therefore, an investigation loop is made to test each pixel value along ROI B in a binarized image from bottom to top. If a pixel value of 1 is returned, the loop stops, and the number of pixels is stored into a vector.
- 11) Further, this number is converted into a fraction of the diameter and an estimation of the liquid height for a frame is obtained. As follows, Figure 13 exemplifies regions of interest defined on a full RGB frame.
- 12) Additionally, an arbitrary threshold value is defined for the beginning of the verification process.
- 13) In sequence, values of liquid height and real pixel values of the blue frame are stored and further compiled into an integrated image containing all ROIs B over time, as shown in Figure 14.
- 14) This integrated image is then analyzed in terms of tracking height output capacity and comparing with the actual video.
- 15) If it is considered a match, this threshold value is defined. On the other hand, this value is adjusted until a correct measurement is achieved.
- 16) Besides that, it is relevant to note that this is repeated for each video as calibration process before the rest of the algorithm is handled.



Figure 13 – Non-treated RGB frame and ROI's location.

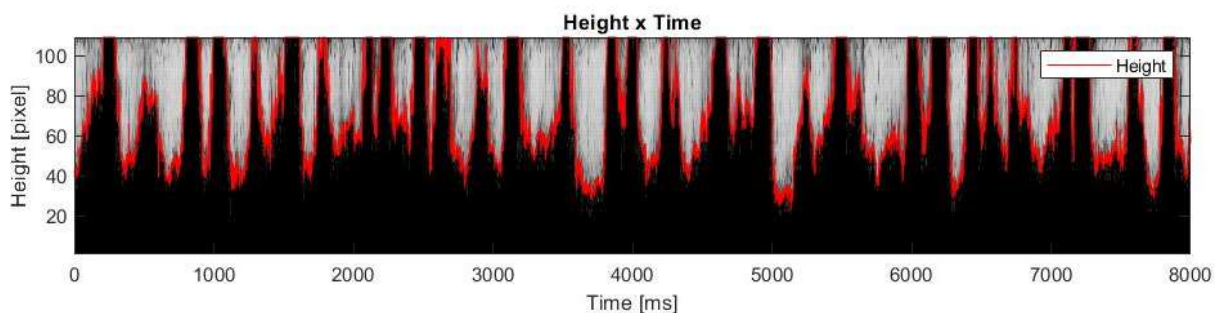


Figure 14 – Comparison between height's output and real video.

Also, Figure 14 brings the possibility of evaluating the frequency domain of the height value occurring through ROI B, since events have a time reference. This process was accomplished using the Fast Fourier Transform - FFT tool presented on MATLAB (2019) and for the present work, a single-sided amplitude spectrum as a function of frequency is the aimed output. Furthermore, it is emphasized that this tool is used to characterize the dominant frequencies of the flow and do not correspond directly to the slug passage. In other words, the FFT returns which frequencies and amplitudes compose the analyzed signal in the form of a sum of sinusoidal functions

(each one with respective frequency and amplitude). As a result, characteristic frequencies that compose the flow can be quantified and further compared with defined flow pattern. Lastly, the PSD (power spectral density) graph can be plotted also using the FFT function and the spectral energy distribution per unit of time is evaluated to support the flow pattern map comparison.

Geometrical approach

In terms of instantaneous void fraction (or gas fraction), α_G^i is calculated by geometrical relationships presented on Equations 19 and 20 as a function of the liquid height h_i , where i is the frame index, which is exemplified in Figure 15.

$$\alpha_G^i = \frac{\frac{D^2}{8} * (\theta_i - \sin(\theta_i))}{A} \quad (19)$$

$$\theta_i = 2 * \pi - 2 * \arccos\left(1 - 2 * \frac{h_i}{D}\right) \quad (20)$$

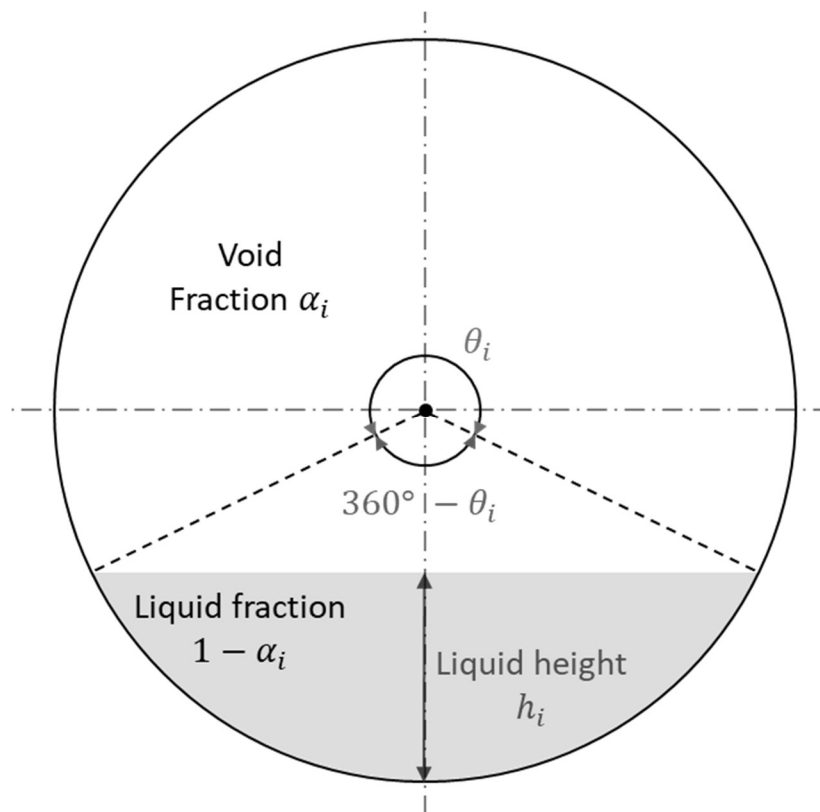


Figure 15 – Cross section geometrical approach scheme.

Since the target flow pattern is intermittent, it is expected a drift velocity V_{GL} occurring between phases, then the calculated void fraction using this technique may differ from the averaged injection void fraction. To make this comparison possible, the

time averaged value of α_G^i must be used and is represented by $\langle \alpha \rangle_G$ on Equation 8.

This geometrical relationship allows to estimate the gas velocity V_G flowing considering an average value of the void fraction and the superficial velocity J_G , as previously defined in Equation 10.

Frequency shift technique

Besides that, using regions A and B and collecting h_i over time generate similar values but spaced in time, as cycling waves. In comparison, it is the same as emitting the same sound with a certain distance between the sources. Knowing the frequency delay and the distance, the velocity can be calculated, since each frame corresponds to 0.001 second.

One problem of implementing this method to estimate V_G is that the function *finddelay* of MATLAB (2019) library process the delay between all amplitudes, shifting the waves until the maximum value of amplitude is achieved, which can generate an error on the velocity value. In this way a possible solution to eliminate unwanted frequencies is following the step-by-step procedure:

- 1) To achieve the binarization, it is necessary to adopt a moving average filter of order 30 using function *medfilt1* to reduce noises.
- 2) Implement a high-pass filter through the function *double* with a threshold set to the diameter of the pipe. Consequently, binarizing the value of h_i to 0 or 1 (1 means that the water touches the top end of the pipe).
- 3) After that, binary waves are observed representing each slug passage, consequently the shift could be estimated by the function *finddelay* and correlated to the gas velocity V_G .

It is also important to highlight that this algorithm is developed to work on intermittent gas-liquid horizontal flows. Even though, all flow patterns presented in this dissertation are submitted to the image processing code and results are further discussed.

Code parameters performance

Aiming to evaluate the best distance L (Figure 13) between regions A and B, it is important to define relations and establish parameters in which results can correctly represent flow phenomena. This evaluation is made processing the most well defined intermittent experimental point video using ROI's distance varying from 0 to 3D (internal diameters) with a resolution set to the number of pixels.

Considering the signal shift value, it is expected that the delay, in milliseconds, increases in a linear form while increasing the distance L . Consequently, this results in a graph containing distance *versus* shift, and the most linear region is selected as a possible valid distance. The second analysis is made by plotting the distance L *versus* gas velocity V_G , calculated by the frequency shift approach. In this graph, a region of constant V_G value is searched since this output variable should not be affected by L . Also, it is expected that at short distances the spatial and temporal resolution may decrease output accuracy, while the longer distances may be more influenced by morphological changes due to turbulence and may not represent the correct correlation.

ROI output data

The first output data from the image processing algorithm is the liquid height h_i . In terms of this variable, averaged void fraction $\langle \alpha \rangle_G$ can be estimated by the geometrical approach (Equation 19). In sequence, it is possible to calculate the gas phase velocity V_G , by Equation 10. Additionally, V_G is also estimated by the frequency shift technique, while $\langle \alpha \rangle_G$ can be calculated using the superficial velocity J_G , as Equation 10 shows.

Lastly, both frequency spectrum and power spectral density are analyzed and compared given set flow pattern. It is also important to highlight that this algorithm was first idealized to NEMOG's facility in order to supply boundary conditions (in form of periodic perturbations) for an intermittent two-phase flow CFD simulation and facilitate a further validation. On the other hand, it demonstrated to be quite useful to characterize properties of the flow and add new variables to this work.

3.9 OUTCOMES

In general, this section showed the adopted method of validation for the mechanistic models' code for both flow pattern and friction loss predictions as well as procedures of how to estimate NEMOG's multiphase flow circuit operational envelop. Additionally, circuit's setup is defined, and a matrix of tests is demonstrated based on the literature on design of experiment.

In terms of the video recording setup, resolution and recording speed are adopted for the best cost benefit in terms of quality and available recording time. Also, the operation of image processing algorithm is explained as well as expected output data. Lastly, possible concerns were raised regarding flow patterns differently from intermittent and definition of best distances between ROI A and B.

4 RESULTS AND DISCUSSION

4.1 VALIDATION OF MECHANISTIC MODELS CODE

As discussed before in Section 3.1, the validation of mechanistic models' implemented code is carried out considering two different approaches. The first one corresponds to the flow pattern map generation and comparison with respective author own results (PETALAS; AZIZ, 2000; TAITEL; DUKLER, 1976). The second approach relies on the comparison of pressure drop predictions using models developed by Petalas and Aziz (2000) and Xiao et al. (1990), with measurements provided by Payne et al. (1979).

Flow pattern map approach

As shown in Figure 16 and Figure 17, flow pattern areas, delimited by continuous lines representing data provided by respective author's model, matches with the data predicted by the developed code of flow pattern map, represented by colored dots. It is important to highlight that figures provided by the referred authors are in form of images and the boundaries needed to be reconstructed for this comparison, representing a possible source of uncertainties. However, in a general way, the agreement between regions is reasonable with a few mismatches, considering a qualitative and visual comparison. Consequently, it is considered that this implementation is validated and ready for further use.

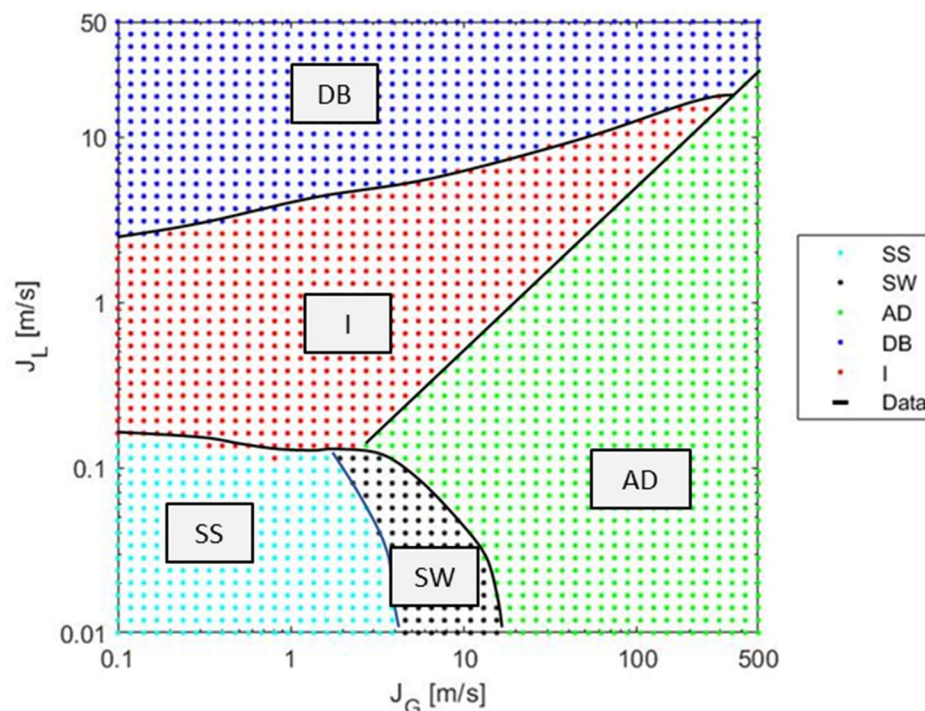


Figure 16 – Comparison of current implementation represented by colored dots and author's provided data identified by boundary lines (TAITEL; DUKLER, 1976).

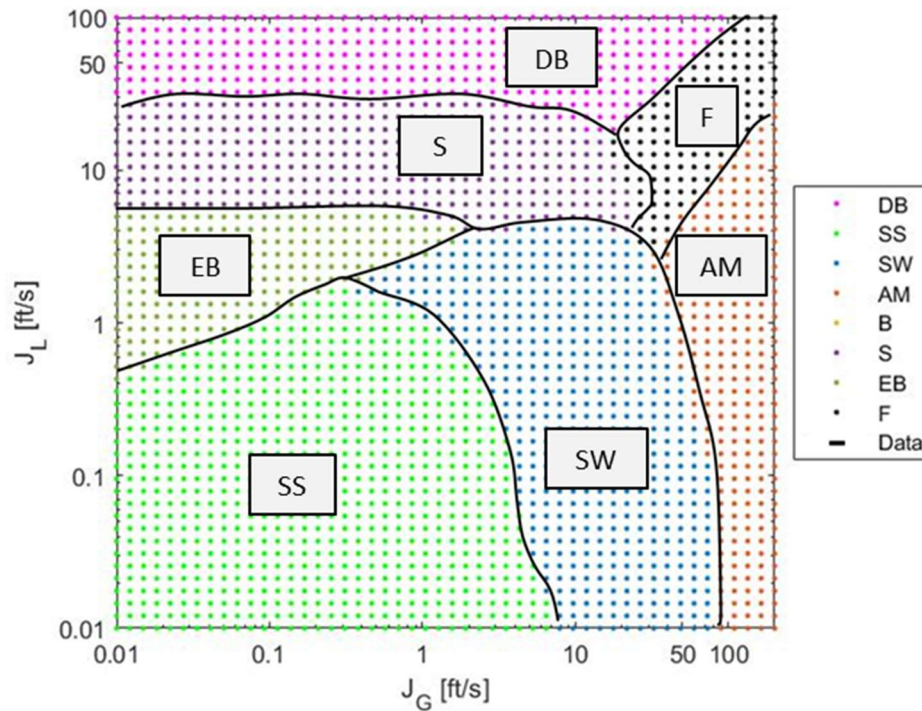


Figure 17 – Comparison of current implementation represented by colored dots and author's provided data identified by boundary lines (PETALAS; AZIZ, 2000).

Pressure drop approach

For the pressure drop code validation, considerations on the criteria for validation must differ from the flow pattern map ones since pressure drop measurements are tainted by uncertainties and models depends on the flow pattern determination for selecting the correct calculation method. As a result, trend line, absolute relative error E_i and standard deviation of the error σ are evaluated for the predictions presented in Figure 18 and Figure 19. The absolute relative error is defined in Equation 21 by the magnitude of the difference between the predicted value x_i using the mechanistic models and the measured differential pressure k_i . Additionally, this evaluation is also performed considering the averaged value of E_i for a specific sample, shown in Equation 22. Lastly, the absolute error e_i is calculated by Equation 23 and further used to evaluate the standard deviation of the error, presented in Equation 24.

$$E_i = \frac{|x_i - k_i|}{k_i} * 100 \quad (21)$$

$$E_{sample} = \frac{\sum_{i=1}^n E_i}{n} \quad (22)$$

$$e_i = x_i - k_i \quad (23)$$

$$\sigma_{sample} = \sqrt{\frac{\sum_{i=1}^n (e_i - \bar{e})^2}{n - 1}} \quad (24)$$

In general, the model of Xiao et al. (1990) presented a trend line following 45° considering the entire data bank. However, results do not correspond to the measurements when considering stratified wavy flow pattern only. The averaged absolute relative error of all flow patterns is $E_{1ALL} = 55.79\%$, while it is $E_{1I} = 43.08\%$ for intermittent, $E_{1SW} = 61.24\%$ for stratified wavy and $E_{1AD} = 66.67\%$ for annular-dispersed liquid. Additionally, standard deviation resulted on $\sigma_1 = 13.81$ kPa and the maximum absolute relative error reaches 228.74%, indicating that results are relatively dispersed.

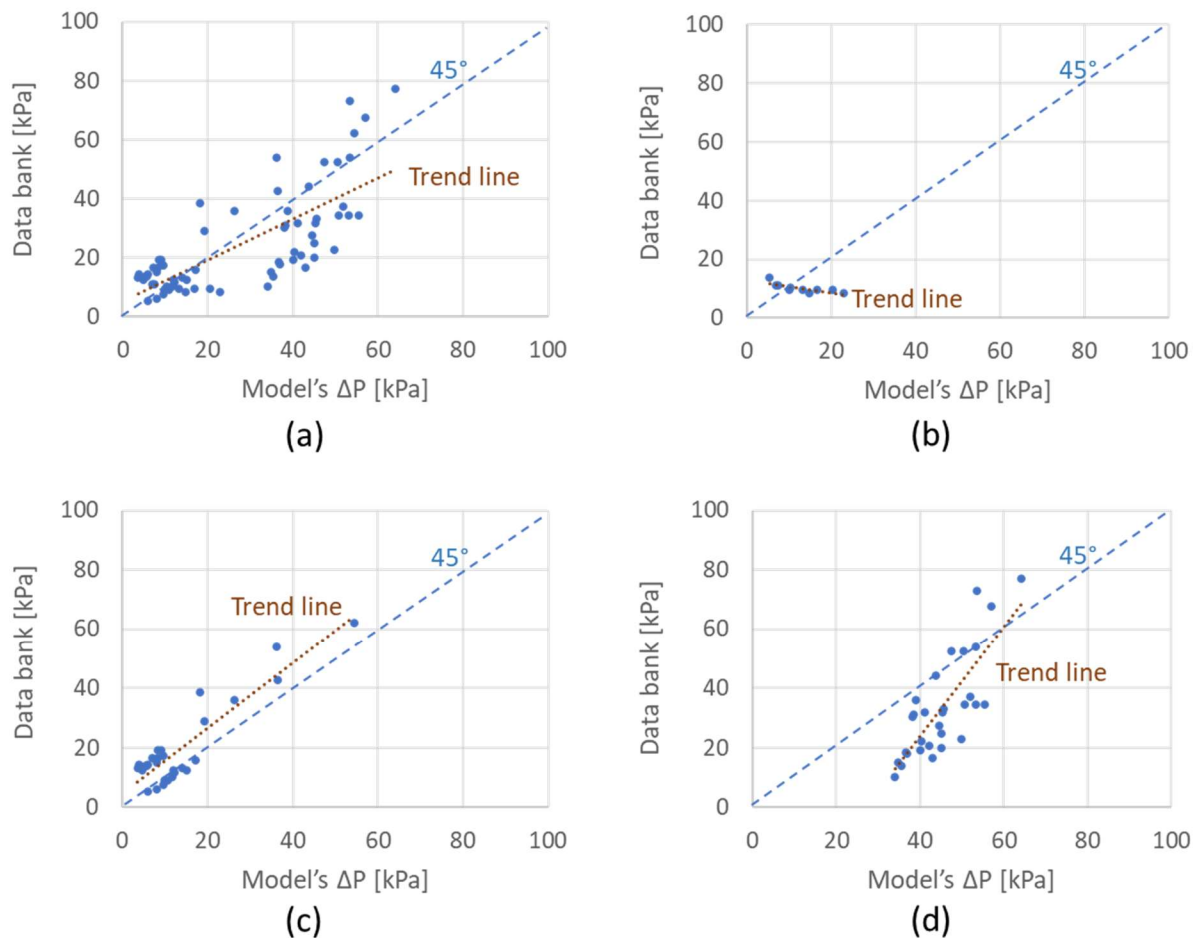


Figure 18 – Xiao et al. (1990) model's predictions compared with experimental data by Payne et al. (1979). (a) Full databank, (b) Stratified wavy flow pattern, (c) Intermittent flow pattern, (d) Annular-dispersed liquid flow pattern.

In terms of the model of Petalas and Aziz (2000), trend lines also follows 45° for the entire data bank, despite stratified wavy flow pattern. For all flow patterns the averaged absolute relative error is $E_{2ALL} = 36.84\%$ and for individual evaluation, $E_{AI} = 39.36\%$ for intermittent (EB and S), $E_{ASW} = 79.82\%$ for stratified wavy and $E_{AAD} = 20.71\%$ for annular mist. Then, the standard deviation is calculated to be $\sigma_2 = 6.85$ kPa, almost half if compared to σ_1 and the maximum relative error is 93.43% .

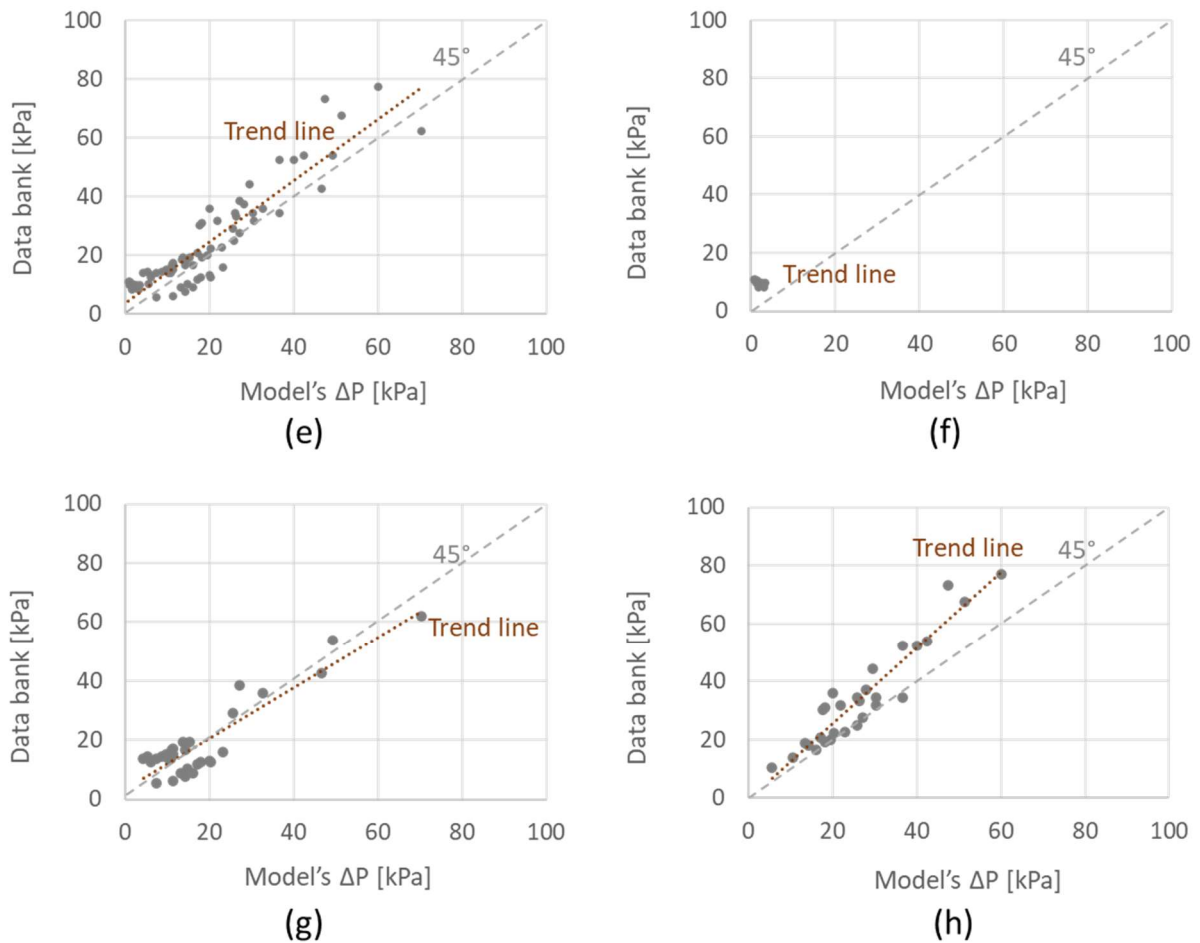


Figure 19 – Petalas and Aziz (2000) model's predictions compared with experimental data by Payne et al. (1979). (e) Full databank, (f) Stratified wavy flow pattern, (g) Intermittent (EB and S) flow pattern and (h) Annular-mist flow pattern.

After this evaluation is completed, it can be observed that the overall results supports higher accuracy of the model developed by Petalas and Aziz (2000). However, it is important to point out that specifically for stratified wavy flow pattern and intermittent, the model of Xiao et al. (1990) resulted in more accurate predictions in comparison to Petalas and Aziz (2000). Even though, more experimental data points should be explored in order to precisely evaluate each model's performance for different flow patterns. However, for the code operation, the implementation is considered validated by the trendline and the fact that the values observed for the errors match the performance reported in the literature.

4.2 SINGLE-PHASE VALIDATION OF PRESSURE DROP MEASUREMENTS

The first implication of this validation relies on the repeatability of measured pressure drop values. It is important to highlight that each measurement was performed at a frequency of 4 Hz during approximately 30 seconds given a steady-state circumstance. In sequence, the average value of differential pressure during this window was calculated resulting in one experimental point. In this way, seven experiments were carried out varying the flow rate and each one is repeated three times. Therefore, the differential pressure meter capacity of reproducing a measurement be evaluated.

As follows, results shown in Figure 20 demonstrate that for a constant value of water flow rate, this technique shows reasonable reproducibility accounting a maximum standard deviation of $\sigma_{dP} = 11$ Pa at the lower pressure drop measurement V1.

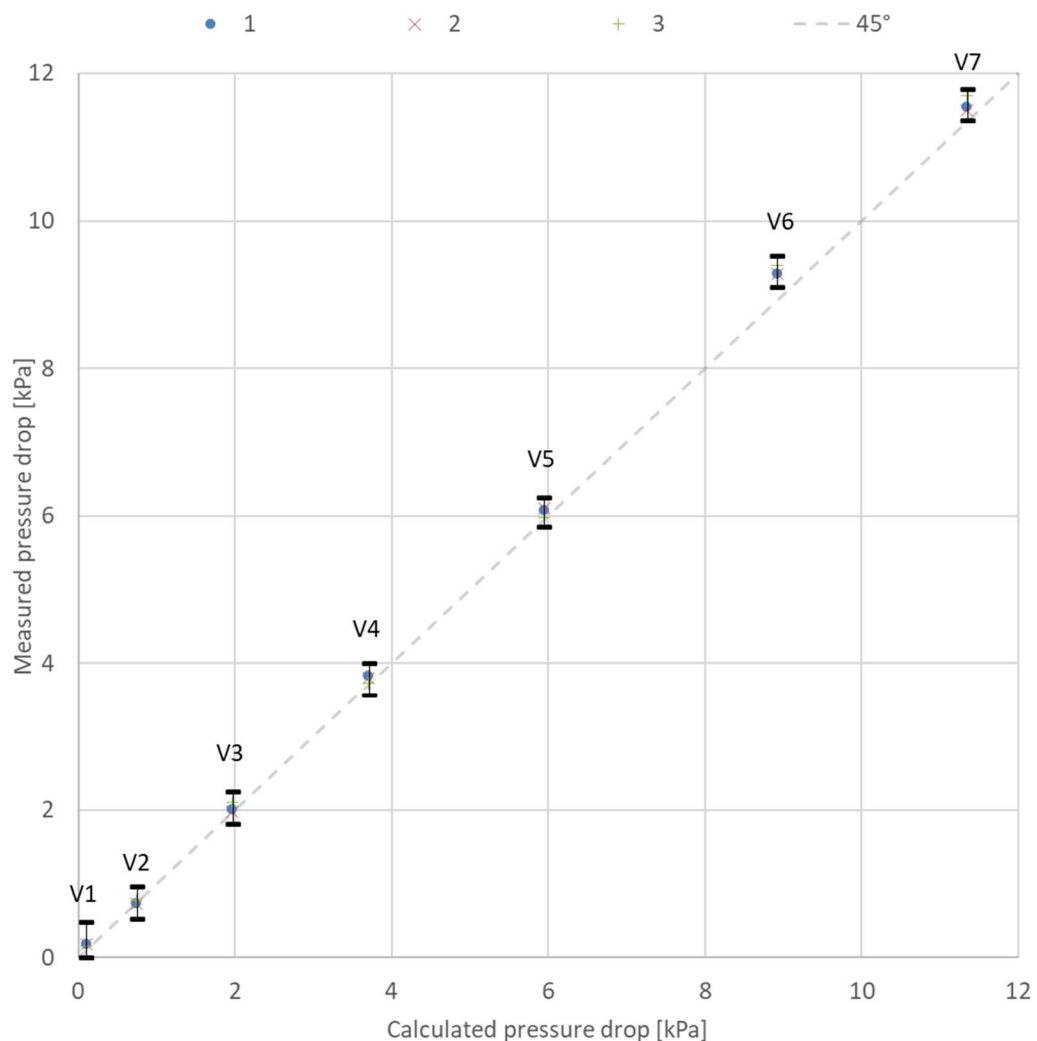


Figure 20 – Single-phase pressure drop measurements compared to calculated pressure drop.

In addition, the error bars of pressure drop for each flow rate is also compared to the predictions presented in Figure 20. In a general way, it is possible to infer that if the differential pressure meter's uncertainties are considered for this evaluation, 6 out of 7 experimental points demonstrated complete agreement with calculations and variabilities values are under uncertainty ranges. Such experimental points are defined in Table 7, considering the three measurements averaged value of pressure drop for each experimental point.

Table 7 – Pressure drop measurement for single-phase validation and pressure transducer uncertainty.

Experimental point	Measured ΔP [kPa]	Calculated ΔP [kPa]	Pressure transducer uncertainty [kPa]
V1	0.17	0.10	0.31
V2	0.76	0.75	0.22
V3	2.03	1.97	0.22
V4	3.78	3.71	0.22
V5	6.05	5.94	0.19
V6	9.32	8.92	0.21
V7	11.58	11.34	0.21

Furthermore, the measurement of experiment V6 is 2.03% higher than the predicted value considering the low end of the error bar, indicating that, possibly, one or more factors such as flange misalignment and absolute pipe wall rugosity may have affected the measured pressure drop. Even though, differential pressure intake configuration can be considered valid in terms of the general agreement of results and measurements.

Lastly, it is also important to highlight that the equation developed by Darcy-Weisbach apud Fox et al. (2014) is one of the most recommended techniques to calculate the friction loss and it provides a valuable estimation that can be used to project new equipment and predict the pressure drop in many situations. Moreover, using Colebrook implicit equation seems to be the best approximation of the friction factor (MINHONI et al., 2020). However, it still relies on the correct estimation of the pipe's wall roughness and equivalent length. As a result, it may account for higher error values depending on the facility's instrumentation, calibration process and available information of the circuit's hardware.

4.3 ESTIMATED AND ACTUAL OPERATIONAL RANGE OF NEMOG'S MULTIPHASE FLOW CIRCUIT

The procedure to determine the operational range of NEMOG's multiphase flow circuit is divided into three different steps. The first step consists in defining a region called theoretical operational capacity and it is correspondent to the area delimited by the operational range of single-phase flow meters. The second relies on the determination of the maximum pressure drop along the entire geometrical circuit domain (L) as estimated by the selected mechanistic models, which can be called estimated operational capacity or envelope. Results of this approach can be observed in Figure 21 to Figure 26. Lastly, the third step consisted of experimentally evaluate the maximum achievable superficial velocities following the planning showed in Table 5, resulting on the actual operational capacity or envelope.

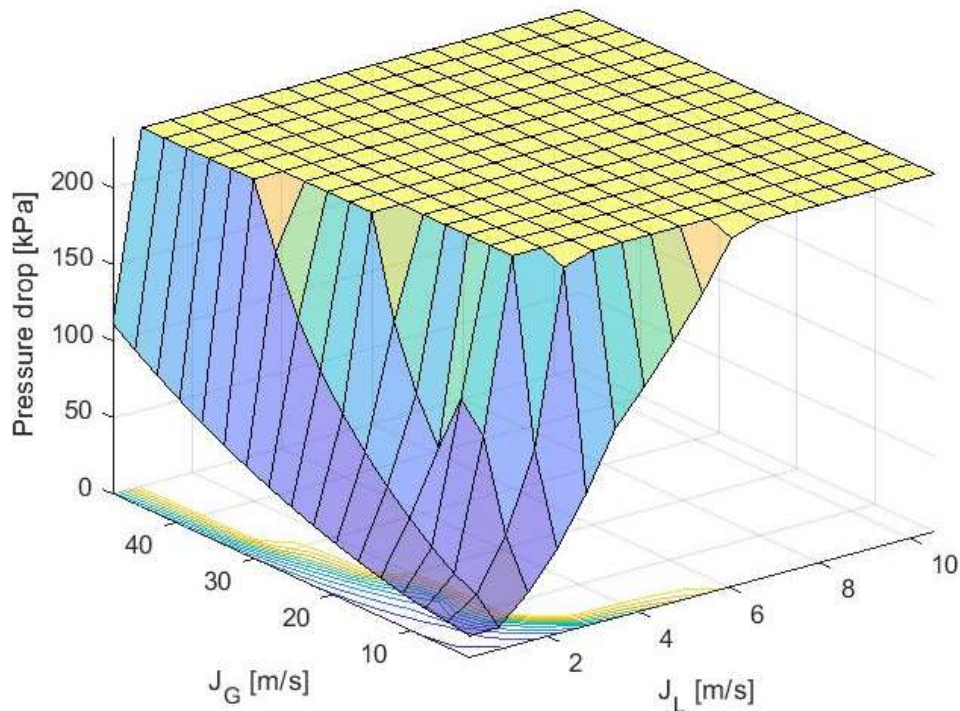


Figure 21 – Calculated pressure drop at $P = 270$ kPa by the model of Xiao et al. (1990) for all pairs of superficial velocities.

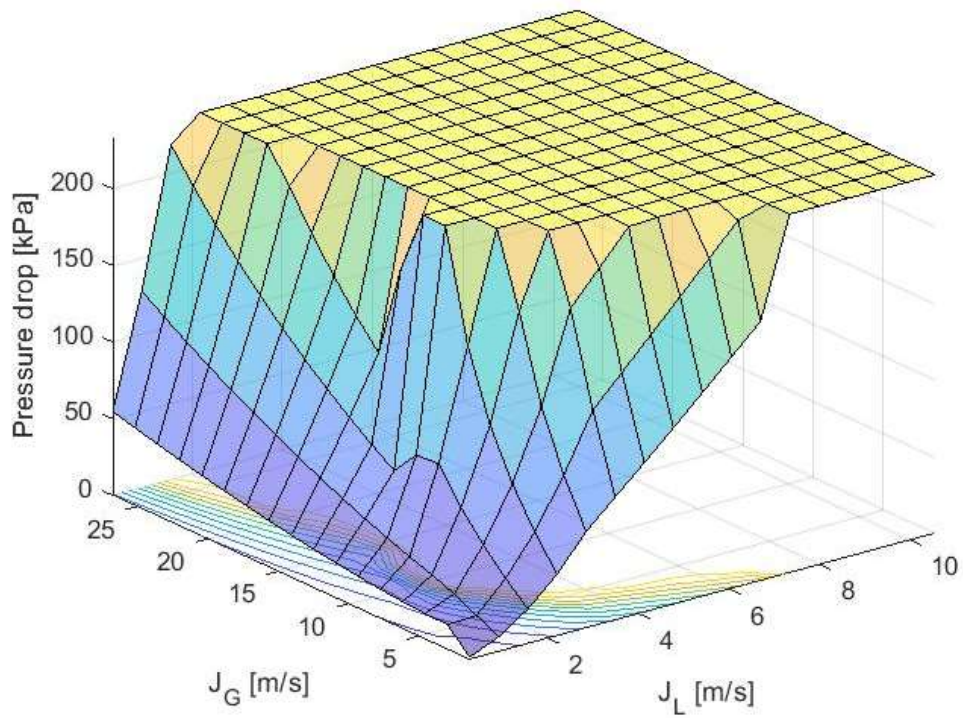


Figure 22 – Calculated pressure drop at $P = 485$ kPa by the model of Xiao et al. (1990) for all pairs of superficial velocities.

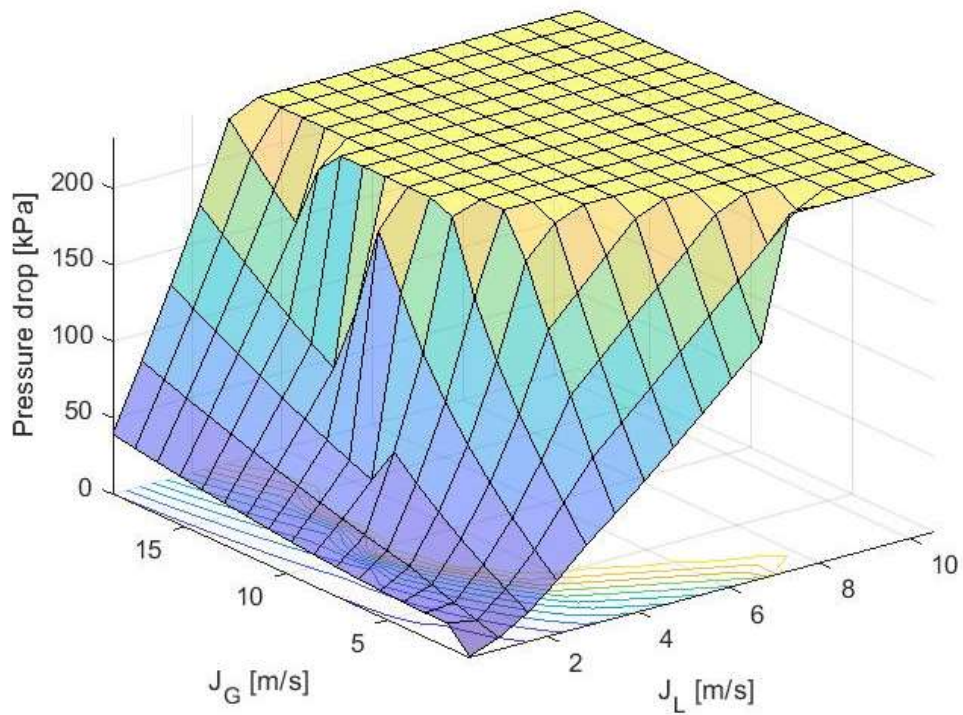


Figure 23 – Calculated pressure drop at $P = 700$ kPa by the model of Xiao et al. (1990) for all pairs of superficial velocities.

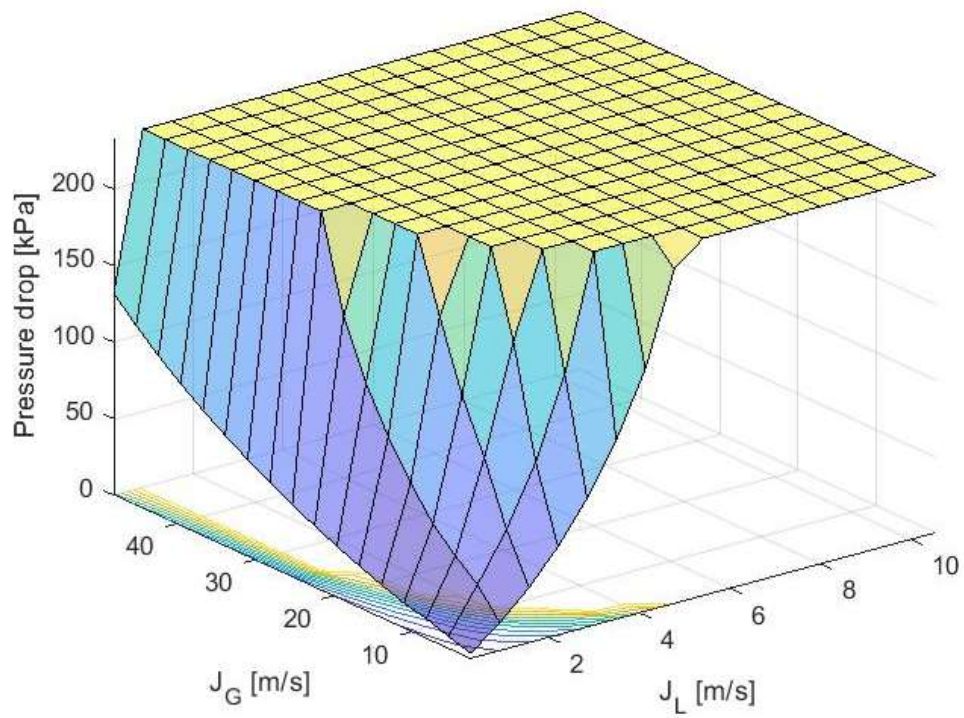


Figure 24 – Calculated pressure drop at $P = 270$ kPa by model the of Petalas and Aziz (2000) for all pairs of superficial velocities.

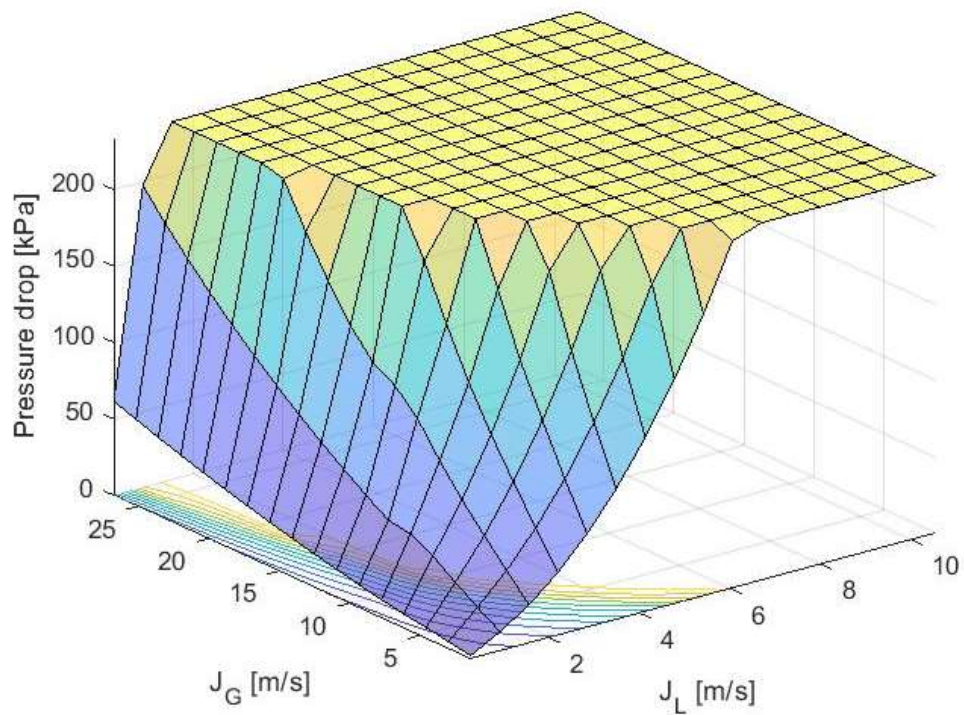


Figure 25 – Calculated pressure drop at $P = 485$ kPa by the model of Petalas and Aziz (2000) for all pairs of superficial velocities.

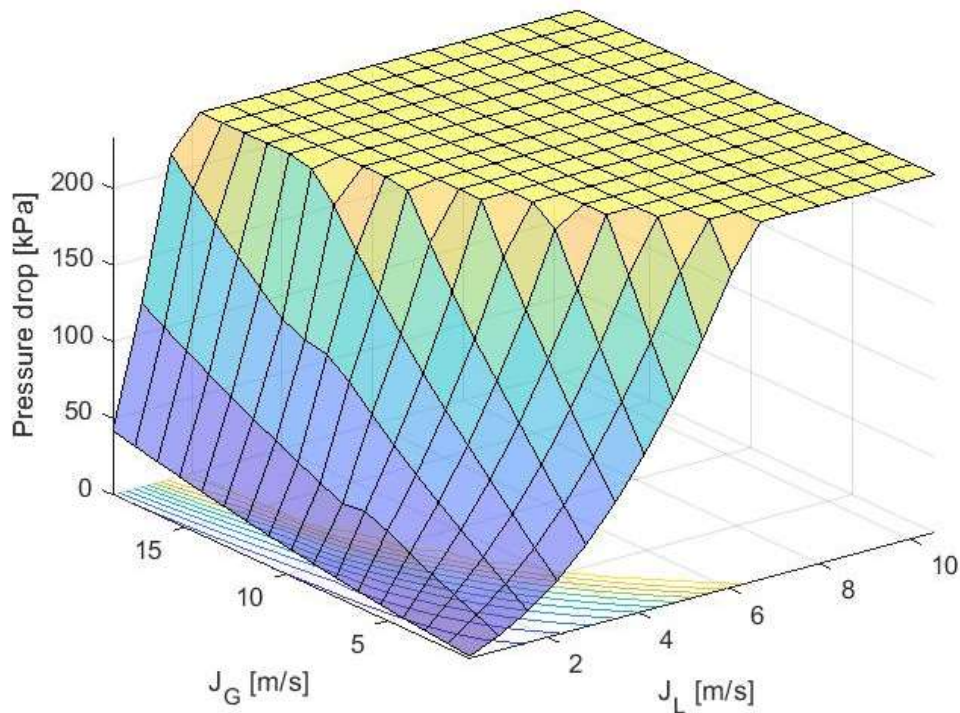


Figure 26 – Calculated pressure drop at $P = 700$ kPa by the model of Petalas and Aziz (2000) for all pairs of superficial velocities.

Evaluating the maximum achievable pressure drop predictions provided by mechanistic models, it is possible to identify that, for both models considered, increasing absolute pressure P causes reduction in the maximum gas superficial velocity J_G values. On the other hand, it is also observed a slight increase in liquid superficial velocity J_L . Considering that gas phase is under compressibility effects, it is expected that increasing density ρ_G , caused by pressure variation, may reduce the maximum achievable J_G .

Figure 27 to Figure 32 show all three approaches summarized in a single flow pattern map. The experimental points are represented by a mean value of superficial velocities of gas and water measured at 4 Hz by single-phase meters. Additionally, these measurements were recorded as soon as the flow achieved a permanent regime during a period of approximately 30 seconds.

In general, it can be observed that both models and pressure configurations resulted in experimental points and calculated ranges contained on the theoretical capacity area. Furthermore, for experimental points with high J_G and J_L , predictions provided by models overestimated pressure drop at $P = 270$ and 485 kPa by a maximum value of 71.33%, while underestimated at $P = 700$ kPa by 16.99%. On the other hand, situations containing the combination of one phase with high superficial velocity and the other with low, predictions can be considered underestimated at a maximum of 21.48%, even varying absolute pressure value.

In terms of interpreting results, it is important to highlight that the underestimation of pressure drop by a mechanistic model means that the calculated operational range contains flow rates for a pair of superficial velocities higher than experiments demonstrated (experimental points 6, 9 and 18). On the other hand, the overestimation implies that experimental superficial velocities achieved higher values if compared to the prediction provided by models (experimental points 3, 7, 12, 16, 21 and 25).

Given limitations of two-phase friction loss models on considering local pressure drop on curves, valves, flanges and meters, as well as the influence of those items on the current flow pattern, it is expected that some level of both under and overestimation may occur. However, results are in a considerably precise agreement with the experimental measurements, and it indicated that those tools can be used to model and predict an operational envelop for a specific application since limitations and a safety parameter is established.

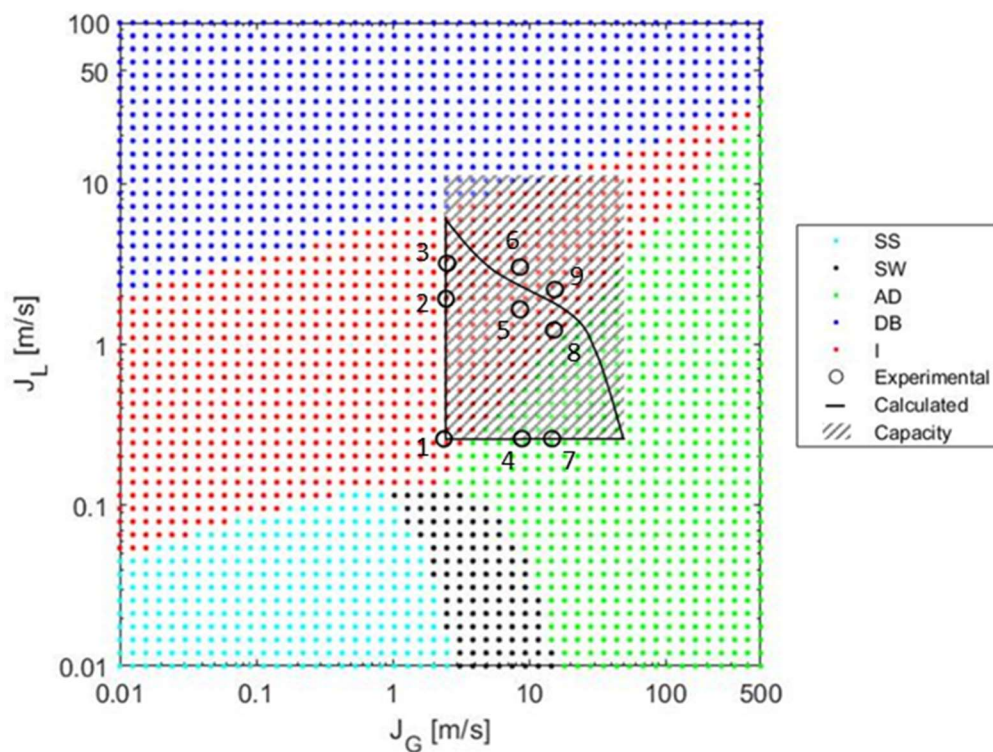


Figure 27 – NEMOG's envelop at $P = 270$ kPa for experimental points 1 to 9. Flow pattern map based on Taitel and Dukler (1976) and friction loss on Xiao et al. (1990).

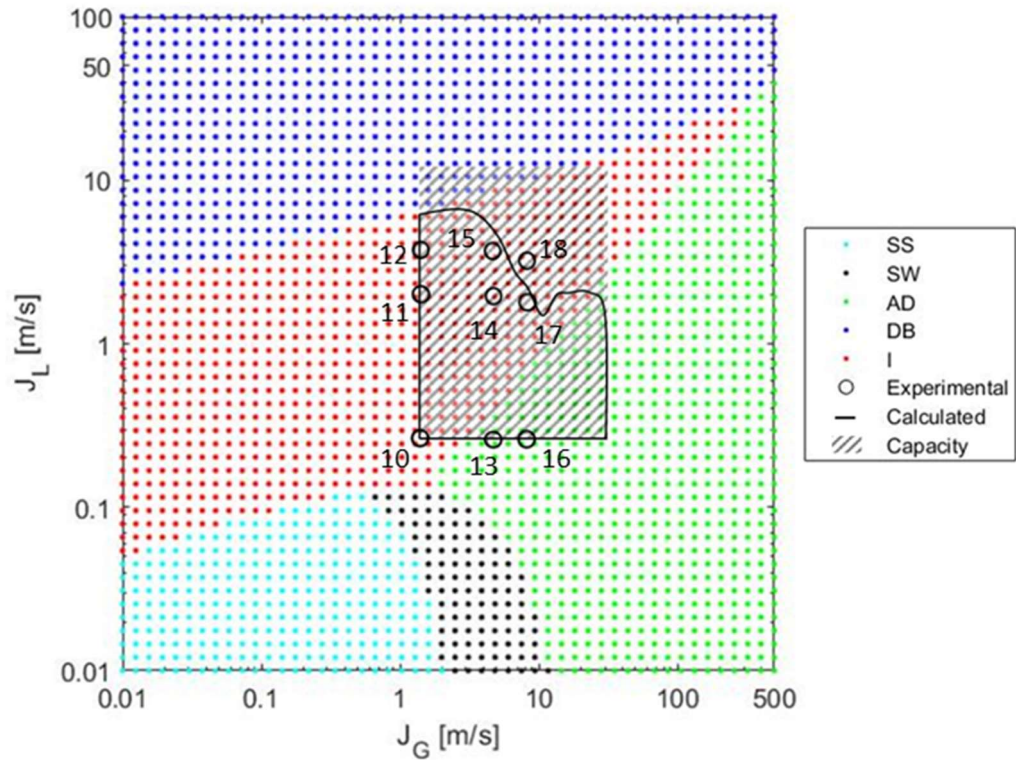


Figure 28 – NEMOG's envelop at $P = 485$ kPa for experimental points 10 to 18. Flow pattern map based on Taitel and Dukler (1976) and friction loss on Xiao et al. (1990).

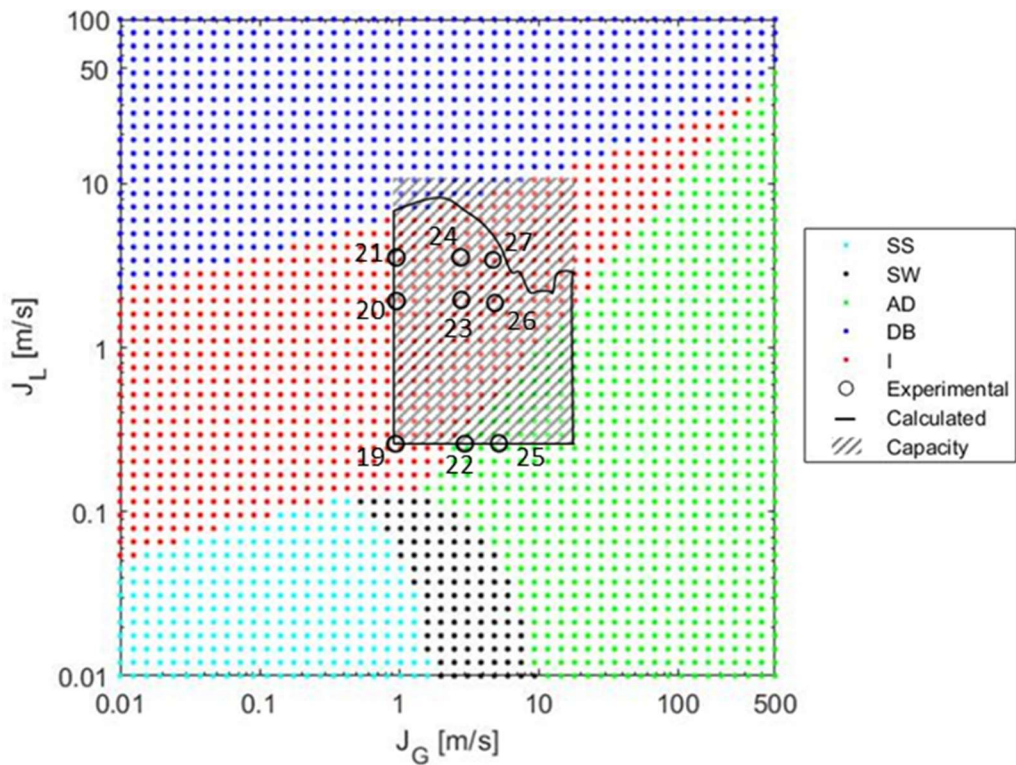


Figure 29 – NEMOG's envelop at $P = 700$ kPa for experimental points 19 to 27. Flow pattern map based on Taitel and Dukler (1976) and friction loss on Xiao et al. (1990).

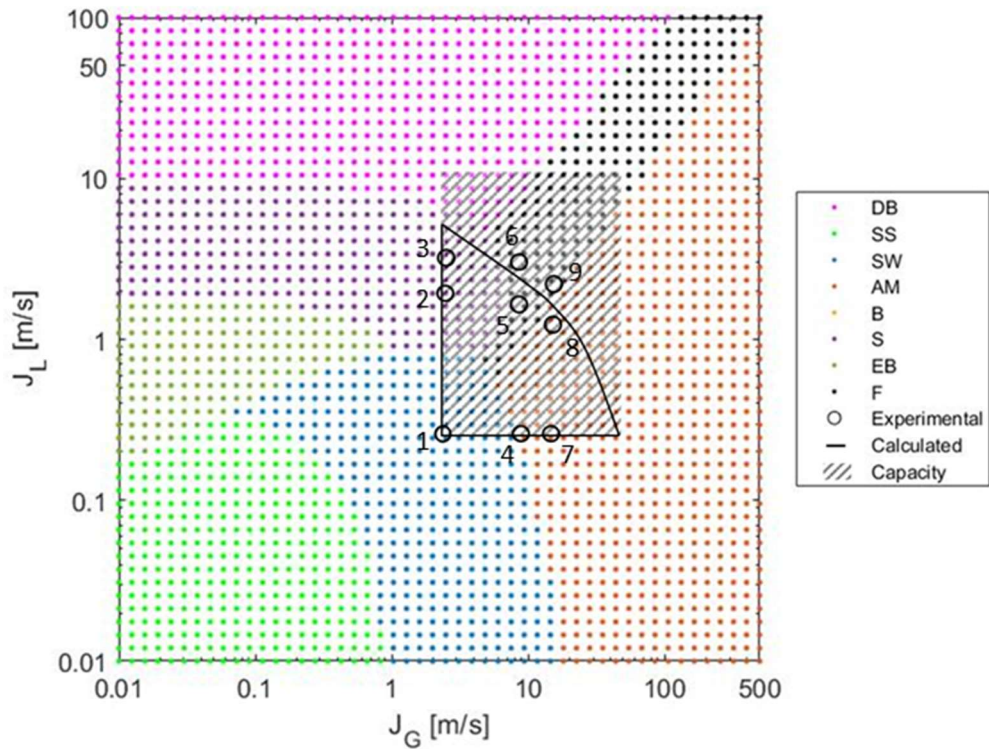


Figure 30 – NEMOG's envelop at $P = 270$ kPa for experimental points 1 to 9. Flow pattern map based on Petalas and Aziz (2000).

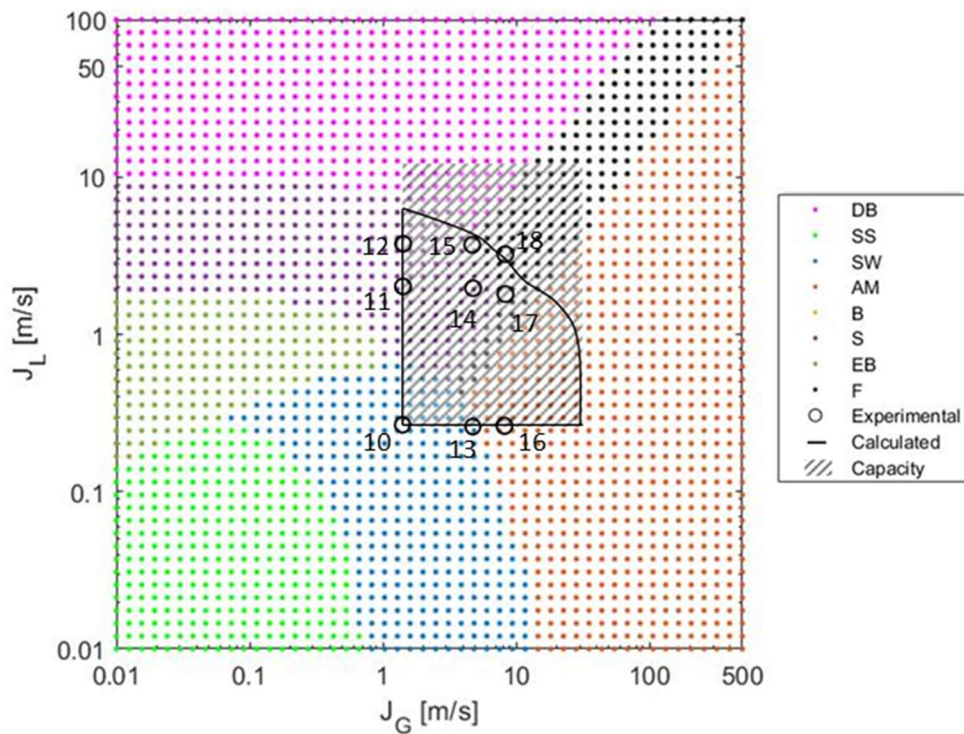


Figure 31 – NEMOG's envelop at $P = 485$ kPa for experimental points 10 to 18. Flow pattern map based on Petalas and Aziz (2000).

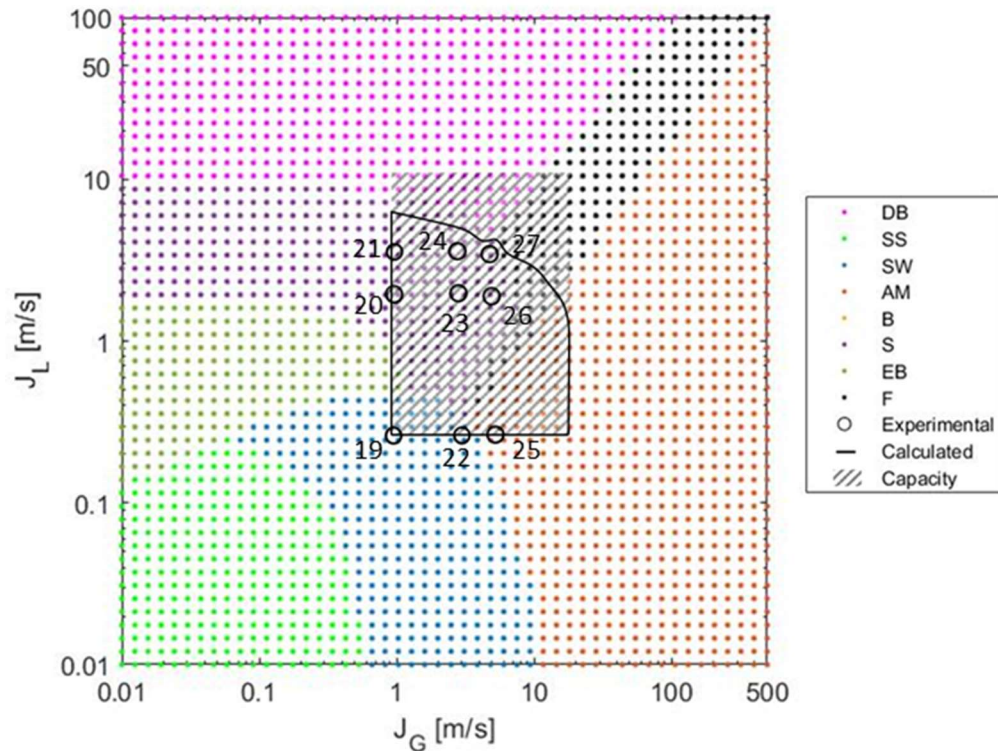


Figure 32 – NEMOG's envelop at $P = 700$ kPa for experimental points 19 to 27. Flow pattern map based on Petalas and Aziz (2000).

4.4 FLOW PATTERN MAP: VISUAL CLASSIFICATION AND PREDICTIONS PROVIDED BY MODELS

In order to test the effectiveness of the selected mechanistic models in predicting the flow pattern, those results are compared with visual observations and the consensus of three referees. It is important to emphasize that, as shown in

Figure 27 to Figure 32, experimental points are located near predicted flow pattern transition regions. Besides, many external factors such as roughness, curves, pressure taps, and flange misalignment may interfere on the flow pattern development inside the pipes. In sum, considering that models are not equipped with tools to account for these factors, it is expected that some results may not agree with observations, as listed in Table 8. Since this evaluation is subjective, the matches after comparison with visual classifications are taken as: total (X) or none (). In this way, scores are 24/39 for the model of Taitel and Dukler (1976) and 29/39 for the model of Petalas and Aziz (2000), indicating 12.8% more accuracy for the second one.

Table 8 – Flow pattern map prediction by models and visual classification.

Test	J_G [m/s]	J_L [m/s]	P [kPa]	Flow Pattern by Taitel and Dukler (1976)	Match	Flow Pattern by Petalas and Aziz (2000)	Match	Observed Flow Pattern [Author]
1	2.38	0.26	270	I		SW	X	SW
2	2.48	1.92	270	I	X	S	X	I
3	2.49	3.21	270	I	X	S	X	I
4	8.93	0.26	270	AD		AM		SW
5	8.63	1.64	270	I	X	F		I
6	8.57	3.03	270	I	X	F		I
7	14.77	0.26	270	AD		AM		SW
8	15.36	1.24	270	AD	X	AM	X	AM
9	15.47	2.19	270	I	X	F		I
10	1.40	0.26	485	I		SW	X	SW
11	1.40	2.02	485	I	X	S	X	I
12	1.43	3.77	485	I	X	S	X	I
13	4.76	0.26	485	AD		SW	X	SW
14	4.73	1.97	485	I	X	S	X	I
15	4.69	3.67	485	I	X	S	X	I
16	8.21	0.26	485	AD		AM		SW
17	8.35	1.79	485	I	X	F		I
18	8.19	3.24	485	I	X	F		I
19	0.96	0.26	700	I		SW	X	SW
20	0.97	1.91	700	I	X	S	X	I
21	0.97	3.51	700	I	X	S	X	I
22	3.00	0.26	700	AD		SW	X	SW
23	2.83	1.96	700	I	X	S	X	I
24	2.76	3.58	700	I	X	S	X	I
25	5.23	0.26	700	AD		AM		SW
26	4.92	1.86	700	I	X	S	X	I
27	4.74	3.43	700	I	X	S	X	I
28	2.55	0.26	270	AD		SW	X	SW
29	2.46	2.97	270	I	X	S	X	I
30	4.71	0.26	270	AD		SW	X	SW
31	4.73	2.98	270	I	X	S	X	I
32	2.48	0.26	485	AD		SW	X	SW
33	2.38	2.99	485	I	X	S	X	I
34	4.80	0.26	485	AD		SW	X	SW
35	4.81	2.98	485	I	X	S	X	I
36	2.57	0.27	700	AD		SW	X	SW
37	2.47	3.01	700	I	X	S	X	I
38	4.97	0.27	700	AD		AM		SW
39	4.74	2.99	700	I	X	S	X	I

Furthermore, it was observed that flow patterns may be classified differently depending on the person who is evaluating. One clear example of this situation relies on the subtle difference between stratified wavy (SW) and intermittent (I or S) flows near the transition boundaries. In this case, it is observed a stable stratified flow with interfacial perturbations, however, sporadically a single column of water can be recognized with non-periodical behavior. This same performance is also observed on the transition between annular and intermittent flows, where the first one is stably defined but perturbations in form of water column may occur. Lastly, it can be pointed out that since many mechanistic models relies on flow pattern definition for further pressure drop calculation, an additional error can be expected at transitional regions due to the wrong flow pattern configuration.

Considering the effect of absolute pressure variation on the predicted and observed flow pattern, experimental points 28-39 are examined. It is important to observe that pressure range details and further discussion of effects on pressure drop can be found in Figure 38. There are four groups of same superficial velocities defined as A (28, 32 and 36), B (29, 33 and 37), C (30, 34 and 38) and D (31, 35 and 39), according to grouping on Table 6. Also, it should be highlighted that absolute pressure values $P = 270$ kPa, $P = 485$ kPa and $P = 270$ kPa are, respectively, linked to the experiment number order for each defined group. In this way, for predictions provided by models, only group C presented a change in flow pattern from stratified wavy (30 and 34) to annular-mist (38), relying on results using the method proposed by Petalas and Aziz (2000). However, no substantial difference is visually noticed.

In general, it can be observed that the pressure variation may cause a displacement of the flow pattern map provided by models. However, during this experiment it was not noticed any significant evidence of pressure's influence on flow pattern for the selected pressure range. Despite that, it is important to emphasize that the challenge of maintain constant and same superficial velocities for different pressure ranges during the experiments was accomplished. Nonetheless, these velocities values may contain a slight variation, accounted for its maximum at 4.8%, and it may interfere on the model response.

4.5 TWO-PHASE FRICTION LOSS: COMPARISON BETWEEN MEASUREMENTS AND PREDICTIONS

After analyzing NEMOG's facility operational envelop at three different absolute pressures and comparing predicted flow pattern with a visual observation, this section confronts mechanistic models' predictions of pressure drop, and measurement provided by a differential pressure transducer. Differently from the flow circuit envelope estimation, these measurements are performed considering a straight pipe section with $L = 4.8$ m, aiming to reduce local pressure drop interferences.

To start, an overall performance evaluation is executed in terms of dispersion of predictions obtained by mechanistic models for all 39 experiments, as described in section 3.5. Additionally, it is highlighted that flow pattern and absolute pressure are not being variables of concern in this case and it represents a generalized result, as can be observed in Figure 33.

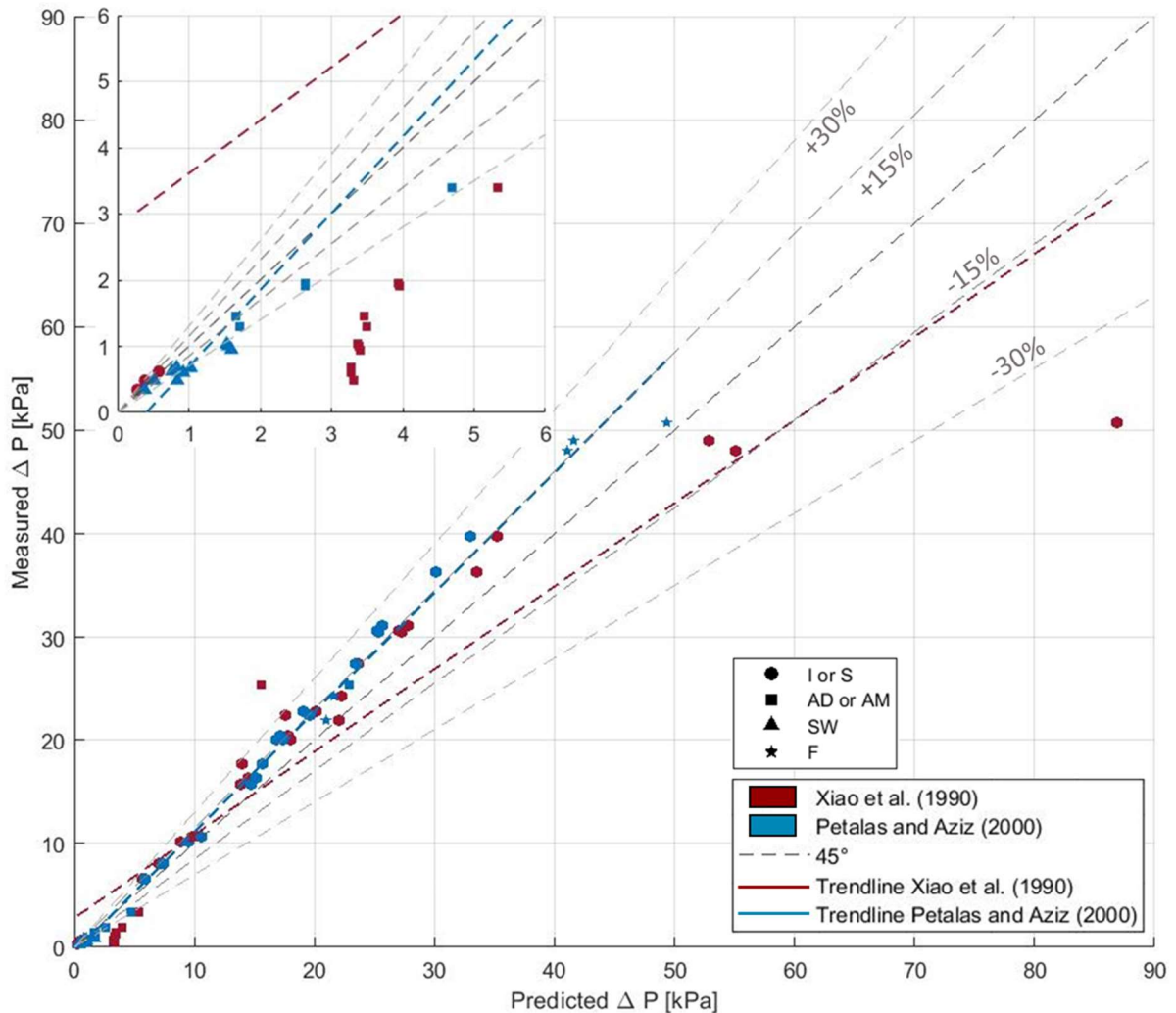


Figure 33 – Overall pressure drop predictions in comparison to measured values, considering all experimental points. Data segmentation according to mechanistic model and predicted flow pattern.

Considering an analysis containing all experimental points, the absolute relative error and standard deviation values are $E^{[X]}_{1-39} = 89.77\%$, $\sigma^{[X]}_{1-39} = 6.65$ kPa, $E^{[P]}_{1-39} = 21.91\%$ and $\sigma^{[P]}_{1-39} = 2.50$ kPa, for each model, respectively. It is clear that considering a superficial analysis, the model of Petalas and Aziz (2000) demonstrated a relative lower dispersion of the results, which can be confirmed analyzing Figure 34. Furthermore, 74.35% of results obtained by the model of Petalas and Aziz (2000) presents an error margin below $\pm 30\%$ while 46.15% of results are below $\pm 15\%$. In comparison, results obtained by the model of Xiao et al. (1990) are characterized by 64.10% of data points with error below $\pm 30\%$ and 53.85% below $\pm 15\%$.

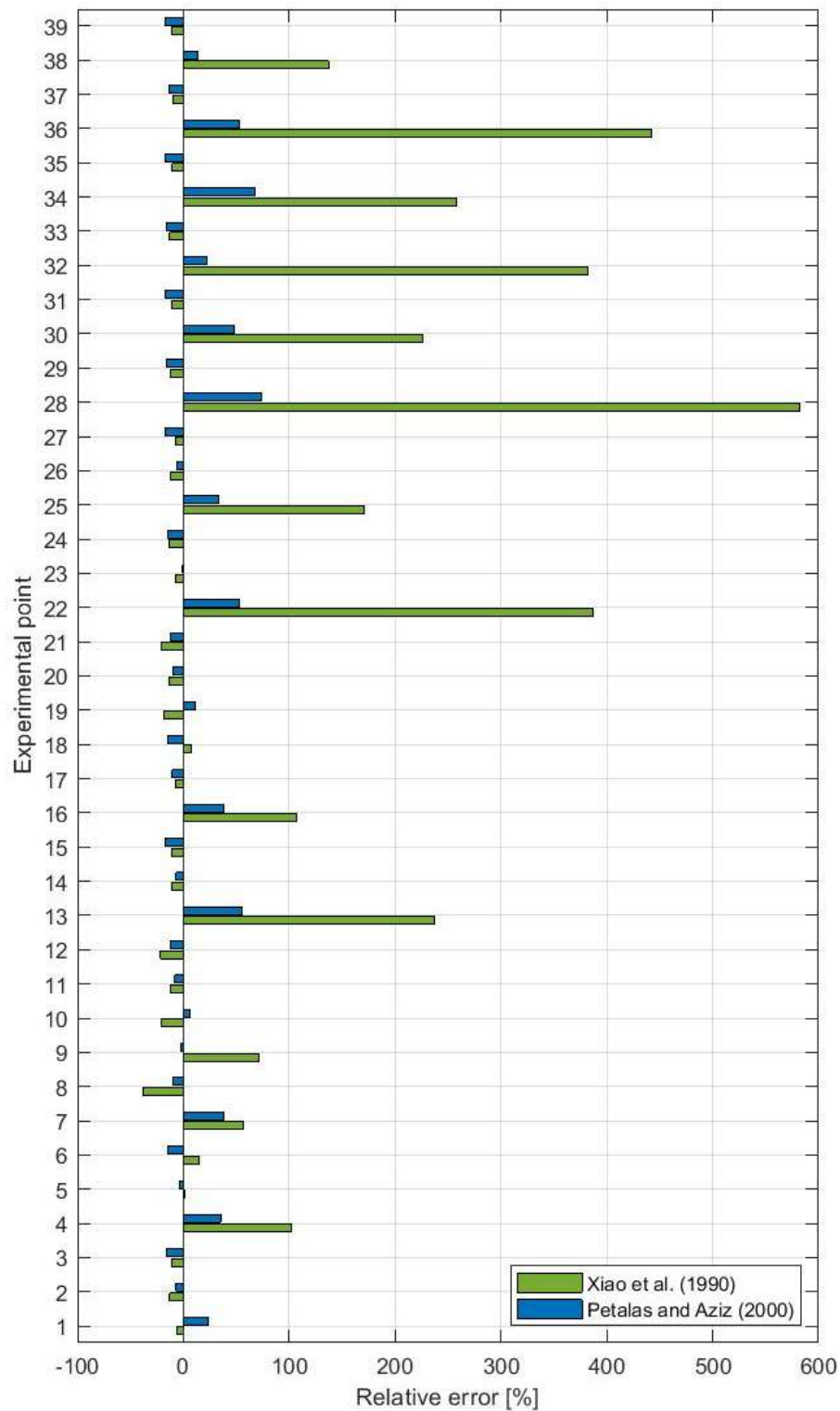


Figure 34 – Pressure drop relative error of Petalas and Aziz (2000) and Xiao et al. (1990) models predictions compared to experimental measurements.

Additionally, it indicates that two-phase pressure drop predictions are not as precise as single-phase ones, estimating by mechanistic models. Even though, depending on the facility or installation and selected method, it can be a good guess to provide significant information, that can be used to project machineries and forecast a physical phenomenon.

As mentioned, these experimental points consist in different flow pattern and pressure configuration, which may influence model performance. In this way, a more specific analysis is carried out relying on two different approaches, pressure influence and flow pattern influence. In terms of flow pattern attributes shown in Figure 33, it can be observed that most of experimental points consisting of errors above $\pm 30\%$ are characterized by annular dispersed (AD) liquid for the model of Xiao et al. (1990) and stratified wavy (SW) for the model of Petalas and Aziz (2000). Consequently, it can be understood that this variable represents an important parameter to be evaluated and it is further discussed in the flow pattern influence section.

Pressure influence

In order to evaluate the pressure influence on model performance and friction loss measurements, an analysis is developed based on same three absolute pressure levels as flow pattern predictions are analyzed. In this way, the first studied data contemplates experiments numbers 1-9, at absolute pressure $P = 270$ kPa, which is observed in Figure 35. In this absolute pressure configuration, both under and overestimation are present for model predictions and a trend can be observed. Considering the averaged absolute relative error and error standard deviation, calculations for pressure drop by the model of Xiao et al. (1990) gives $E^{XJ}_{1-9} = 35.02\%$ and $\sigma^{XJ}_{1-9} = 12.96$ kPa. On the other hand, those results estimated by model of Petalas and Aziz (2000) are $E^{PJ}_{1-9} = 16.72\%$ and $\sigma^{PJ}_{1-9} = 2.52$ kPa. Thus, indicating a better performance at the lower pressure configuration for the second one.

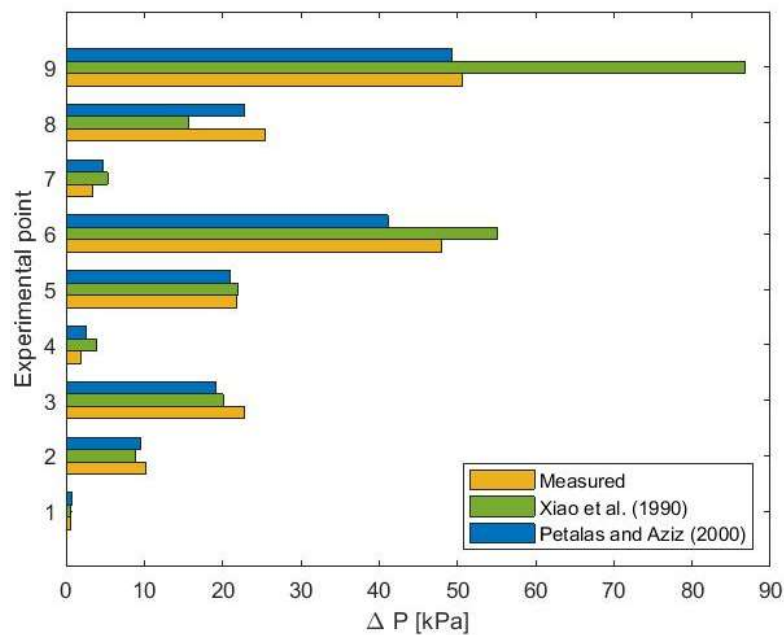


Figure 35 – Pressure drop at $P = 270$ kPa.

The same evaluation is applied for $P = 485$ kPa and can be observed in Figure 36. For this configuration, the first model performed with $E^{[X]}_{10-18} = 50.79\%$ and $\sigma^{[X]}_{10-18} = 2.99$ kPa while the second achieved $E^{[P]}_{10-18} = 17.24\%$ and $\sigma^{[P]}_{10-18} = 3.02$ kPa. Once again, Petalas and Aziz (2000) model presents better relative performance in terms of the magnitude of the relative error, however predictions dispersion can be considered similar.

Additionally, it can be observed that both authors' models resulted in an averaged absolute relative error higher if compared to results of $P = 270$ kPa while the standard deviation for the model of Xiao et al. (1990) reduced by a factor of 4. This realization may be correlated to flow patterns predicted in each absolute pressure range and respective method to estimate the pressure drop.

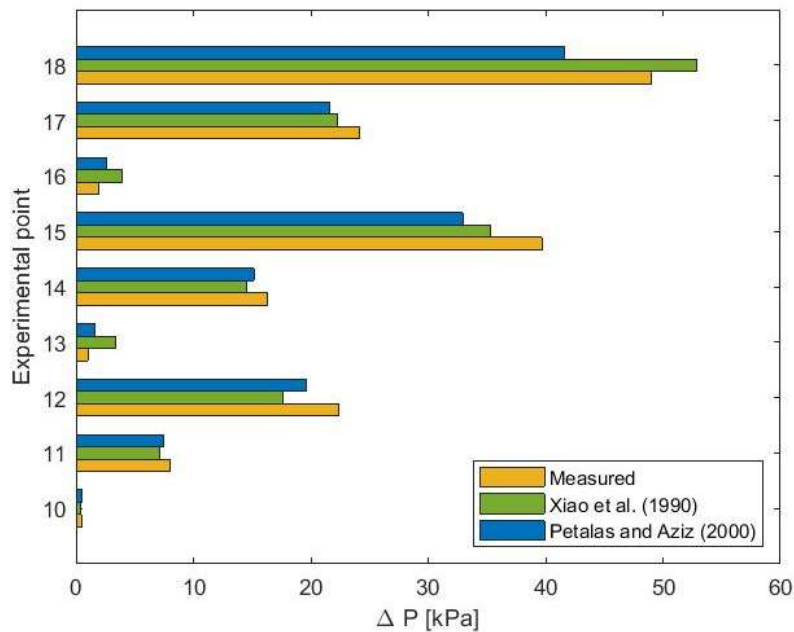


Figure 36 – Pressure drop at $P = 485$ kPa.

In sequence, experimental points of absolute pressure $P = 700$ kPa, shown in Figure 37, represent the maximum pressure range evaluated. As a result, $E^{[X]}_{19-27} = 72.50\%$ and $\sigma^{[X]}_{19-27} = 2.33$ kPa while $E^{[P]}_{19-27} = 17.68\%$ and $\sigma^{[P]}_{19-27} = 2.26$ kPa, indicating that the mechanistic model developed by Petalas and Aziz (2000), in general, performed better at the three pressure ranges evaluated considering only the absolute relative error. Moreover, Xiao et al. (1990) model maintains the trend of low dispersion as pressure is incremented, which may be also correlated to the reduction of maximum gas superficial velocity J_G and increase in gas density ρ_G .

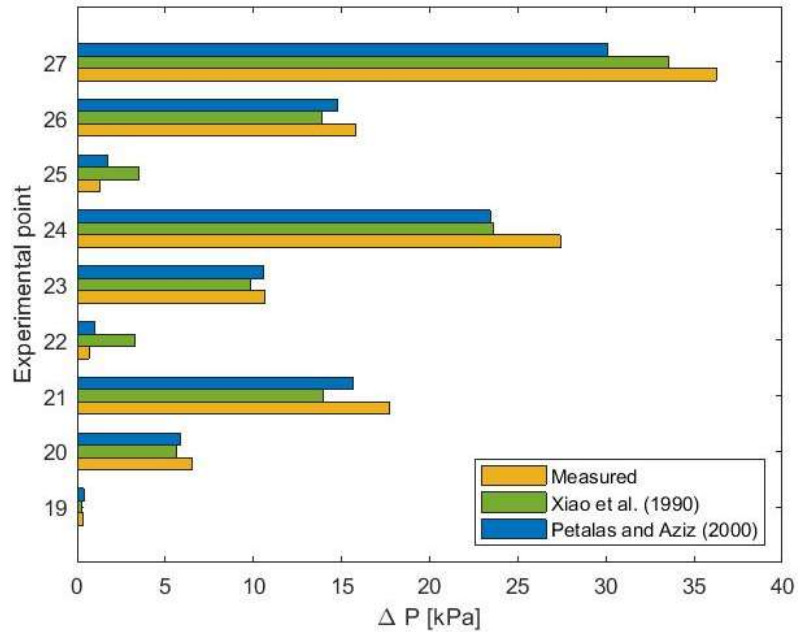


Figure 37 – Pressure drop at P = 700 kPa.

For the remaining 12 experimental points, the analysis is based on the evaluation of absolute pressure P on the friction loss predictions and measurements, given the same superficial velocity as indicated by letters A, B, C and D in Figure 38. For this assessment, averaged absolute relative error and error standard deviation are summarized on Table 9.

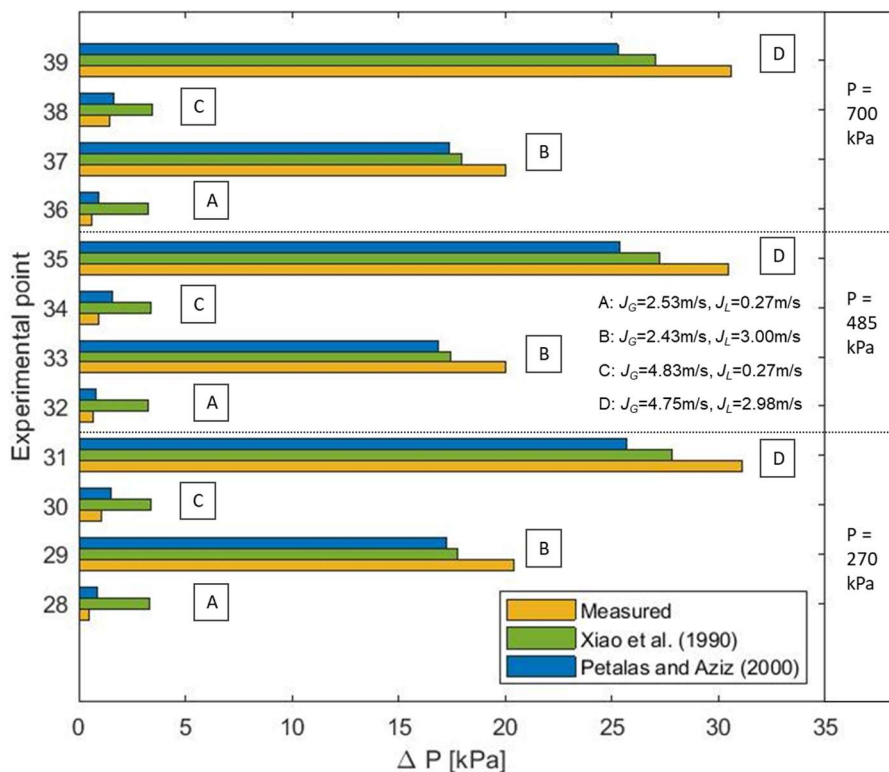


Figure 38 – Pressure drops at same superficial velocities. A) $J_G=2.53\text{ m/s}$ and $J_L=0.27\text{ m/s}$. B) $J_G=2.43\text{ m/s}$ and $J_L=3.00\text{ m/s}$. C) $J_G=4.83\text{ m/s}$ and $J_L=0.27\text{ m/s}$. D) $J_G=4.75\text{ m/s}$ and $J_L=2.98\text{ m/s}$.

Table 9 – Error and standard deviation of experimental points 28 - 39.

P [kPa]	Experimental point	$E^{[X]}$	$\sigma^{[X]}$	$E^{[P]}$	$\sigma^{[P]}$
270	28 - 31	208.02%	2.88 kPa	38.75%	3.21 kPa
485	32 - 35	165.83%	2.75 kPa	30.76%	3.15 kPa
700	36 - 39	150.34%	2.68 kPa	24.28%	3.04 kPa

Moreover, an additional analysis is conducted in order to account for the possible effect of absolute pressure variation on the measured pressure drop. This analysis contemplates the meter uncertainty for single-phase measurement as reference parameter and is shown in Figure 39. Comparing three differential pressure levels of each superficial velocities pair, the actual difference does not represent a trend. Additionally, the uncertainty range is over the measured differences for all cases and no conclusions can be made due to that.

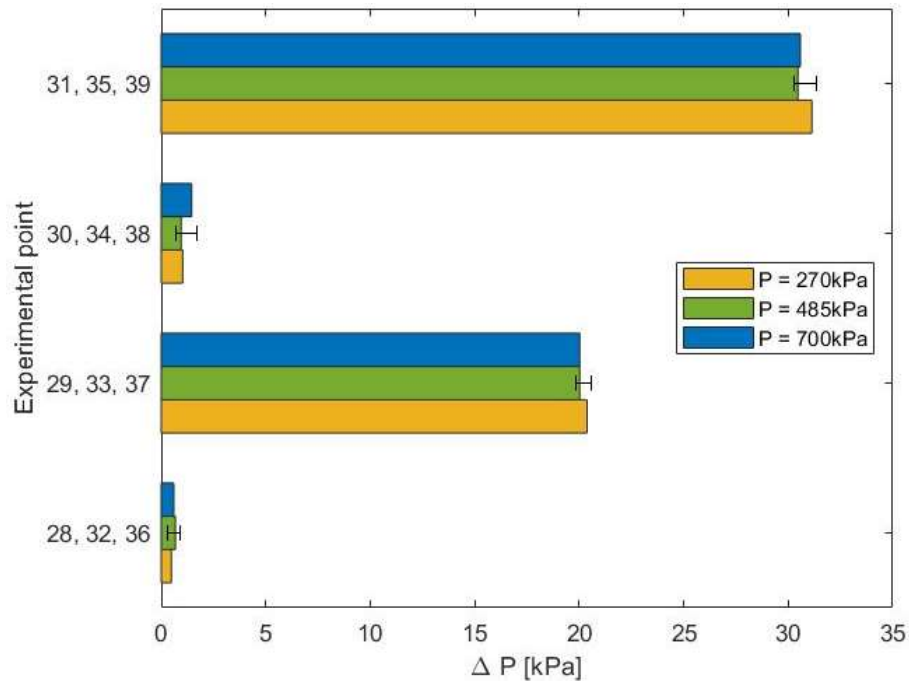


Figure 39 – Comparison of measured pressure drop considering same superficial velocities at different absolute pressure P .

Flow pattern influence

The flow pattern influence was primarily analyzed in terms of the pattern output from the selected models. In this way, Table 10 shows flow pattern as expected by each author, as well as the averaged absolute relative error and standard deviation.

Table 10 – Averaged absolute relative error and error standard deviation segmented on flow pattern determined by mechanistic models.

Flow pattern	$E^{[X]}$	$\sigma^{[X]}$	$E^{[P]}$	$\sigma^{[P]}$
AD or AM	240.62%	3.37 kPa	28.14%	1.35 kPa
S or I	14.34%	7.81 kPa	12.47%	2.01 kPa
F	-	-	9.33%	3.11 kPa
SW	-	-	41.47%	0.22 kPa

It is observed that the model of Xiao et al. (1990) resulted in elevated error values for experimental points tagged with annular-dispersed liquid (AD) compared to the annular-mist (AM) result of Petalas and Aziz (2000). It is also important to highlight that both mechanistic models relies on the solution of a two-phase momentum equation to determine pressure drop for annular flow pattern. Additionally, those depend on empirical correlations to calculate the fraction entrainment (FE) into the gas core and interfacial friction factor (f_i) as enclosing relationships. Consequently, precision of results may be related to the amount, variety and quality of data used to develop these empirical correlations. It was also found out that the fraction entrainment correlation used by Xiao et al. (1990) on the correspondent model was developed by Oliemans et al. (1986) for two-phase annular vertical flows while the referred model estimates pressure drop for horizontal configurations, which can be directly associated to correspondent performance issues. On the contrary, empirical relationships employed by Petalas and Aziz (2000) were developed based on a large amount of experimental data containing multiple slopes, flow rates and pressure ranges.

In terms of intermittent flow pattern (I or S), both models outputs demonstrate satisfactory precision compared to the experimental measurements, with great increase in performance for the model of Xiao et al. (1990). Moreover, froth and stratified wavy patterns were only predicted by Petalas and Aziz (2000)'s model. For the first mentioned flow pattern, predictions represented the best registered results, while stratified wavy ones revealed the most elevated absolute relative error and lower standard deviation values, indicating a possible systematic error for this flow pattern, of this analysis regarding this author's model.

Furthermore, models' performance are also evaluated in terms of predicted flow pattern matched with visual observations (Table 8). This investigation is carried out splitting the averaged absolute relative error and error standard deviation into two different groups of experimental points, those in which the predicted flow pattern agrees with respective authors' classifications and those which does not, for both Xiao et al. (1990)'s and Petalas and Aziz (2000)'s models. After analyzing Table 11, it can be understood that for results obtained by the model of Xiao et al. (1990), correct flow pattern prediction seems to be essential for better performance. Besides, it is highlighted that 12/15 of non-matching experimental points are classified as AD by the algorithm, reinforcing that this flow pattern approach may be limited for specific

configurations. On the other hand, matches are represented by 23/24 of intermittent patterns, which are characterized by best performance of this model on Table 10. Considering this time predictions of Petalas and Aziz (2000)'s model at the experimental points analyzed, the agreement with visual observations indicates no relevant difference in performance. At last, it is pointed out that all experimental points are located at flow pattern transition regions. Therefore, this evaluation represents the performance on NEMOG's multiphase flow circuit and only at the current operational range. It is possible that, at lower or higher superficial velocities, different pressure range and selected fluids, in which flow patterns are solidly defined, both model's performance may differ from those found.

Table 11 – Averaged absolute relative error and error standard deviation based on models' flow pattern predictions in agreement with observations.

Match	$E^{[X]}$	$\sigma^{[X]}$	$E^{[P]}$	$\sigma^{[P]}$
Yes	15.22%	8.38 kPa	22.38%	2.29 kPa
No	209.04%	1.03 kPa	20.55%	3.15 kPa

4.6 CODE PARAMETERS PERFORMANCE FOR IMAGE PROCESSING IN TERMS OF FREQUENCY SHIFT TECHNIQUE

Before processing all recorded videos, an evaluation of the best distance between ROI A and B is accomplished. As discussed before, measured shift's response is expected to have a linear behavior if the distance is changed, and the measured gas velocity should be noticed as constant. In this way, Figure 40 represents these parameters considering an intermittent flow pattern, referring to the data collected from experimental point 14.

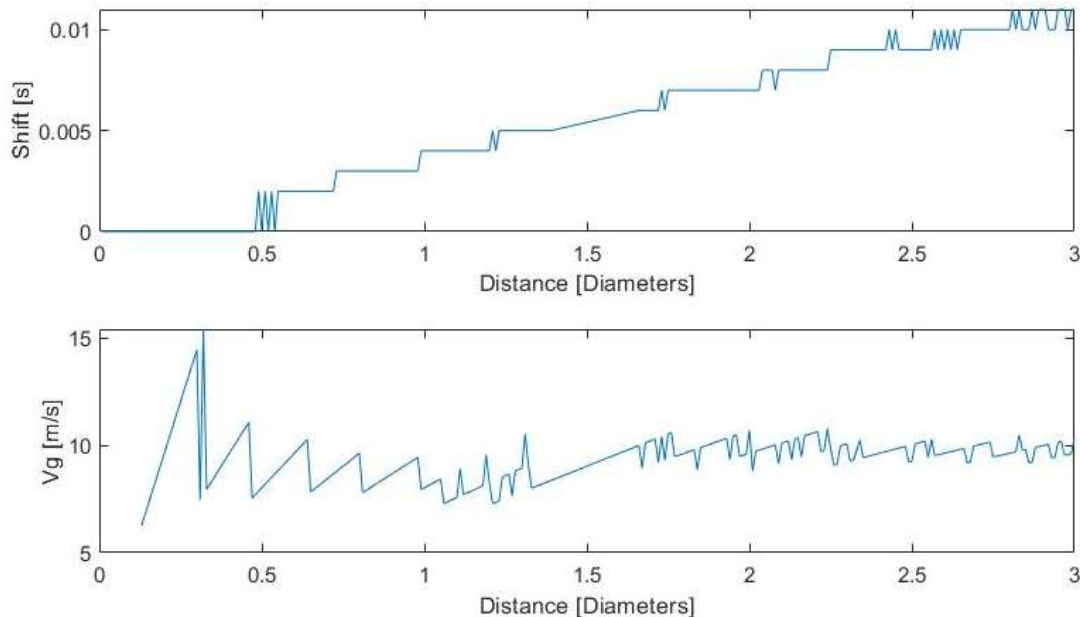


Figure 40 – Evaluation of signal shift and gas velocity over distance.

As observed, at distances below $1D$ the gas velocity demonstrated unstable results and the shift reached zero, while for distances above $2.5D$ shift results does not present a linear trend. After this realization, it was defined two diameters ($2D$) as a standard distance value for data acquisition of recorded videos. Lastly, it is also important to highlight that at distances between 1.35 and $1.65D$ there are points with no data due to the metric scale used during experiments. Consequently, this range is not accounted for this task.

Furthermore, it can be highlighted that experimental points 19, 30, 32, 28, 11, 10, 2, 5, 20, 23, 14 and 17 were submitted to this analysis and the same behavior is observed. It was also noticed that for less intermittent flows (19, 30, 32, 28 and 10) shorter distances ($<2D$) resulted in consistent linearity for shift's measurement and constancy for measured velocity. On the other hand, for highly intermittent flows (11, 2, 5, 20, 23, 14 and 17) distances shorter than $2D$ considerably affected the expected behavior. As a result, it can be inferred that a hardware capable of recording at higher resolution (spatial and temporal) may be suitable to collect data at shorter distances.

4.7 ROI OUTPUT

Considering the ROI output data and in terms of the liquid height over time h_i , gas velocity by geometrical approach V_G and gas velocity by frequency shift V_{G_s} , there are some observed situations that the algorithm poorly performed. Consequently, those experimental points were eliminated from the first part of this analysis. However, possible causes are indeed discussed, and selected points are shown on Table 12.

The first case relies on high liquid height (mostly higher than $0.8D$) in which during experiments, it could be noticed that water formed a liquid film on the pipe's wall avoiding the passage of background light. Thus, collected liquid height values are predominantly over measured and do not represent the flow itself. It can be pointed out that some of the developments found in the literature, such as Dinaryanto et al. (2016), Do Amaral et al. (2013) and Morales (2011) used translucent water during experiments for two-phase flows image processing techniques. On the other hand, the current development adopted a brown-yellow colored water, what may have increased the background light attenuation and contributed to decrease in contrast between phases.

Additionally, this error is also increased by the passage of small bubbles that often were not recognized by the code due to its low contrast compared to the water. This observation is also made by Zhou and Niu (2020) while measuring bubble size for situations in which bubbles are overlapped and some of them are not accounted for. Zhou and Niu (2020) recognized that the method is of great significance but has limitations. Considering the present work, averaged void fraction $\langle \alpha_G \rangle$ is underestimated and gas velocity by geometrical approach V_G is overestimated, since a reduction in area for the same flow rate imply that the velocity must increase. A

possibility to mitigate this effect may consist in use clear water and to investigate the entire height for each frame (not only until the interface is recognized).

For the technique using frequency shift, it is noticed that some experimental points resulted in stratified wavy flow patterns and some of them did not account for any passage of a water column. Since this part of the algorithm is specifically developed to work on intermittent flows and depends entirely on the transit time of this column, it resulted in a slug frequency of $\langle f \rangle_{slug} = 0$. Therefore, V_{G_s} could not be estimated. However, the geometrical approach seems to give precise measurements of liquid height in stratified flows.

Additionally, it is observed that at higher flow rates (both water and air) the turbulence seems to morphologically change shapes of the flow between ROI A and B. In this way, the collected transit time between those water columns could not be considered as the actual gas phase velocity. Lastly, comparable to the geometrical approach when the liquid height is considerably high, passage of dispersed small bubbles are not accounted as variations over time in h_i (which is also overestimated) and indeed not considered into the signal shift.

Table 12 – Selected experimental points based on accuracy criteria ($E_{V_{Gs}}$).

Experimental point	V_G [m/s]	V_{G_s} [m/s]	$E_{V_{Gs}}$	$\alpha_{G_{ref}}$	α_{G_h}	α_{G_s}	$\langle h \rangle / D$
19	1.62	1.61	0.60%	0.79	0.59	0.59	0.43
30	6.25	5.72	9.33%	0.95	0.75	0.82	0.29
32	3.70	3.32	11.36%	0.90	0.67	0.75	0.36
28	3.52	3.05	15.29%	0.91	0.72	0.83	0.33
11	5.17	4.21	22.92%	0.41	0.27	0.33	0.71
10	2.29	1.74	31.60%	0.84	0.61	0.80	0.41
2	7.76	5.43	42.72%	0.56	0.32	0.46	0.67
5	18.43	11.64	58.34%	0.84	0.47	0.74	0.54
20	5.58	3.44	62.55%	0.34	0.17	0.28	0.80
23	10.01	5.96	68.12%	0.59	0.28	0.48	0.70
14	14.19	8.23	72.40%	0.71	0.33	0.57	0.66
17	22.41	12.34	81.62%	0.82	0.37	0.68	0.63

As a result, this section presents the analysis on experimental points with less than 100% relative error (E_{VGS}) between V_G and V_{G_s} . For comparison purposes, experimental points showed are sorted from the lower relative error E_{VGS} to the higher. Nonetheless, $\alpha_{G_{ref}}$, α_{G_h} and α_{G_s} represent, respectively: injection void fraction, measured void fraction by geometrical approach and void fraction obtained as result of gas velocity by shift technique V_{G_s} .

After analyzing results presented on Table 12, it is noticeable that the increase in value of measured gas velocities V_G and V_{G_s} , in general, seems to be correlated to a higher relative error E_{VGS} . This observation reinforces the argument that the algorithm performance is affected by turbulence and morphological shape changes of the air-water interface between ROI A and B. Furthermore, mostly at low average liquid level $\langle h \rangle_L/D$ (experimental points 19, 30, 32 and 28), the relative error E_{VGS} does not exceed 20%. As a result, it can be understood that high liquid levels are associated with less light passage and consequently low code's performance.

Height over time

As videos of selected experimental points are processed, the first output value of height over time h_i is collected. In sequence, the entire array is plotted using blue pixel values of ROI B (correspondent to the region in which height is measured), as shown in Figure 41. This comparison allows an evaluation of follow-up capacity, given the threshold value used for binarization in each situation. Additionally, this approach is used for all experimental points to evaluate the best threshold value that corresponds to the most real liquid level.

In a general way, it can be observed that the algorithm is able to properly reproduce the height of the interface between air and water for different flow patterns. It can also be noticed that high liquid and gas superficial velocities are remarked by dispersed liquid droplets (points 5, 14 and 17) that are not measured by the algorithm, representing a potential limitation of the code. Consequently, higher uncertainties are expected on these experimental points.

Additionally, those plots provide a possibility of re-evaluating the defined flow pattern determined by visual observations, as defined in Table 8. In this way, experiments 19, 30, 32, 28 and 10 can be identified as predominantly stratified wavy, however, containing one or two passages of water columns (but not with a defined periodic characteristic). On the other hand, 11, 2, 5, 20, 23, 14 and 17 have most of intermittent aspects, including: periodic large bubbles and columns of water. Thus, those points can be indeed classified as intermittent (I). As a result, it reinforces that flow pattern classification is considerably subjective given a visual classification in comparison with the predictions provided by mechanistic models.

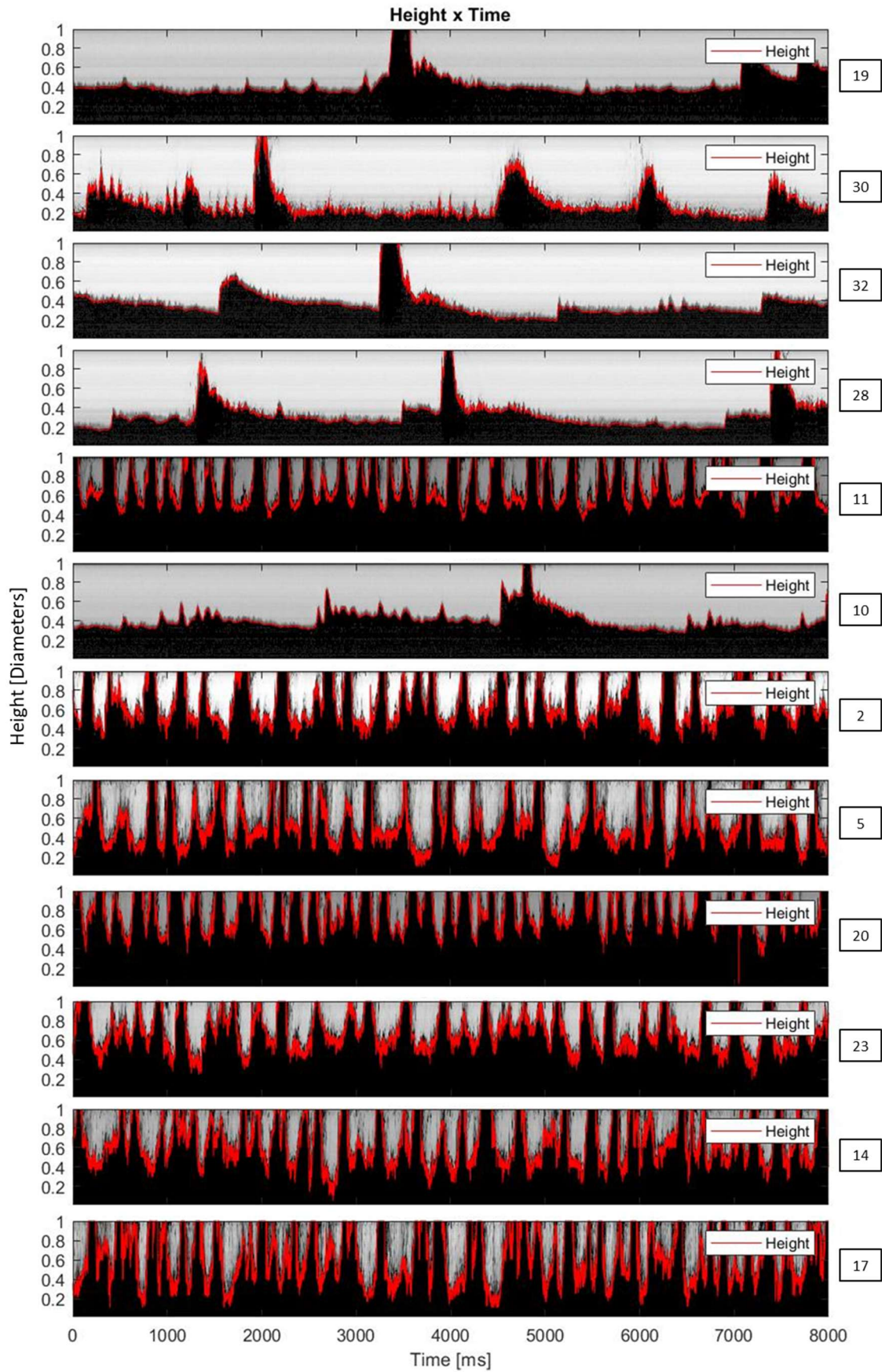


Figure 41 – Height over time (red line) and video integration (background) comparison for selected experimental points (Table 12).

Gas velocity: geometrical approach and frequency shift

Since the geometrical approach depends only on the correct measurement of the liquid height, it is considered that the most precise values of V_G are the ones in which high contrast and low liquid level occurs (19, 30, 32, 28 and 10) for experimental points on Table 12. However, regarding the efficiency of the algorithm in terms of achieving similar gas velocities by both techniques, it is important to note that results showed in Figure 41 are sorted by the relative error $E_{V_{GS}}$ between V_G and V_{G_s} , from the lower to the highest values. In this way, it can be observed that the most precise responses are linked to a small number of flow perturbations with lower averaged liquid level. These factors may contribute to a cleaner visualization of the flow due the higher contrast and consequently, an accurate value of height could be measured. Furthermore, despite the frequency shift technique dependence on accuracy of liquid height, it is also influenced by the correct reproduction of the flow on ROI A and B. Therefore, it is expected that the higher turbulent intensity the flow has (or even more frequent slug occurrences), more uncertainty this measurement may contain. This realization can be noticed evaluating $E_{V_{GS}}$ along with the last five results in Figure 41, in which more interfacial fluctuations are present and dispersed liquid is observed in the gas region.

Considering now the shift technique, in general, increasing flow velocities causes the events collected from ROI A and B to occur closer, consequently, the temporal resolution of videos might be also considered as a limitation and possible source of errors. For the sake of this evaluation, Figure 42 illustrates both height values used to estimate the gas velocity V_{G_s} plotted on the same graphs. It can be observed that the most precise outputs are linked to a defined passage of a column of water and correspondent geometry on both ROIs. Oppositely, flows with more perturbations (cases 2, 5, 20, 23, 14 and 17) and consisting of a narrower interval between events are remarked by higher errors. At last, experiment 17 contains an example of a possible mismatch between ROIs at approximately 1.8 and 2.8 seconds. In this case, liquid height measured by ROI A may be recognized as the passage of a column of water while liquid height by ROI B does not reach the top of the pipe, thus, this event might not be accounted for the signal binarization process at height B.

In terms of the binary height directly used for the gas velocity V_{G_s} estimation, Figure 43 shows obtained results after the signal is processed using averaged moving and high pass filters. It can be observed that for the first six best results ($E_{V_{GS}} < 40\%$), signals matches 100% from regions A and B. Additionally, the best four ones are remarked by two or less slug occurrences. On the other hand, higher error results are characterized either by an extreme short distance between signals (5, 23, 14 and 17) or at least one mismatch (2, 20, 23, 14 and 17). Furthermore, despite experimental points 11 and 10, high turbulent intensity and elevated slug frequency seem to lead to lower agreement between V_G and V_{G_s} .

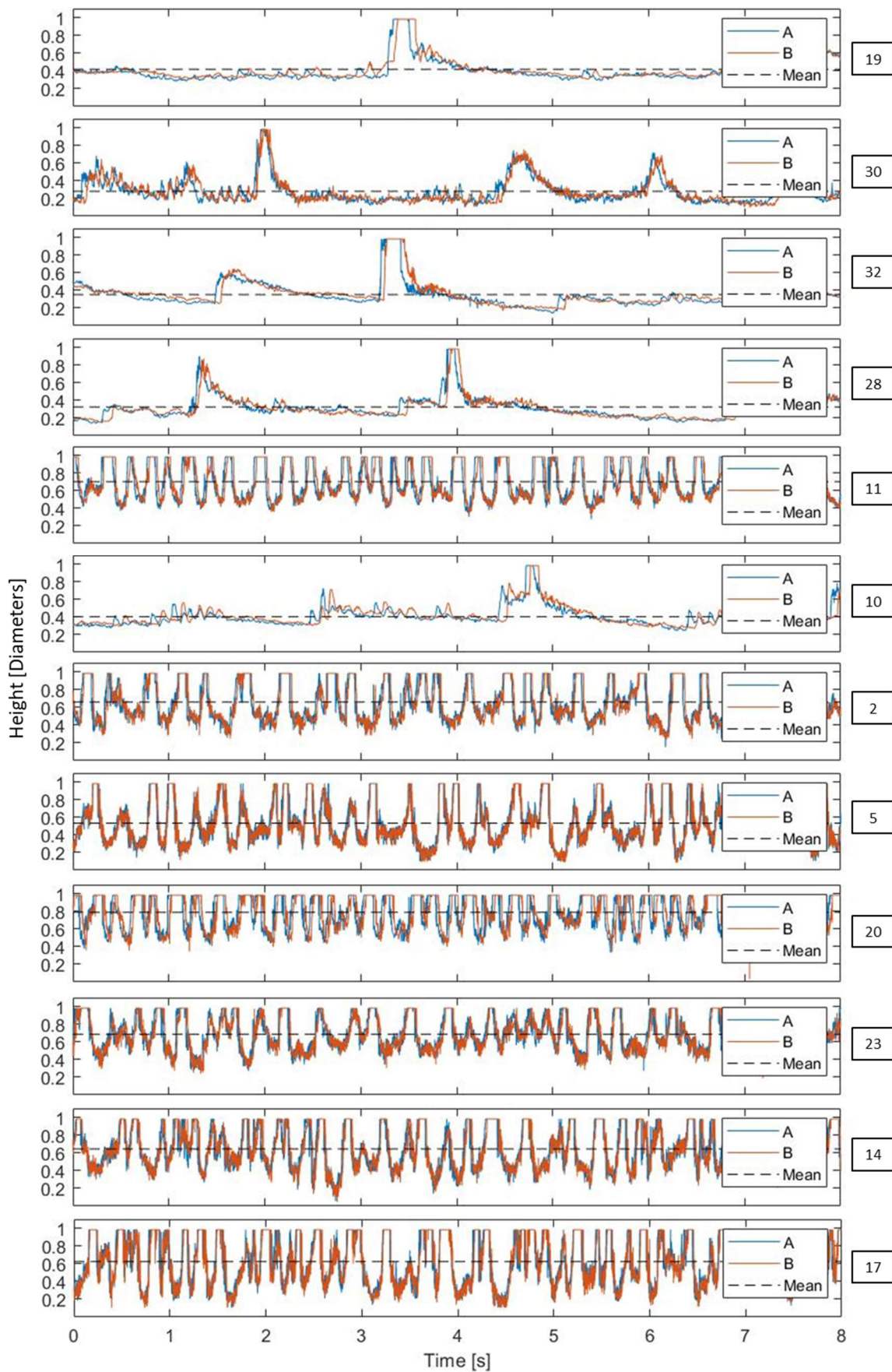


Figure 42 – Comparison of measured liquid height respectively by ROI A (red) and B (blue) at a distance of $2D$.

FFT and PSD

Using a frequency spectrum of height over time to evaluate the occurrence of intermittency does not result in a direct method for quantifying the slug periodicity. Given the definition of a Fourier transform, it is possible to infer that the frequency domain represents which periodical waves (with respective amplitude $Y(f)$ and frequency f) can be added to compose the final signal. Consequently, the resulted single-sided spectrum of h_i can be considered analogous to a sum of characteristics of the present flow pattern, including phases velocity, averaged liquid height, interfacial waves, slug amplitude and frequency. Furthermore, it is expected that dominant structures (such as a slug passage) represent the highest amplitudes structures while interfacial waves correspond to smallest ones. In this way, Figure 44 shows the frequency spectrum of relevant experimental points defined in Table 12.

In order to analyze the frequency spectrum, Olbrich et al. (2018) selected five highest amplitude events of the FFT output as a form quantified comparison between a real two-phase flow and CFD results. Therefore, for the present work this method is used to characterize the windows of dominant frequencies of the flow and it can be observed in Table 13.

In this way, it could be realized that the most remarkable characteristic observed seems to be directly related to the slug periodicity evaluating experimental points 19, 30, 32, 28 and 10 and comparing with the height over time in Figure 41. All mentioned points consist of 1 to 3 slug passages during a time of 8 seconds, meaning that this event's frequency is between 0.125 and 0.375 Hz. In terms of the frequency spectrum for these experiments, it can be noticed that highest amplitude waves (0.004 to 0.0065 m) have an occurrence between 0 and 0.5 Hz. On the other hand, highly intermittent flows (11, 2, 5, 20, 23, 14 and 17) with slug frequency from 3.125 to 4.875 Hz are represented by amplitudes ranging from 0.003 to 0.0055 m between 1.25 and 6.125 Hz. As a result, the frequency window of highest amplitude events seems to be correlated with the occurrence of slugs.

Additionally, considering only experimental points, in which the classification is given as intermittent, it is observed that the measured void fraction α_{Gh} can be related to the maximum amplitude achieved using Fourier transform. In this way, when $\alpha_{Gh} < 0.28$, $Y(f)$ does not exceed 0.004 m while for $\alpha_{Gh} > 0.32$, all experimental points has at least one value equal or superior to $Y(f) = 0.004$ m and it tops 0.0065 m. As a result, it indicates that the actual averaged void fraction may be directly related to the slug amplitude.

These evaluations indicate that there are intrinsic characteristics that can be correlated to the flow in terms of the amplitude spectrum. It could be observed that the higher the frequency of elevated amplitude events, the more a slug passage is observed over time. Therefore, flow patterns corresponds to highest amplitudes at the frequency spectrum in the same way as slug occurrences – stratified wavy is dominant at 0 to 0.5 Hz while intermittent appears to be defined at 1.25 to 6.125 Hz.

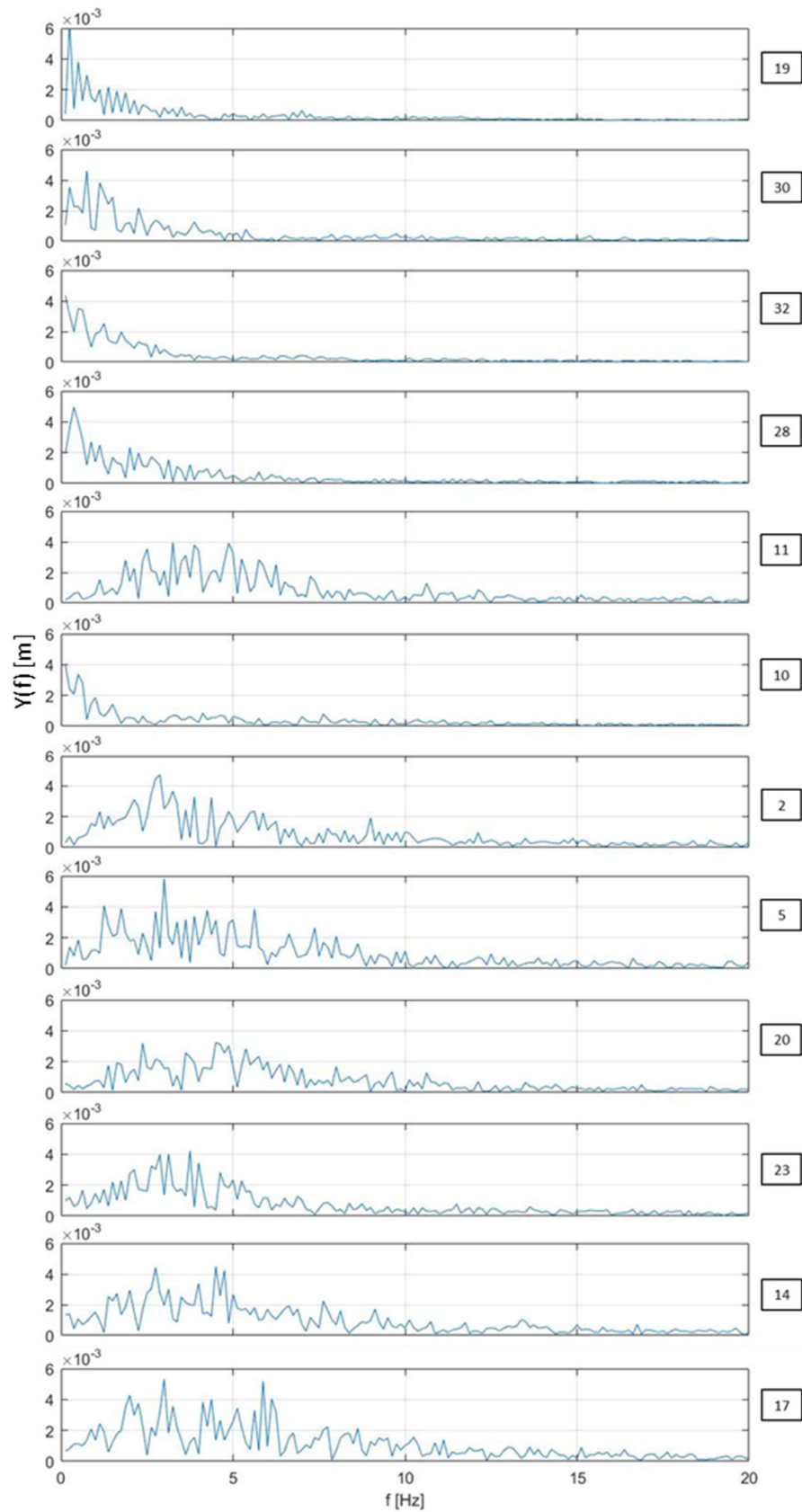


Figure 44 – Single-sided amplitude spectrum of h_i using FFT tool on MATLAB (2019). Higher amplitude events located at lower frequencies in experimental points 19, 30, 32, 28 and 10 in agreement with lower number of slug passages.

Table 13 – Frequency in which largest amplitude waves occur by *FFT*.

Experimental point	f [Hz]	Amplitude [m] * 10^{-3}
19	0.25	6.5
	0.5	3.8
	0.75	2.9
	1.375	2.2
	1.125	2.0
30	0.75	4.6
	1.125	3.8
	0.25	3.5
	1.25	3.1
	1.5	2.9
32	0.125	4.4
	0.5	3.5
	0.625	3.4
	0.25	3.1
	1.25	2.5
28	0.375	4.9
	0.5	4.0
	0.25	3.6
	0.625	2.8
	0.875	2.7
11	3.25	4.0
	4.875	3.9
	3.875	3.8
	2.5	3.5
	4	3.4
10	0.125	4.0
	0.5	3.4
	0.625	2.8
	0.25	2.4
	0.375	2.1
2	2.875	4.7
	2.75	4.5
	3.25	3.7
	2.625	3.5
	3.875	3.3
5	3	5.8
	1.25	4.1
	1.75	3.9
	5.625	3.9
	4.25	3.8
20	4.5	3.2
	2.375	3.2
	4.625	3.1
	4.875	3.0
	5.375	2.8
23	3.75	4.2
	3.125	4.0
	2.875	4.0
	4	3.4
	2.625	3.2
14	4.5	4.5
	2.75	4.4
	4.75	4.2
	4	3.4
	2.625	3.0
17	3	5.3
	5.875	5.2
	2	4.3
	6.125	4.0
	4.375	4.0

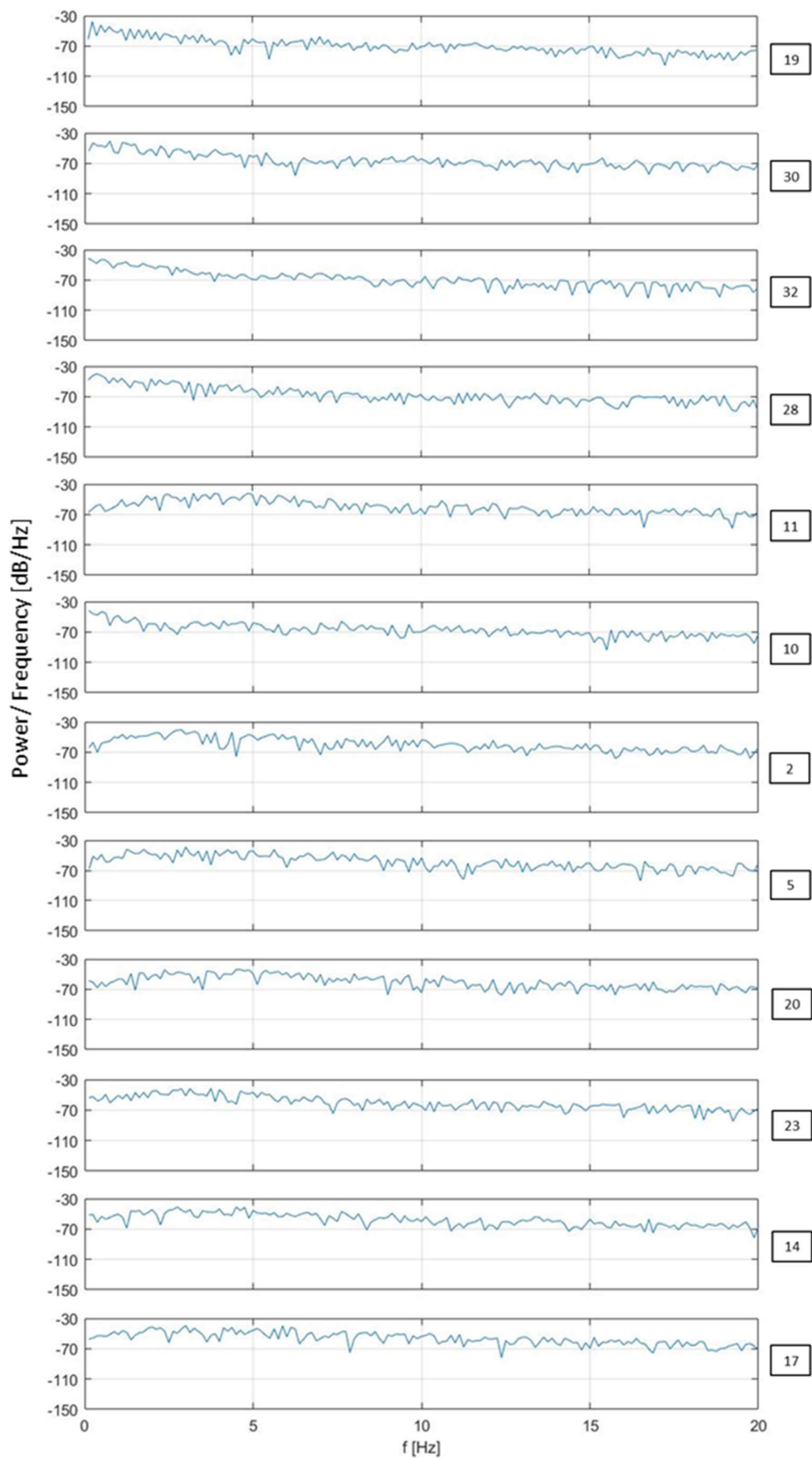


Figure 45 – Power spectral density PSD of h_i processed on MATLAB (2019) using single-sided amplitude spectrum.

In a complementary way, the power spectral density of the height over time may give additional information on the characteristics of each flow pattern. The response of this evaluation seems to be particularly in agreement with the one performed by the single-sided amplitude spectrum of h_i . However, in the PSD graph, squared power amplitude is normalized by frequency resolution. As a result, it is independent of the acquisition rate and may be a consistent form of comparing experimental points' characteristic frequencies by its correspondent spectral signature. As follows, after analyzing Figure 45 it can be observed that for stratified wavy dominant flow patterns, the peaks are also located at frequencies lower than 0.5 Hz. On the other hand, the intermittent ones show their peaks located between 1.25 and 6.125 Hz. Thereafter, for this case it can also be noticed that the higher the amplitude in Figure 44 the more curved PSD tends to result. Besides, when the maximum amplitudes are lower than 0.004 m, PSD behavior is approximately a straight line.

Lastly, if compared to FFT results, it is possible to notice that PSD plots does not add any substantial information or tool to analyze the frequency spectrum of the present work and its developments. However, it was found out that given the normalization process and independence from the acquisition rate (since it has the minimum required) this tool may be consistently useful as a training resource for machine learning algorithms, data-driven techniques, and additional validation parameter for two-phase flow CFD simulations.

Remaining experimental points

Since this analysis was conducted based on the relative accuracy of the algorithm in terms of matching the gas velocities from the geometrical and frequency shift approaches, 27 of 39 experimental points were not here evaluated. To provide an overview for who is interested, those results are available from Appendix 2 to Appendix 5.

Briefly, experimental points in which the stratified wavy flow pattern are well defined (1, 4, 7, 13, 16, 22, 25, 34, 36 and 38), the geometrical approach from the image processing algorithm is supposed to properly work and correctly estimate void fraction and gas velocity. Nonetheless, there are no passage of water columns, and the frequency shift method output does not measure the gas velocity based on a premeditated physical aspect. As a result, there is no reference to evaluate the code's performance.

The rest of the experimental points presented large disagreement between gas velocities resulting in an elevated value of relative error E_{VES} (>100%). Particularly, experimental points consisting of a high liquid level (3, 6, 9, 12, 15, 18, 21, 24, 27, 29, 31, 33, 35, 37 and 39) could not be correctly evaluated because of low contrast captured on the videos and the passage of bubbles are indeed not properly accounted for. On the other hand, experiments 8 and 26 are visually much the same as

intermittent points with $E_{VGS} < 100\%$ (selected for discussion) without regarding that, respectively, relative errors achieved 101.7% and 161.4%. As a result, those were interpreted as sufficiently affected by turbulence and not considered as a valid estimation.

4.8 STATISTICAL PARAMETERS EVALUATION

After evaluating flow pattern, friction loss and current developed image processing algorithm separately, a statistical analysis considering combined results is carried out to identify possible valid correlations between variables that yet could not be accounted for. Furthermore, it is expected that some of already observed trends may be reinforced by this analysis. For this purpose, a table containing results of all experimental points is presented on Appendix 1.

The first evaluation consists in the use of Pearson cross-correlation coefficient R (bounded between -1 and 1) to investigate possible linear correlation between variables. It is also important to highlight that this parameter is restricted to correlations that represent a linear behavior and do not identify non-linear correlations. Given this scenario, a possible linear correlation is observed comparing the individual influence of gas and liquid phases velocity on the measured ΔP and models' prediction of pressure drop ($\Delta P^{[X]}$ and $\Delta P^{[P]}$). The cross-correlation coefficient showed a value of $R = 0.81$ for ΔP and J_L , while $R = 0.35$ for ΔP and J_G , indicating that the liquid phase may be more influential in terms of the pressure drop. In this way, a relatively scattered data is adjusted to a fit in a linear equation, as shown in Figure 46.

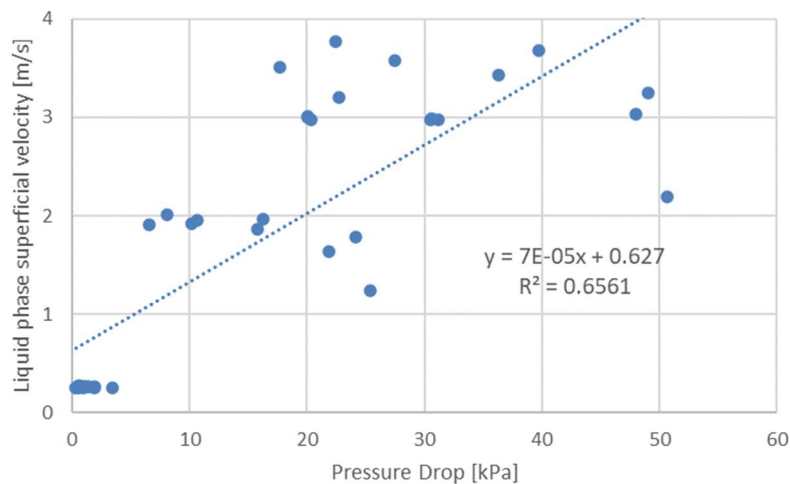


Figure 46 – Linear adjustment applied to liquid phase superficial velocity and measured pressure drop.

On the other hand, when observing data containing information of flow pattern, measured pressure drop and superficial velocity of both phases, showed in Figure 47, it is not clear in which situations the liquid phase influence may be more dominant. It is possible to observe that despite the contribution of liquid phase superficial velocity, the gas phase seems to be also influential to pressure drop measurements.

Additionally, variations in liquid phase superficial velocity appears to be more effective in increasing pressure drop measurements for flow patterns different from stratified wavy. So, it is important to account for other variables such as flow pattern, absolute pressure and localized pressure drop to be evaluated along a larger database. As a consequence, it is suggested that an individual analysis is performed for each flow pattern varying flow rates at the same absolute pressure.

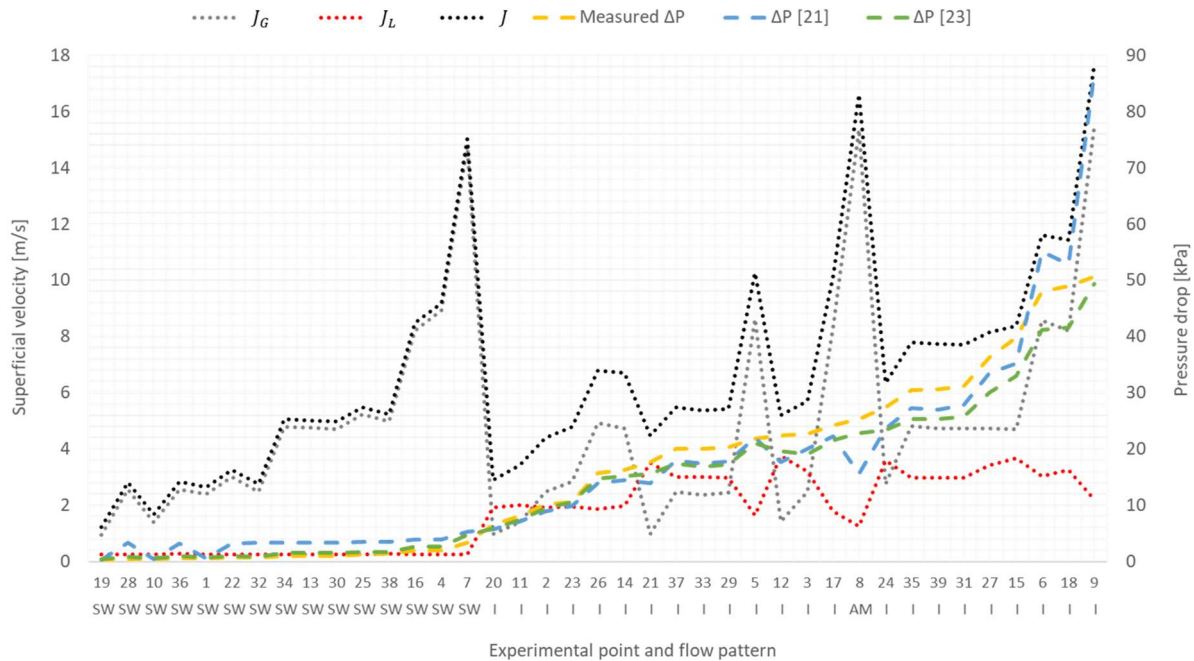


Figure 47 – Gas and liquid superficial velocities influence on pressure drop and flow pattern.

Moreover, another possible correlation relies on the slug frequency f_{slug} and pressure drop shown in Figure 48, consisting of $R = 0.75$. It is expected that when comparing the stratified flow pattern with intermittent, the first would represent lower pressure drop (Figure 47) because of the physical distribution of phases inside the pipe and due to the lower velocity of phases. On the other hand, considering only intermittent flows frequency, it is possible that it may represent a correlation with pressure drop. However, those phenomena relies on complex fluid dynamics processes and requires experiments planned to explore this occurrence. Since intermittent flow patterns observed in the present work occurred in three different absolute pressure configurations and diverse flow rates, the real influence of the slug frequency to friction loss is not clear. Variations in gas phase density and both gas and liquid phases flow rates may increase or decrease the measured pressure drop. In this way, is it proposed that a further investigation of this relation is performed using more experiments of intermittent flow patterns only, at the same absolute pressure.

Additionally, it is important to combine this analysis to the influence of individual phases to pressure drop. For example, if gas phase is considered to have low influence in pressure drop measurements, gas flow rate can be increased or decreased in order to modify slug frequency, while maintaining liquid flow rate constant. As a result, the

change in flow regime seems to impact other measured variables. For the annular regime, there is only one occurrence, and it is considered not representative for evaluation. Additionally, PC₂, PC₃ and PC₄ did not indicate any other relations.

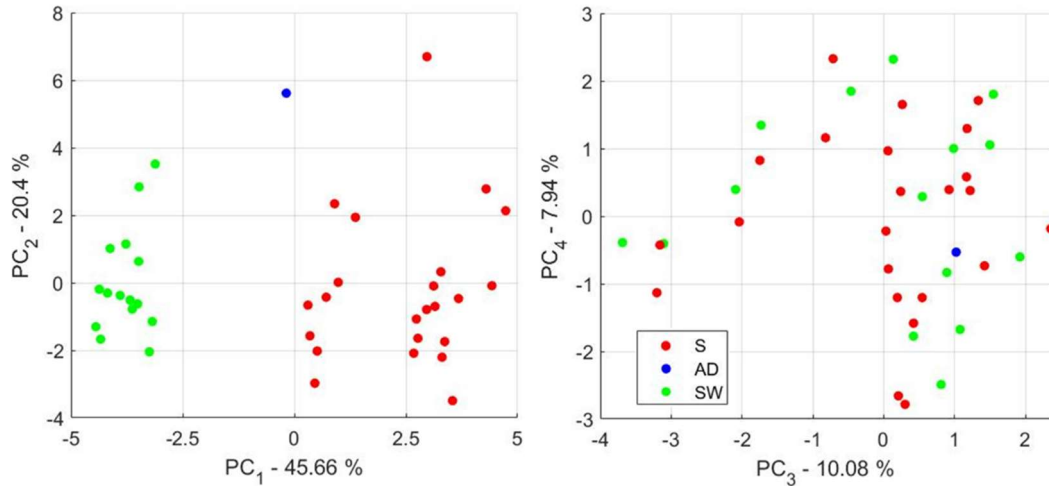


Figure 49 – PCA analysis in terms of observed flow pattern classification and its influence on data variance mostly indicated by PC₁ (S and SW) and PC₂ (AD).

Secondly, the same evaluation is performed considering ranges of measured pressure drop, consisting in a weight coefficient of 0.2869 for relative weight in PC₁. It can be observed in Figure 50 that this segmentation method also represents clusters divided into three categories, indicating that this parameter reflects certain variance of data for PC₁. Moreover, comparing analysis showed in Figure 49 and Figure 50 it can be inferred that low pressure drop measurements are correlated to stratified wavy flow patterns, while high pressure drop relates to slug or annular regimes.

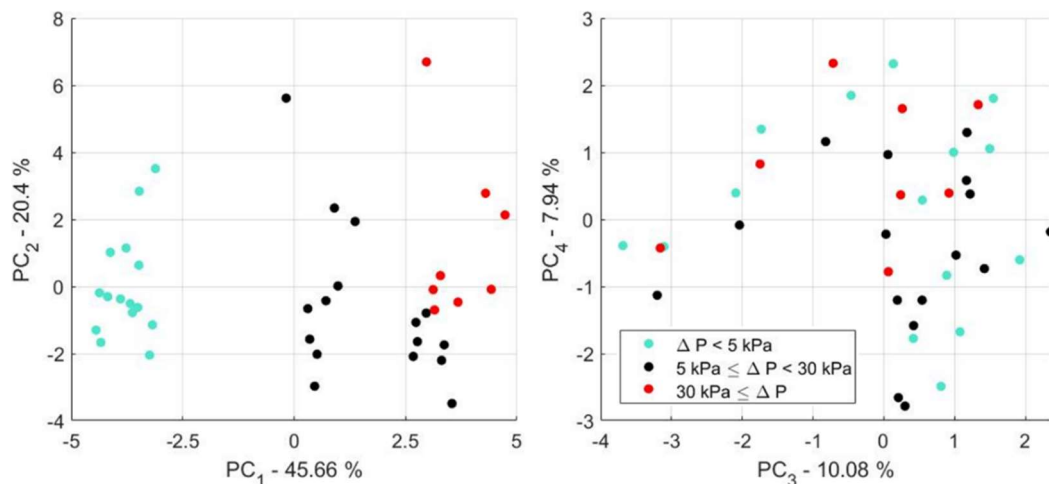


Figure 50 - PCA analysis in terms of ranges of measured pressure drop and its influence on data variance mostly indicated by PC₁.

Furthermore, the slug frequency is also used as a segmentation parameter, consisting in a weight coefficient of 0.2915 for PC₁ (which also dominate clusters positions). This evaluation may support inferences related to the influence of flow

pattern and pressure drop. It can be pointed out that cluster remarked by $f = 0$ Hz represents most of flow patterns classified as non-intermittent and consequently dominated by low measurements of pressure drop.

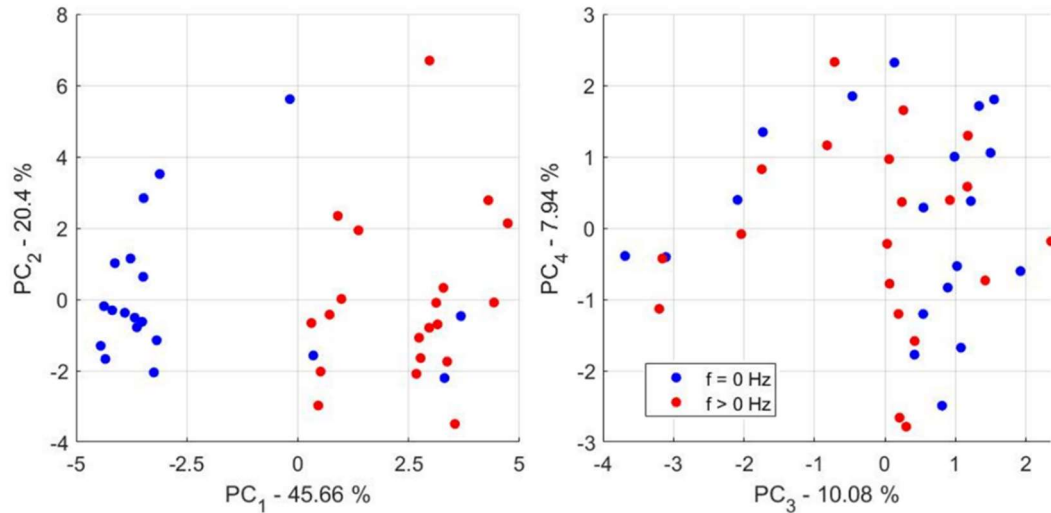


Figure 51 - PCA analysis in terms of measured slug frequency and its influence on data variance mostly indicated by PC₁.

As follows, both gas and liquid superficial velocities are adopted as a segmentation method. It can be observed in Figure 52 that liquid superficial velocity (weight coefficient of 0.3107 for PC₁) seems to be strongly correlated to measured pressure drop and flow pattern in terms of PC₁. On the other hand, gas superficial velocity clustering showed in Figure 53 is visibly most related to PC₂ (weight coefficient of 0.4356), indicating that the variance associated to this variable is orthogonal to the variance correlated to liquid superficial velocity. As a result, gas velocity may have lower influence to measured variables, but it still correlated to a certain amount of data variance.

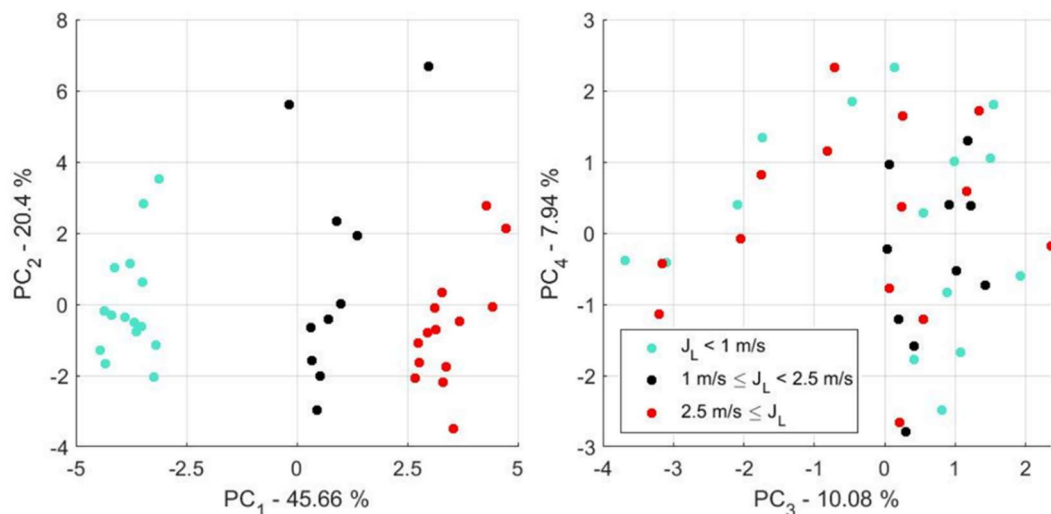


Figure 52 - PCA analysis in terms of liquid superficial velocity ranges and its influence on data variance mostly indicated by PC₁.

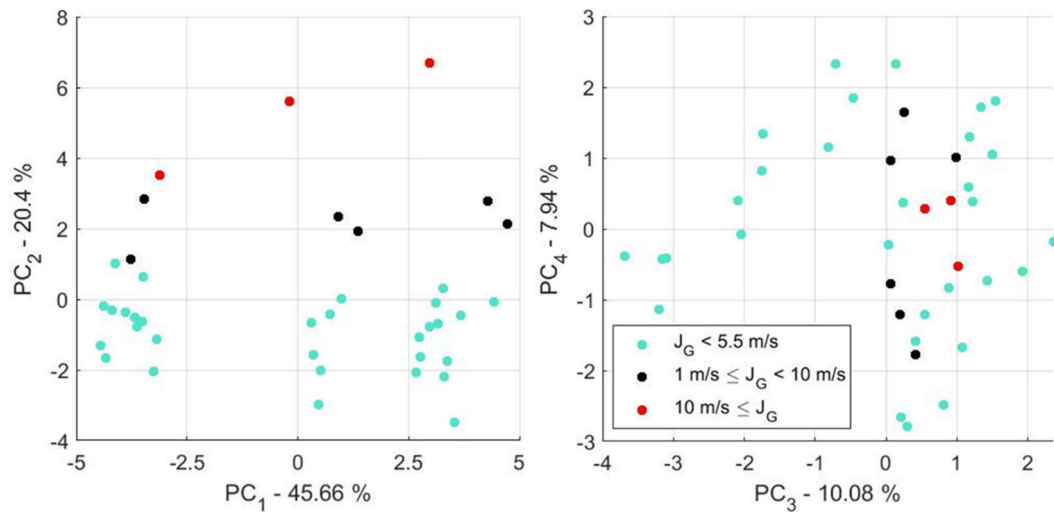


Figure 53 - PCA analysis in terms of gas superficial velocity ranges and its influence on data variance mostly indicated by PC₂.

Given accomplished statistical analysis, it is indicated that variables such as flow pattern, friction loss, slug frequency and phases superficial velocities are strongly correlated to variance in measured and calculated data. This evaluation reinforces the importance to correctly determine flow pattern for pressure drop predictions and mechanistic models' development, since measured values are associated to changes in flow regimes. Furthermore, both liquid and gas superficial velocities appeared to influence differently data variance, indicating that this is a possible study to be deepened using proper methods. Lastly, slug frequency also demonstrated to be correlated to pressure drop measurements, pointing to the possibility of carrying out a study under controlled conditions for intermittent flow patterns.

5 CONCLUSION

5.1 FINAL CONSIDERATIONS

Modeling and managing two-phase flows have demonstrated that it is still a conceptual and technological challenge. Many authors proposed methods to predict and measure properties of the flow, however many of these relies on empirical results and correlations that are not completely based on physical principles.

Given this scenario, three mechanistic models used in two-phase flows were selected by their best fitting in the present work context, based on a literature review. Additionally, those were tested against referred author's provided data and implementation was validated. In sequence, using these same models, NEMOG's multiphase flow circuit operational envelop was estimated and compared with experiments, resulting in a reasonable agreement. In such manner, it could be realized that despite the incomplete match, mechanistic models can be a powerful tool to

predict the order of magnitude of certain phenomena and can be adopted as a low-cost alternative in industrial sites where experiments cannot be accomplished.

Using the selected mechanistic models for operational envelop estimation, a set of experiments could be correctly planned, aiming to collect the higher amount of data with the lowest number of tests rounds. The first 27 experimental points consisted of a work to experimentally verify the real operational range of the facility. On the other hand, the last 12 experiments were performed to identify potential effects of pressure variation on flow pattern and pressure drop at the same superficial velocities, returning no conclusive data of this topic for the experimented conditions. Additionally, all experimental points were successfully submitted to high-frame rate video recording and evaluated by an image processing algorithm.

It can be synthesized that NEMOG's experimental circuit could reach absolute pressures up to 700 kPa, considering all safety concerns. Additionally, during the experiments, maximum two-phase volumetric flow rates were quantified as $Q_G = 120.48 \text{ m}^3/\text{h}$ for the air and $Q_L = 29.35 \text{ m}^3/\text{h}$ for the water, respectively, corresponding to superficial velocities $J_G = 15.47 \text{ m/s}$ and $J_L = 3.77 \text{ m/s}$. In terms of measured pressure drop, the maximum value was $\Delta P = 50.7 \text{ kPa}$ along a 4.8 m section. Lastly, visually observed flow patterns were stratified wavy (SW) and intermittent (I).

The performance of the flow pattern map models' predictions was evaluated against author's classification using video observations as a comparison parameter. It can be pointed out that the model of Taitel and Dukler (1976) predicted intermittent (I) and annular-dispersed liquid (AD) flow patterns, representing a pattern match on 24/39 (61.54%) experimental points. On the other hand, the model of Petalas and Aziz (2000) predicted stratified wavy (SW), slug (S), annular mist (AM) and froth (F), in agreement with 29/39 (74.36%) visual observations. In general, it can be considered a reasonably good agreement for both selected models, but it should be emphasized that the presence of a tool to quantify the influence of local pressure drop into flow pattern transitions may be appreciably relevant to be developed.

Relating to pressure drop predictions, it was observed that, in general, the model of Petalas and Aziz (2000) performed reasonably better in terms of the absolute relative error – absolute relative error of $E^{[P]}_{1-39} = 21.91\%$ and standard error deviation of $\sigma^{[P]}_{1-39} = 2.50 \text{ kPa}$ – compared to Xiao et al. (1990)'s model – $E^{[X]}_{1-39} = 89.77\%$ and $\sigma^{[X]}_{1-39} = 6.65 \text{ kPa}$. This realization may be a reflect of more updated references and the presence of a larger database used by Petalas and Aziz (2000). Additionally, predictions of pressure drop by the model of Xiao et al. (1990), in which the flow pattern was classified as annular-mist by the algorithm, represented the higher error and standard deviation values while the intermittent flow pattern is remarked by considerable precise predictions. This fact is discussed as a possible consequence of using a correlation to calculate fraction entrainment developed for vertical annular flows in a model that is applied to horizontal ones. Also, a constant value of interfacial friction factor is used, and it may also be a contribution mean. Lastly, for this model, the match between predicted and observed flow pattern seems to be quite relevant for

its performance. It was observed a high increase in performance for predictions in which the flow pattern matches. On the other hand, for the model of Petalas and Aziz (2000) the agreement between flow pattern did not demonstrate any relevant change in error or standard deviation values. In sum, both models can be considered to provide high quality predictions of pressure drop if the limitations in terms of calculation method associated to flow pattern is accounted.

The image processing algorithm was successfully developed and implemented, proving to be a valuable tool to collect information regarding a two-phase flow. In terms of its performance, it is important to note that the adopted recording configuration demonstrated its limitations in occasions that light could not sufficiently penetrate the fluid medium, in highly turbulent flows and in situations that there are no slug occurrence. Despite that, it can correctly identify phases' interface and measure gas velocity by two different approaches, achieving an average relative error value of $\langle E_{V_{GS}} \rangle = 39.74\%$ between gas velocity calculated by geometrical and frequency shift techniques, considering favorable points in which turbulence intensity is low and light properly reaches camera sensors. Moreover, the single-sided amplitude spectrum of height over time obtained by the FFT tool proved to be a possible useful solution to characterize the flow pattern without any intrusive meter. It is observed that the amplitude spectrum presents a peak in higher frequencies for all investigated intermittent flow patterns. Lastly, PSD resulted in quite similar results as FFT and specifically for this work, it did not add any relevant information. However, it may be a useful tool to quantify frequency characteristics of a flow if the acquisition rate is not the same for all evaluated configurations. Consequently, it represents a potential variable to be used at neural-networks and machine learning algorithms.

5.2 FUTURE PERSPECTIVES

After accomplishing the objectives of the present work, observations are made in terms of future developments to enlighten the continuity of this research. Additionally, some unexplored experimental configurations and techniques are suggested for further investigation.

Pressure influence on flow pattern map and friction loss

One of the objectives of the present work was evaluating the pressure influence on flow pattern map and pressure drop considering the same superficial velocities for experimental points. However, NEMOG's multiphase flow circuit operates from pressures ranging from 101.3 kPa to 800 kPa which represents a limiting boundary for exploring these effects. In this way, it is suggested that this comparison should be made at higher absolute pressure (> 800 kPa) in which the dynamics of the flow may be substantially affected by air density variations.

Additionally, this experimental limitation also affected the evaluation of mechanistic models' performance since it could not be taken to their limits. In this way, a future development could consider a wider range of flow rates and higher absolute pressures in order to compare pressure drop measurements, visual observations of flow patterns and predictions provided by models.

Frequency shift technique

The technique of frequency shift for gas velocity estimation is based on the delay between the passage of a slug through two regions of interest. In this way, it can be understood that this method may also result in the gas velocity in a parallel situation in which the periodicity of the slug is measured by another equipment. One raised possibility was that two pressure transducers installed at an experimental circuit may collect the pressure variation over time caused by the passage of the slug. An attempt of evaluating this effect was carried out, however, it could not be correctly performed given the limited temporal resolution of pressure transducers of 4 Hz, which needed to be at least 14 Hz for the present work (twice the highest slug frequency). As a result, it is suggested that this technique is evaluated using higher frequency pressure transducers or even two accelerometers attached to the external pipe's wall.

FFT and PSD applications

In terms of the amplitude and frequency spectrum, this work is based on the evaluation of height over time, which showed to be quite useful distinguishing stratified and intermittent flow patterns. Consequently, it can be inferred that different flow patterns may present different frequency spectrum, even the ones that cannot be collected by video observations. As a possible solution, many authors such as Li et al. (2016), Matsui (1986) and Wu et al. (2020) used the Fourier transform of pressure fluctuations as a quantifying parameter for flow pattern identification. Additionally, Zhang et al. (2020) associated the output of a pressure signal PSD with a machine learning algorithm to identify the flow regime of a two-phase flow.

In this way, it is proposed that since both FFT and PSD may be used as a signature of a specific flow pattern and it can be correctly categorized, it is a potential method to be developed to a less intrusive (pressure transducers) or completely non-intrusive (accelerometer or high frame rate videos) real-time flow pattern identification mechanism. This implication may directly impact on the use of mechanistic models that predicts pressure drop on-site relying on the flow pattern identification.

6 REFERENCES

ABDUL-MAJEED, G. H.; AL-MASHAT, A. M. A Mechanistic Model for Vertical and Inclined Two-Phase Slug Flow. **Dr. Sci., The University of Baghdad, Iraq**, 2000.

ANSARI, A. M. et al. Comprehensive mechanistic model for upward two-phase flow in wellbores. **SPE Production and Facilities**, v. 9, n. 2, p. 143–152, 1994.

ASSOCIAÇÃO BRASILEIRA DE NORMAS TÉCNICAS. **ABNT NBR ISO 17025: Requisitos Gerais para competência de laboratórios de ensaio e calibração**. Rio de Janeiro: [s.n.].

BANAFI, A.; TALAIE, M. R. A New Mechanistic Model to Predict Gas–Liquid Interface Shape of Gas–Liquid Flow Through Pipes with Low Liquid Loading. **AIChE Journal**, v. 59, n. 4, p. 215–228, 2012.

BARNEA, D. et al. Gas-liquid flow in inclined tubes: Flow pattern transitions for upward flow. **Chemical Engineering Science**, v. 40, n. 1, p. 131–136, 1985.

BARNEA, D. A unified model for predicting flow-pattern transitions for the whole range of pipe inclinations. **International Journal of Multiphase Flow**, v. 13, n. 1, p. 1–12, 1987.

BARNEA, D.; SHOHAM, O.; TAITEL, Y. Flow pattern transition for vertical downward two phase flow. **Chemical Engineering Science**, v. 37, n. 5, p. 741–744, 1982.

BEGGS, H. D.; BRILL, J. R. **Study of Two-Phase Flow in Inclined Pipes**. **JPT, Journal of Petroleum Technology**, 1973.

CALIMAN, R. F.; RAMOS, R. WET GAS METERING BY DIFFERENTIAL PRESSURE METERS : A LITERATURE REVIEW. In: MARTINS, M. F.; RAMOS, R.; BELICH, H. (Eds.). **Multiphase Flow Dynamics - A Perspective from the Brazilian Academy and Industry**. 1. ed. [s.l.] Springer Nature Switzerland, 2022.

CICCHITTI, A.; LOMBARDI, C.; SILVESTRI, M. Two-phase cooling experiments - Pressure drop, heat transfer and burnout measurement. **Energia Nuclear**, p. 407–425, 1960.

DA SILVA, M. J.; SCHLEICHER, E.; HAMPEL, U. Capacitance wire-mesh sensor for fast measurement of phase fraction distributions. **Measurement Science and Technology**, v. 18, n. 7, p. 2245–2251, 2007.

DINARYANTO, O. et al. Image processing analysis on the air-water slug two-phase flow in a horizontal pipe. **AIP Conference Proceedings**, v. 1737, 2016.

DO AMARAL, C. E. F. et al. Image processing techniques for high-speed videometry in horizontal two-phase slug flows. **Flow Measurement and Instrumentation**, v. 33, p. 257–264, 2013.

DUKLER, A. E.; WICKS, M.; CLEVELAND, R. G. Pressure drop and hold-up in two-phase flow. **AIChE Journal**, p. 38–51, 1964a.

DUKLER, A. E.; WICKS, M.; CLEVELAND, R. G. Frictional Pressure Drop in Two-Phase Flow: A. A Comparison of Existing Correlations for Pressure Loss and Holdup. 1964b.

EINSTEIN, A. Eine neue Bestimmung der Moleküldimensionen. **Annalen der Physik**, v. 324, n. 2, p. 289–306, 1906.

FOX, R. W. et al. **Introdução à Mecânica dos Fluidos**. 8. ed. [s.l.] LTC, 2014.

HAIDER, G. et al. A mechanistic model for stochastic rebound of solid particles with application to erosion predictions. **Wear**, v. 376–377, p. 615–624, 2017.

HERNANDEZ, J. S. et al. Data driven methodology for model selection in flow pattern prediction. **Heliyon**, v. 5, n. 11, p. e02718, 2019.

HEWITT, G. F.; HALL-TAYLOR, N. S. **Annular two-phase flow**. New York: Pergamon Press, 1970.

HOOGENDORD, C. J. Flow in Horizontal Pipes. **Chemical Engineering Science**, v. 9, p. 205–217, 1959.

HUANG, C.-N.; KHARANGATE, C. R. A new mechanistic model for predicting flow boiling critical heat flux based on hydrodynamic instabilities. **International Journal of Heat and Mass Transfer**, v. 138, p. 1295–1309, 2019.

HUGHMARK, G. A.; PRESSBURG, B. S. Holdup and pressure drop with gas-liquid flow in a vertical pipe. **A.I.Ch.E. Journal**, v. 7, n. 4, p. 677–682, 1961.

ISHII, M.; HIKIBI, T. **Thermo-Fluid Dynamics of Two-Phase Flow**. Second Edition. New York: Springer Science and Business Media, 2011. v. 51

JEREZ-CARRIZALES, M.; JARAMILLO, J. E.; FUENTES, D. Prediction of Multiphase Flow in Pipelines: Literature Review. **Ingeniería y Ciencia**, v. 11, n. 22, p. 213–233, 2015.

KANIN, E. A. et al. A predictive model for steady-state multiphase pipe flow: Machine learning on lab data. **Journal of Petroleum Science and Engineering**, v. 180, n. May, p. 727–746, 2019.

KRUMRICK, E.; LOPEZ, E.; CAMACHO, A. Prediction of the Flow Regime in Liquid-Gas Flows Through Straight Pipes Using Computational Fluid Dynamics. **Mecánica Computacional**, v. 34, n. 30, p. 2101–2114, 2016.

KUNTORO, H. Y. et al. Experimental Study of the Interfacial Waves in Horizontal Stratified Gas-liquid Two-phase Flows by Using the Developed Image Processing Technique. p. 85–91, 2015.

LI, X. et al. Study of gas-liquid two-phase flow patterns of self-excited dust scrubbers. **Chemical Engineering Science**, 2016.

LOCKHART, R. W.; MARTINELLI, R. C. Proposed correlation of data for isothermal two-phase, two-component flow in pipes. **Chemical Engineer Progress**, 1949.

MATLAB. **Version R2019a**Natick, MassachusettsThe MathWorks Inc, , 2019.

MATSUI, G. Automatic identification of flow regimes in vertical two-phase flow using differential pressure fluctuations. **Nuclear Engineering and Design**, v. 95, p. 221–231, 1986.

MCADAMS, W. H.; WOODS, W. H.; HEROMAN, L. C. Vaporization inside horizontal tubes. **Transactions of ASME**, v. 64, p. 193–200, 1942.

MCQUILLAN, K. W.; WHALLEY, P. B. Flow patterns in vertical two-phase flow. v. I, n. 2, p. 161–175, 1985.

MERIBOUT, M. et al. Multiphase Flow Meters Targeting Oil & Gas Industries. **Measurement: Journal of the International Measurement Confederation**, v. 165, p. 108111, 2020.

MINHONI, R. DE A. et al. The performance of explicit formulas for determining the Darcy-Weisbach friction factor. **Soil and Water Engineering**, v. 40, n. 2, 2020.

MOHMED, A. O. et al. Measurements of translational slug velocity and slug length using an image processing technique. **Flow Measurement and Instrumentation**, v. 50, p. 112–120, 2016.

MONTGOMERY, D. C. **Design and analysis of experiments**. 8. ed. Tempe: John Wiley & Sons, Inc., 2013.

MORALES, R. E. M. Image analysis of horizontal two-phase flows. **International Mechanical Engineering Congress & Exposition**, p. 1–7, 2011.

MUKHERJEE, H.; BRILL, J. P. Pressure drop correlations for inclined two-phase flow. **Journal of Energy Resources Technology, Transactions of the ASME**, v. 107, n. 4, p. 549–554, 1985.

NAC IMAGE TECHNOLOGY. **HotShot 512 sc Digital High-Speed Video Camera**. Disponível em: <https://www.nacinc.com/datasheets/HotShot_512_sc_Specification_Sheet_DEC06.pdf>. Acesso em: 23 mar. 2022.

OLBRICH, M. et al. Validation of simulations in multiphase flow metrology by comparison with experimental video observations. **Journal of Physics: Conference Series**, v. 1065, n. 9, 2018.

OLIEMANS, R. V. A.; POTS, B. F. M.; TROMPÉ, N. Modelling of annular dispersed two-phase flow in vertical pipes. **International Journal of Multiphase Flow**, v. 12, n. 5, p. 711–732, 1986.

PAYNE, G. A. et al. Evaluation of Inclined-Pipe, Two-Phase Liquid Holdup and Pressure-Loss Correlations Using Experimental Data. **JPT, Journal of Petroleum Technology**, v. 31, n. 9, p. 1198–1208, 1979.

PETALAS, N.; AZIZ, K. **Stanford Multiphase Flow Database - Users Manual, Version 0.2** Petroleum Engineering Dept., Stanford University, , 1995.

PETALAS, N.; AZIZ, K. A mechanistic model for multiphase flow in pipes. **Annual Technical Meeting 1998, ATM 1998**, 2000.

ROUHANI, S. Z.; SOHAL, M. S. Two-phase flow patterns: A review of research results. **Progress in Nuclear Energy**, v. 11, n. 3, p. 219–259, 1983.

SCHMELTER, S. et al. Numerical simulation, validation, and analysis of two-phase slug flow in large horizontal pipes. **Flow Measurement and Instrumentation**, v. 73, 2020.

SHABAN, H.; TAVOULARIS, S. Performance evaluation of conductivity wire-mesh sensors in vertical channels. **Flow Measurement and Instrumentation**, v. 54, n. February, p. 185–196, 2017.

SHAHVERDI, H.; SOHRABI, M. A mechanistic model for prediction of three-phase flow in petroleum reservoirs. **Journal of Petroleum Science and Engineering**, v. 157, p. 507–518, 2017.

SHUARD, A. M.; MAHMUD, H. B.; KING, A. J. Comparison of two-phase pipe flow in openFOAM with a mechanistic model. **IOP Conference Series: Materials Science and Engineering**, v. 121, n. 1, 2016.

TAITEL, Y.; BARNEA, D. **Encyclopedia of Two-Phase Heat Transfer and Flow I**. 1. ed. Lausanne: World Scientific Publishing Co. Pte. Ltd., 2015.

TAITEL, Y.; BORNEA, D.; DUKLER, A. E. Modelling flow pattern transitions for steady upward gas-liquid flow in vertical tubes. **AIChE Journal**, v. 26, n. 3, p. 345–354, 1980.

TAITEL, Y.; DUKLER, A. E. A model for predicting flow regime transitions in horizontal and near horizontal gas-liquid flow. **AIChE Journal**, v. 22, n. 1, p. 47–55, 1976.

THOME, J. R. et al. Unified mechanistic multiscale mapping of two-phase flow patterns in microchannels. **Experimental Thermal and Fluid Science**, v. 44, p. 1–22, 2013.

U.S. DEPARTMENT OF COMMERCE. **National Institute of Standards and Technology**. Disponível em: <https://webbook.nist.gov/cgi/fluid.cgi?TUnit=C&PUnit=bar&DUnit=mol%2Fm³&HUnit=kJ%2Fmol&WUnit=m%2Fs&VisUnit=uPa*s&STUnit=N%2Fm²&Type=IsoTherm&RefState=DEF&Action=Page&ID=C106978>. Acesso em: 26 set. 2020.

VELASCO PEÑA, H. F.; RODRIGUEZ, O. M. H. Applications of wire-mesh sensors in multiphase flows. **Flow Measurement and Instrumentation**, v. 45, p. 255–273, 2015.

WALLIS, G. B. **One-dimensional two phase flow**. 1. ed. [s.l.] McGraw-Hill Companies, 1969.

WIDYATAMA, A. et al. The development of image processing technique to study the interfacial behavior of air-water slug two-phase flow in horizontal pipes. **Flow Measurement and Instrumentation**, v. 59, p. 168–180, 2018.

WU, B. et al. Use of pressure signal analysis to characterise counter-current two-phase flow regimes in annuli. **Chemical Engineering Research and Design**, v. 153, p. 547–561, 2020.

XIAO, J. J.; SHOHAM, O.; BRILL, J. P. Comprehensive mechanistic model for two-phase flow in pipelines. **Proceedings - SPE Annual Technical Conference and Exhibition**, v. Pi, p. 167–180, 1990.

ZHANG, F. et al. A unified transient solid-liquid two-phase flow model for cuttings transport- modelling part. **Journal of Petroleum Science and Engineering**, v. 166, n. December 2017, p. 146–156, 2018.

ZHANG, Y. et al. Two - phase flow regime identification based on the liquid - phase velocity information and machine learning. **Experiments in Fluids**, p. 1–16, 2020.

ZHOU, H.; NIU, X. An image processing algorithm for the measurement of multiphase bubbly flow using predictor-corrector method. **International Journal of Multiphase Flow**, v. 128, 2020.

7 APPENDIX

Appendix 1 – Combined results 1-39.

Experiment number/ Variables	1	2	3	4	5	6	7	8	9
M_G [kg/h]	58	60	60	218	214	211	365	371	378
M_L [kg/h]	1995	14947	24918	2023	12754	23584	2011	9638	17008
Q_G [m ³ /h]	18.6	19.3	19.4	69.5	67.2	66.7	115.0	119.6	120.5
Q_L [m ³ /h]	2.0	15.0	25.0	2.0	12.8	23.6	2.0	9.7	17.0
J_G [m/s]	2.38	2.48	2.49	8.93	8.63	8.57	14.77	15.36	15.47
J_L [m/s]	0.26	1.92	3.21	0.26	1.64	3.03	0.26	1.24	2.19
P_{ABS} [bar]	2.70	2.69	2.68	2.71	2.74	2.73	2.73	2.67	2.70
T [°K]	302.3	302.0	301.9	301.9	301.7	301.6	301.4	301.6	301.5
ρ_L [kg/m ³]	997.2	997.3	997.3	997.3	997.4	997.4	997.5	997.4	997.4
ρ_G [kg/m ³]	3.12	3.11	3.11	3.14	3.18	3.17	3.17	3.10	3.14
$\Delta P_{measured}$ [Pa]	621	10197	22716	1947	21833	48008	3393	25374	50687
ΔP [Pa] by Xiao et al. (1990)	581	8881	20100	3935	22001	55116	5323	15617	86842
E_1 [%]	-6.41%	-12.91%	-11.52%	102.06%	0.77%	14.81%	53.90%	-38.45%	71.33%
ΔP [Pa] by Petalas and Aziz (2000)	765	9482	19121	2631	20957	41116	4694	22855	49339
E_2 %	23.24%	-7.01%	-15.83%	35.11%	-4.01%	-14.36%	38.34%	-9.93%	-2.66%
$\alpha_{G ref}$	0.90	0.56	0.44	0.97	0.84	0.74	0.98	0.93	0.88
$\alpha_{G h}$	0.71	0.32	0.02	0.84	0.47	0.13	0.93	0.56	0.07
$V_{G h}$ [m/s]	3.4	7.8	148.1	10.6	18.4	63.6	15.8	27.3	206.6
$V_{L h}$ [m/s]	0.87	2.83	3.26	1.62	3.09	3.51	3.92	2.84	2.37
$\alpha_{G s}$	0.00	0.46	0.34	1.86	0.74	0.63	0.00	1.13	1.29
$V_{G s}$ [m/s]	0.00	5.43	7.41	4.80	11.64	13.58	0.00	13.58	12.04
$V_{L s}$ [m/s]	0.00	3.54	4.83	-0.30	6.34	8.22	0.00	-9.47	-7.67
$\langle f \rangle_{slug}$ [Hz]	0	3.125	6	0.125	3.375	5.875	0	2.25	4.875
$\langle h \rangle_L$	1.74E-02	3.52E-02	5.12E-02	1.04E-02	2.84E-02	4.54E-02	5.83E-03	2.44E-02	4.82E-02
E_{VGS}	3374%	43%	1899%	122%	58%	368%	15814%	101%	1616%
Fr	0.1862	0.1933	0.1938	0.6988	0.6806	0.6738	1.1628	1.1957	1.2119
Re_{SL}	16499	123650	206138	16733	105513	195120	16641	79740	140720
Re_{SG}	210514	218244	218550	791949	776865	766906	1324947	1347354	1374074

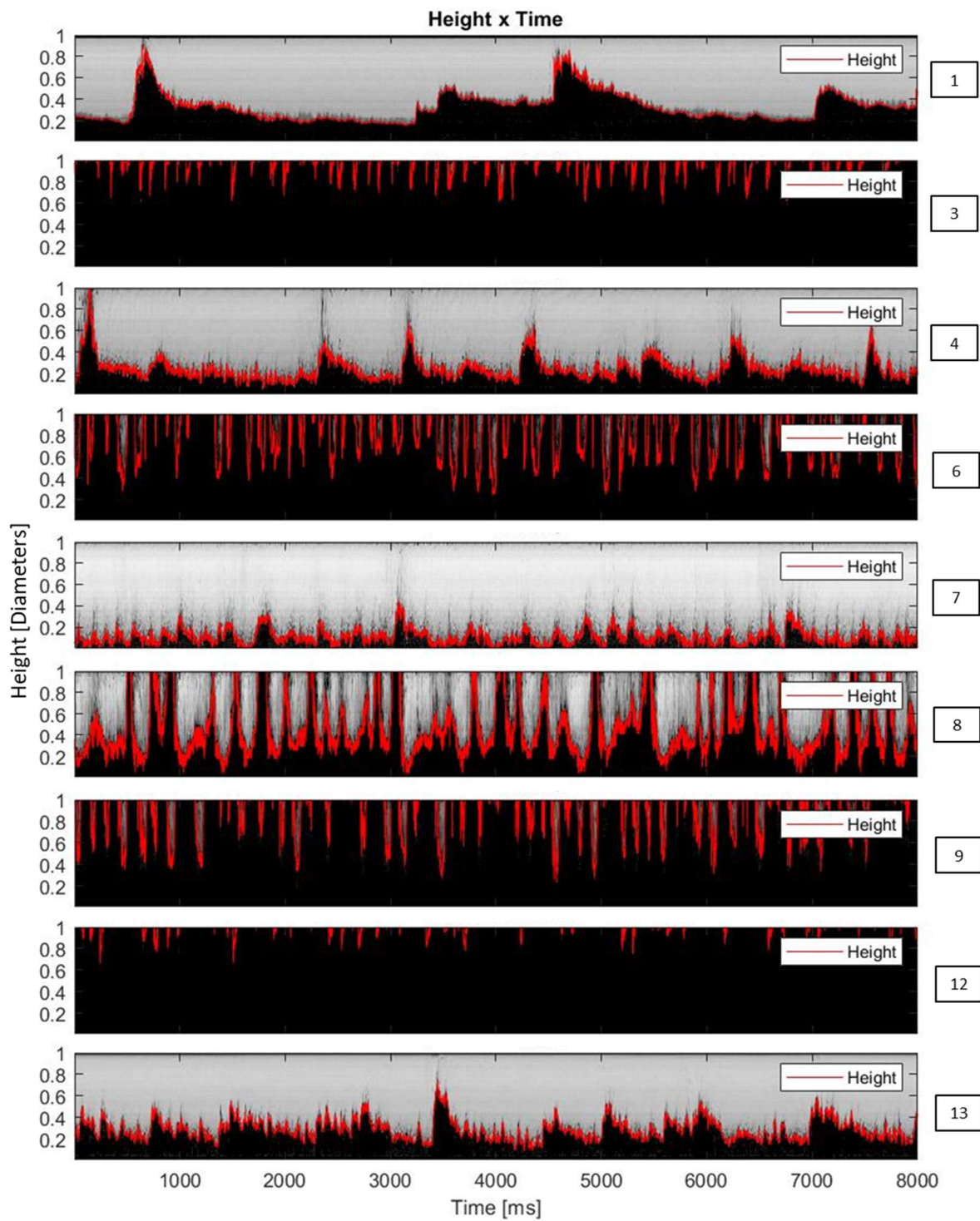
Experiment number/ Variables	10	11	12	13	14	15	16	17	18
M_G [kg/h]	61	61	63	209	208	207	360	364	360
M_L [kg/h]	2052	15672	29289	2002	15284	28558	2006	13898	25219
Q_G [m ³ /h]	10.9	10.9	11.2	37.1	36.9	36.5	64.0	65.0	63.8
Q_L [m ³ /h]	2.1	15.7	29.3	2.0	15.3	28.6	2.0	13.9	25.3
J_G [m/s]	1.40	1.40	1.43	4.76	4.73	4.69	8.21	8.35	8.19
J_L [m/s]	0.26	2.02	3.77	0.26	1.97	3.67	0.26	1.79	3.24
P_{ABS} [bar]	4.85	4.83	4.84	4.86	4.85	4.87	4.86	4.81	4.86
T [°k]	302.0	301.5	301.3	302.1	301.0	300.8	301.5	300.7	300.6
ρ_L [kg/m ³]	997.3	997.5	997.5	997.3	997.6	997.7	997.5	997.7	997.7
ρ_G [kg/m ³]	5.62	5.60	5.61	5.62	5.63	5.65	5.63	5.59	5.65
$\Delta P_{measured}$ [Pa]	485	8065	22427	1003	16304	39717	1908	24165	49018
ΔP [Pa] by Xiao et al. (1990)	384	7115	17610	3386	14496	35249	3948	22262	52851
E_1 [%]	-20.75%	-11.78%	-21.48%	237.61%	-11.09%	-11.25%	106.91%	-7.88%	7.82%
ΔP [Pa] by Petalas and Aziz (2000)	515	7419	19599	1557	15159	32955	2634	21623	41615
E_2 %	6.25%	-8.01%	-12.61%	55.20%	-7.02%	-17.03%	38.04%	-10.52%	-15.10%
$\alpha_{G ref}$	0.84	0.41	0.28	0.95	0.71	0.56	0.97	0.82	0.72
$\alpha_{G h}$	0.61	0.27	0.00	0.76	0.33	0.01	0.83	0.37	0.01
$V_{G h}$ [m/s]	2.3	5.2	349.3	6.3	14.2	601.5	9.9	22.4	577.1
$V_{L h}$ [m/s]	0.68	2.77	3.78	1.06	2.95	3.70	1.52	2.85	3.29
$\alpha_{G s}$	0.80	0.33	0.23	1.89	0.57	0.51	0.00	0.68	0.57
$V_{G s}$ [m/s]	1.74	4.21	6.30	2.52	8.23	9.17	0.00	12.34	14.42
$V_{L s}$ [m/s]	1.34	3.02	4.88	-0.29	4.63	7.52	0.00	5.54	7.52
$\langle f \rangle_{slug}$ [Hz]	0.125	4	2.875	0	4.375	4.125	0	4	4.25
$\langle h \rangle_L$	2.15E-02	3.75E-02	5.21E-02	1.51E-02	3.44E-02	5.19E-02	1.17E-02	3.33E-02	5.16E-02
E_{VGS}	32%	23%	5444%	149%	72%	6456%	9890%	82%	3903%
Fr	0.1465	0.1467	0.1501	0.4999	0.4970	0.4936	0.8627	0.8741	0.8617
Re_{SL}	16977	129669	242335	16563	126475	236328	16595	115012	208704
Re_{SG}	221804	221820	227285	757177	753621	749866	1308365	1321058	1308707

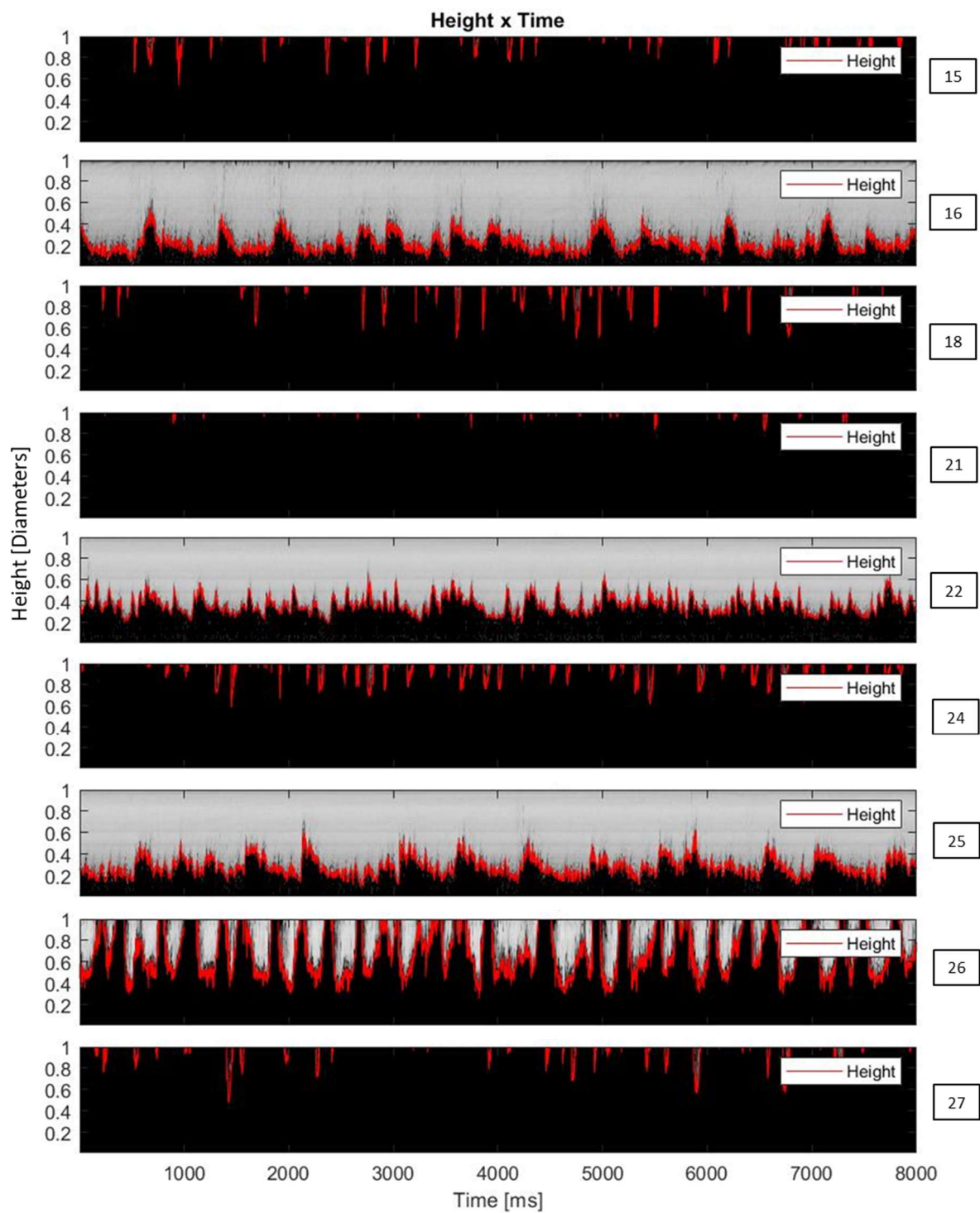
Experiment number/ Variables	19	20	21	22	23	24	25	26	27
M_G [kg/h]	60	61	61	189	179	173	330	313	300
M_L [kg/h]	2011	14844	27305	2037	15216	27825	2037	14477	26648
Q_G [m ³ /h]	7.4	7.6	7.5	23.4	22.1	21.5	40.7	38.3	36.9
Q_L [m ³ /h]	2.0	14.9	27.4	2.0	15.2	27.9	2.0	14.5	26.7
J_G [m/s]	0.96	0.97	0.97	3.00	2.83	2.76	5.23	4.92	4.74
J_L [m/s]	0.26	1.91	3.51	0.26	1.96	3.58	0.26	1.86	3.43
P_{ABS} [bar]	6.98	6.96	6.96	7.00	7.01	6.97	7.00	7.05	7.02
T [°K]	302.1	301.8	301.7	302.2	301.4	301.3	301.6	301.3	301.1
ρ_L [kg/m ³]	997.3	997.4	997.4	997.3	997.5	997.5	997.4	997.5	997.6
ρ_G [kg/m ³]	8.07	8.05	8.05	8.08	8.12	8.08	8.10	8.17	8.13
$\Delta P_{measured}$ [Pa]	344	6543	17723	672	10634	27422	1288	15780	36262
ΔP [Pa] by Xiao et al. (1990)	279	5667	13952	3272	9840	23618	3489	13883	33536
E_1 [%]	-18.79%	-13.39%	-21.28%	387.25%	-7.47%	-13.87%	170.93%	-12.02%	-7.52%
ΔP [Pa] by Petalas and Aziz (2000)	384	5870	15623	1028	10562	23427	1722	14768	30102
E_2 %	11.55%	-10.30%	-11.85%	53.12%	-0.68%	-14.57%	33.66%	-6.41%	-16.99%
$\alpha_{G ref}$	0.79	0.34	0.22	0.92	0.59	0.43	0.95	0.73	0.58
$\alpha_{G h}$	0.59	0.17	0.00	0.67	0.28	0.01	0.77	0.28	0.01
$V_{G h}$ [m/s]	1.6	5.6	1473.3	4.5	10.0	186.2	6.8	17.4	419.1
$V_{L h}$ [m/s]	0.63	2.31	3.52	0.80	2.73	3.63	1.12	2.60	3.47
$\alpha_{G s}$	0.59	0.28	0.17	0.00	0.48	0.39	0.00	0.74	0.57
$V_{G s}$ [m/s]	1.61	3.44	5.55	0.00	5.96	7.14	0.00	6.66	8.33
$V_{L s}$ [m/s]	0.63	2.67	4.26	0.00	3.74	5.83	0.00	7.11	7.95
$\langle f \rangle_{slug}$ [Hz]	0.125	4.875	4	0	2.875	3.875	0	3.375	2.5
$\langle h \rangle_L$	2.24E-02	4.21E-02	5.24E-02	1.89E-02	3.67E-02	5.14E-02	1.48E-02	3.67E-02	5.18E-02
E_{VGS}	1%	63%	26429%	4471%	68%	2508%	6826%	161%	4932%
Fr	0.1202	0.1225	0.1219	0.3783	0.3578	0.3471	0.6592	0.6230	0.5985
Re_{SL}	16631	122806	225905	16852	125893	230226	16851	119786	220504
Re_{SG}	217962	221732	220670	686274	650596	629463	1197458	1136705	1089356

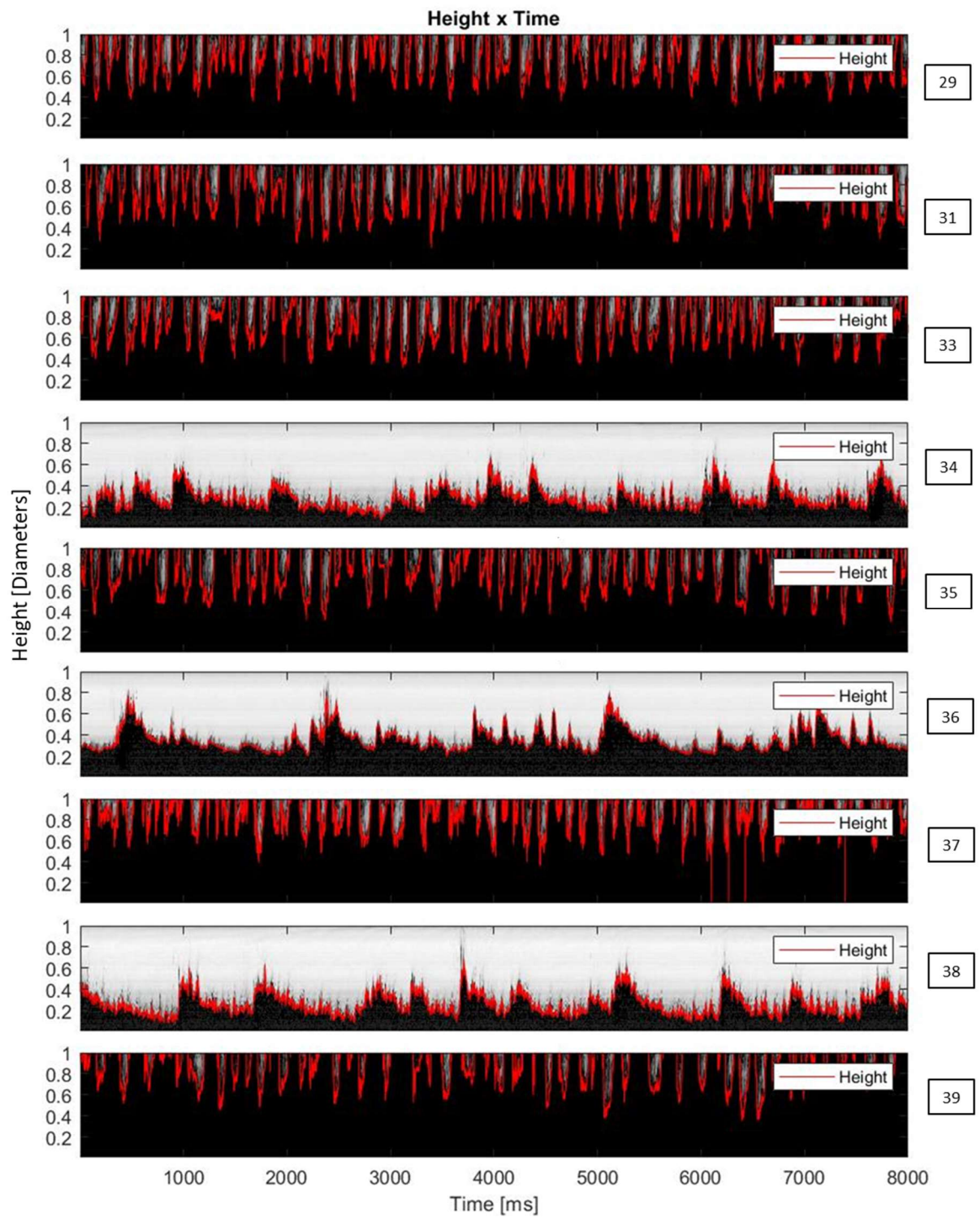
Experiment number/ Variables	28	29	30	31	32	33
M_G [kg/h]	63	61	117	118	109	105
M_L [kg/h]	2048	23107	2057	23158	2043	23267
Q_G [m ³ /h]	19.8	19.2	36.7	36.8	19.3	18.5
Q_L [m ³ /h]	2.1	23.2	2.1	23.2	2.0	23.3
J_G [m/s]	2.55	2.46	4.71	4.73	2.48	2.38
J_L [m/s]	0.26	2.97	0.26	2.98	0.26	2.99
P_{ABS} [bar]	2.71	2.73	2.72	2.74	4.81	4.84
T [°K]	299.3	298.8	299.1	298.7	299.6	299.2
ρ_L [kg/m ³]	998.1	998.2	998.1	998.2	998.0	998.1
ρ_G [kg/m ³]	3.17	3.20	3.19	3.21	5.61	5.66
$\Delta P_{measured}$ [Pa]	485	20376	1033	31132	681	20028
ΔP [Pa] by Xiao et al. (1990)	3306	17779	3372	27827	3281	17426
E_1 [%]	582.26%	-12.75%	226.46%	-10.62%	382.10%	-12.99%
ΔP [Pa] by Petalas and Aziz (2000)	842	17212	1531	25701	832	16872
E_2 %	73.77%	-15.53%	48.25%	-17.44%	22.28%	-15.76%
$\alpha_{G ref}$	0.91	0.45	0.95	0.61	0.90	0.44
$\alpha_{G h}$	0.72	0.17	0.75	0.18	0.67	0.18
$V_{G h}$ [m/s]	3.5	14.7	6.2	26.2	3.7	13.4
$V_{L h}$ [m/s]	0.96	3.57	1.07	3.63	0.80	3.64
$\alpha_{G s}$	0.83	0.39	0.82	0.50	0.75	0.41
$V_{G s}$ [m/s]	3.05	6.36	5.72	9.54	3.32	5.87
$V_{L s}$ [m/s]	1.60	4.85	1.50	5.91	1.04	5.03
$\langle f \rangle_{slug}$ [Hz]	0.25	5.75	0.125	5.25	0.125	6.375
$\langle h \rangle_L$	1.74E-02	4.29E-02	1.50E-02	4.25E-02	1.88E-02	4.70E-02
E_{Ves}	15%	132%	9%	175%	11%	128%
Fr	0.2006	0.1943	0.3716	0.3745	0.2603	0.2502
Re_{SL}	16956	191320	17027	191747	16909	192620
Re_{SG}	228538	222408	424614	429505	394123	380355

Experiment number/ Variables	34	35	36	37	38	39
M_G [kg/h]	211	212	163	158	314	302
M_L [kg/h]	2042	23131	2111	23407	2085	23230
Q_G [m ³ /h]	37.4	37.4	20.0	19.3	38.7	36.9
Q_L [m ³ /h]	2.0	23.2	2.1	23.5	2.1	23.3
J_G [m/s]	4.80	4.81	2.57	2.47	4.97	4.74
J_L [m/s]	0.26	2.98	0.27	3.01	0.27	2.99
P_{ABS} [bar]	4.84	4.85	7.01	7.04	6.98	7.03
T [°K]	299.6	299.3	300.5	299.6	300.2	299.5
ρ_L [kg/m ³]	998.0	998.0	997.7	998.0	997.8	998.0
ρ_G [kg/m ³]	5.65	5.66	8.15	8.20	8.12	8.19
$\Delta P_{measured}$ [Pa]	950	30470	604	20024	1460	30587
ΔP [Pa] by Xiao et al. (1990)	3399	27232	3276	17978	3464	27050
E_1 [%]	257.59%	-10.63%	442.25%	-10.22%	137.32%	-11.56%
ΔP [Pa] by Petalas and Aziz (2000)	1599	25353	923	17387	1660	25272
E_2 %	68.22%	-16.79%	52.82%	-13.17%	13.74%	-17.38%
$\alpha_{G\ ref}$	0.95	0.62	0.90	0.45	0.95	0.61
$\alpha_{G\ h}$	0.76	0.15	0.68	0.15	0.79	0.09
$V_{G\ h}$ [m/s]	6.3	32.0	3.8	16.9	6.3	54.9
$V_{L\ h}$ [m/s]	1.08	3.50	0.84	3.53	1.25	3.27
$\alpha_{G\ s}$	0.00	0.57	0.00	0.39	0.00	0.59
$V_{G\ s}$ [m/s]	0.00	8.48	0.00	6.36	0.00	8.10
$V_{L\ s}$ [m/s]	0.00	6.87	0.00	4.93	0.00	9.54
$\langle f \rangle_{slug}$ [Hz]	0	4.75	0	5.75	0	4
$\langle h \rangle_L$	1.50E-02	4.40E-02	1.89E-02	4.37E-02	1.37E-02	4.74E-02
E_{Ves}	6346%	277%	3805%	165%	6324%	578%
Fr	0.5044	0.5059	0.3251	0.3136	0.6273	0.6011
Re_{SL}	16900	191494	17474	193762	17257	192300
Re_{SG}	765932	769521	592232	573188	1140863	1098269

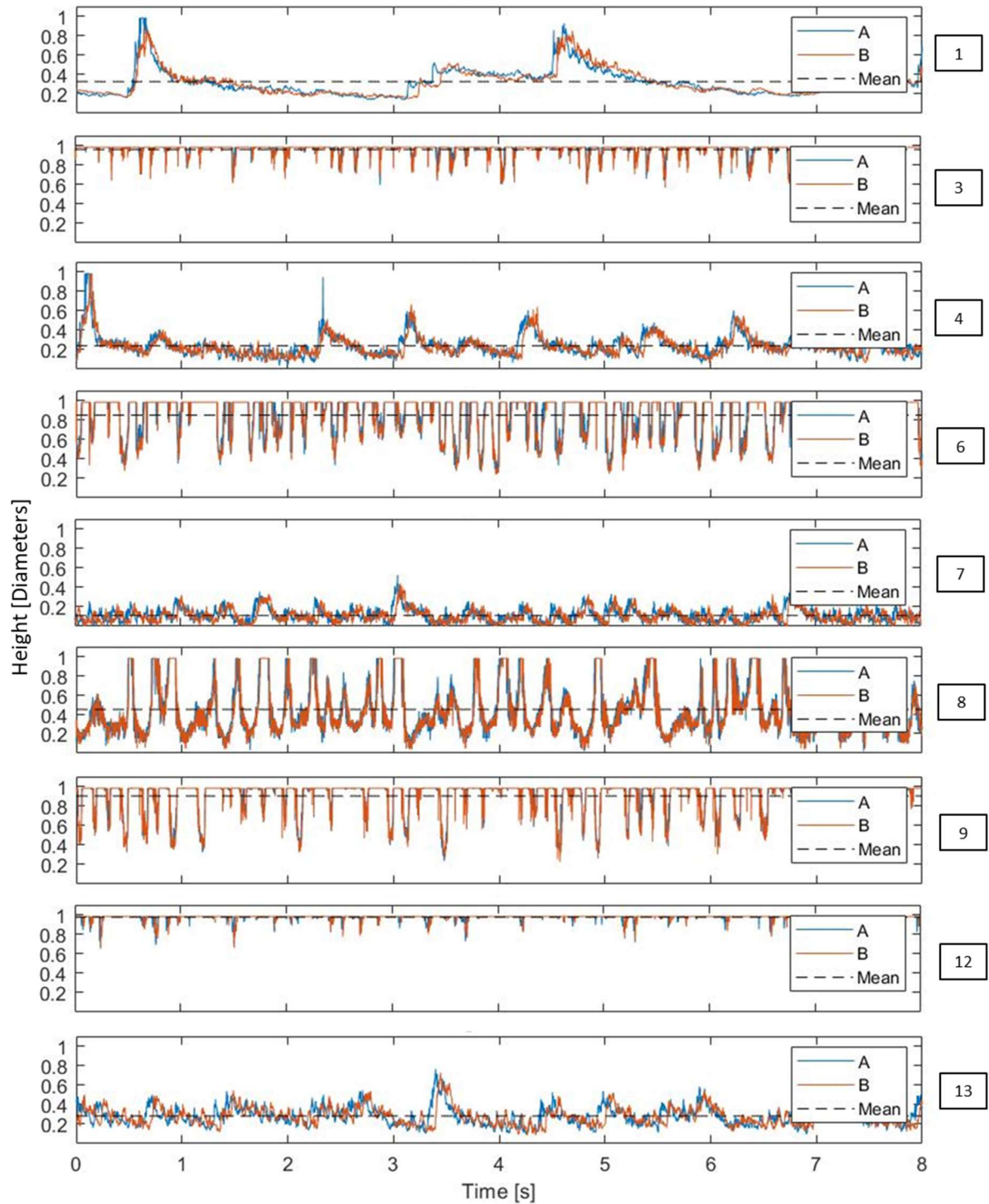
Appendix 2 – Height over time and video integration comparison.

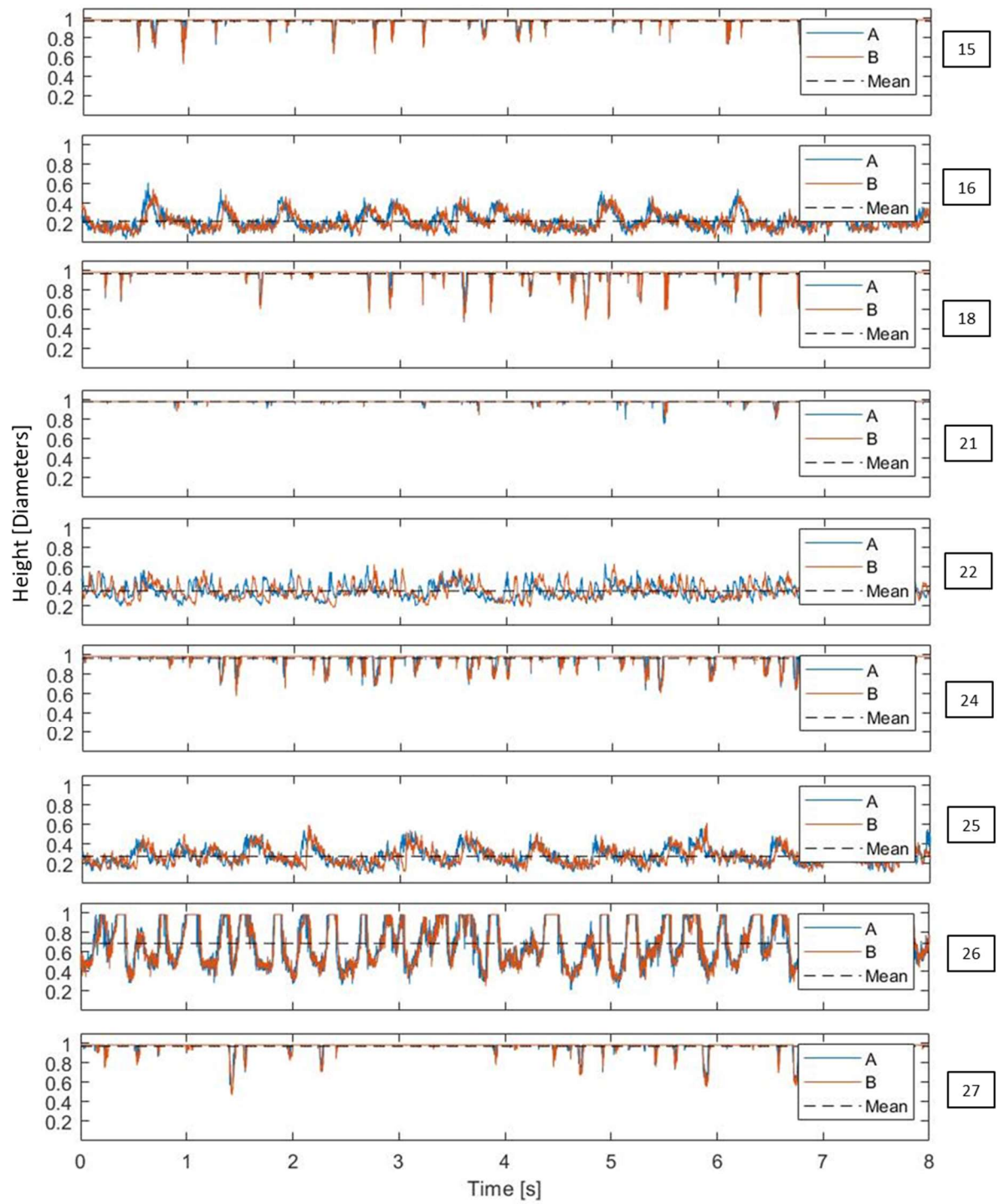


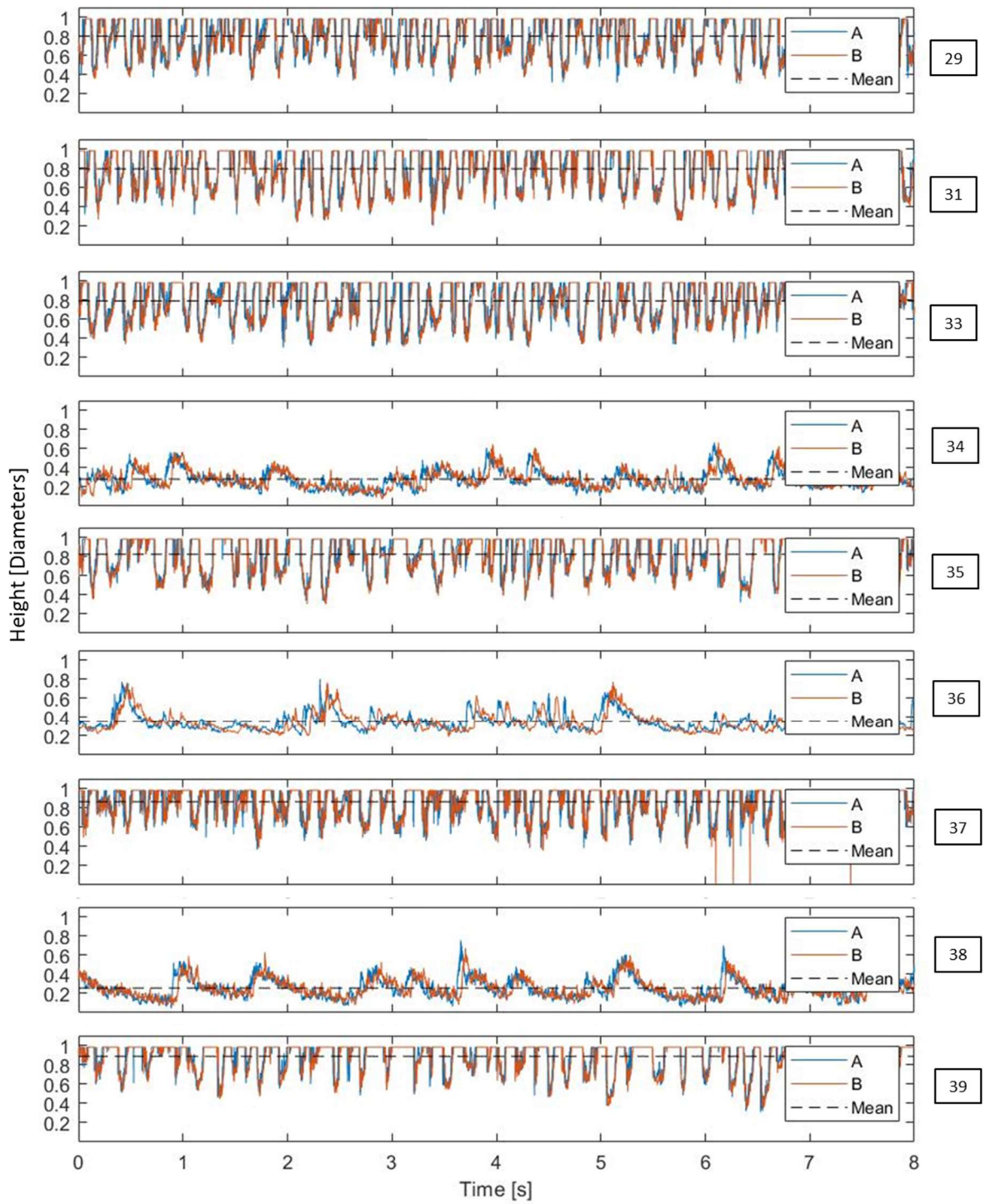




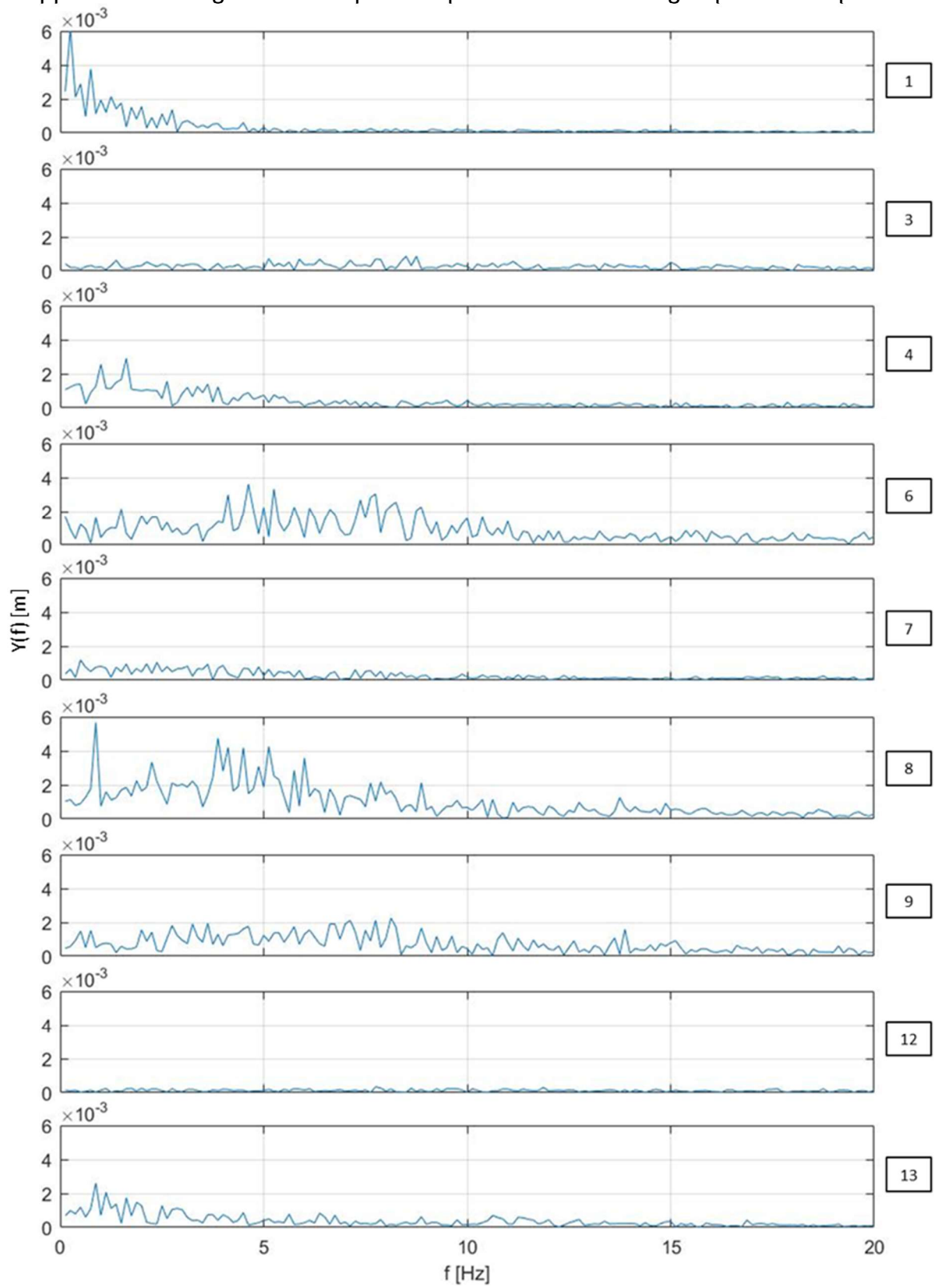
Appendix 3 – Height A and B over time of remaining experimental points.

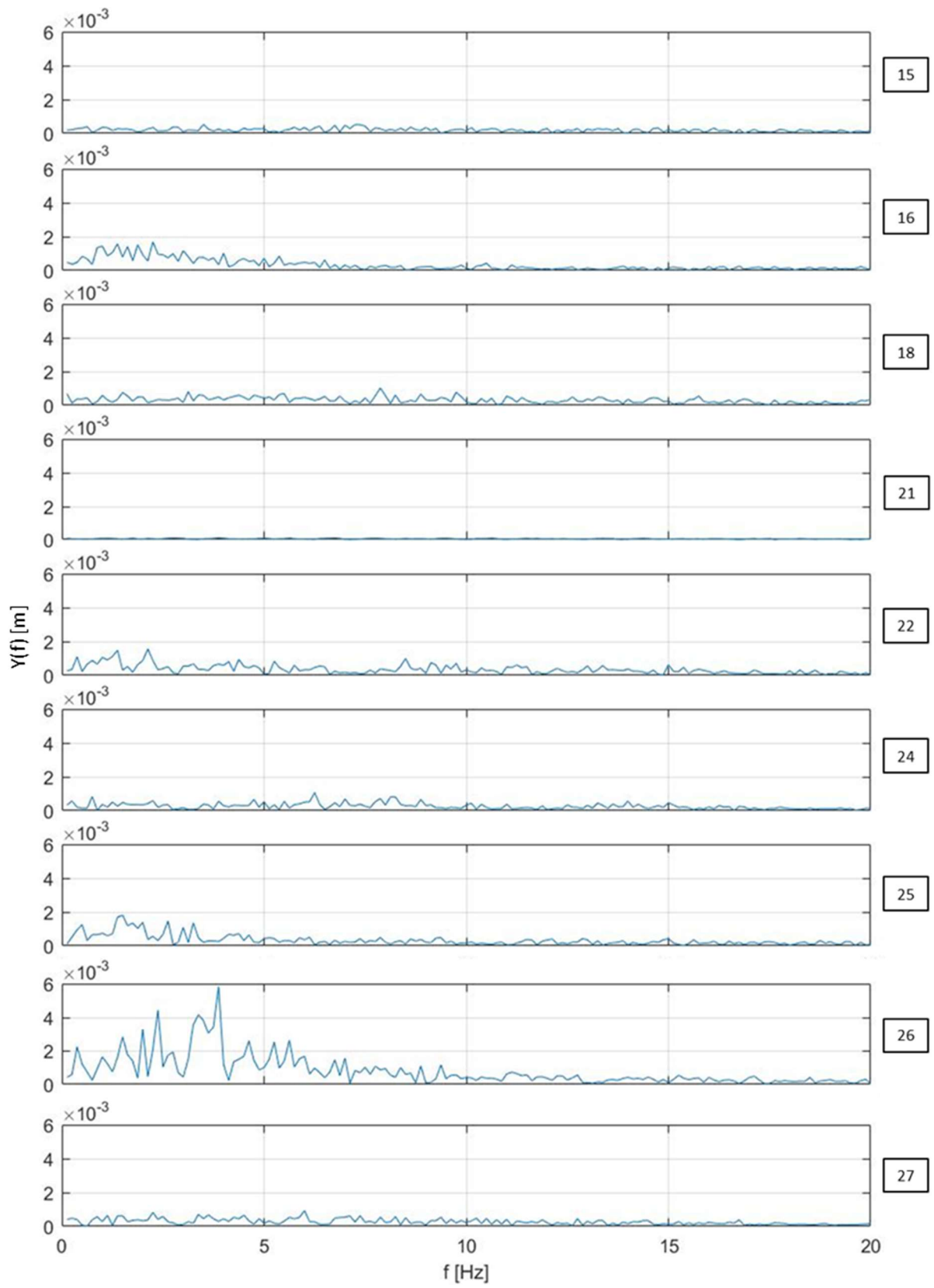


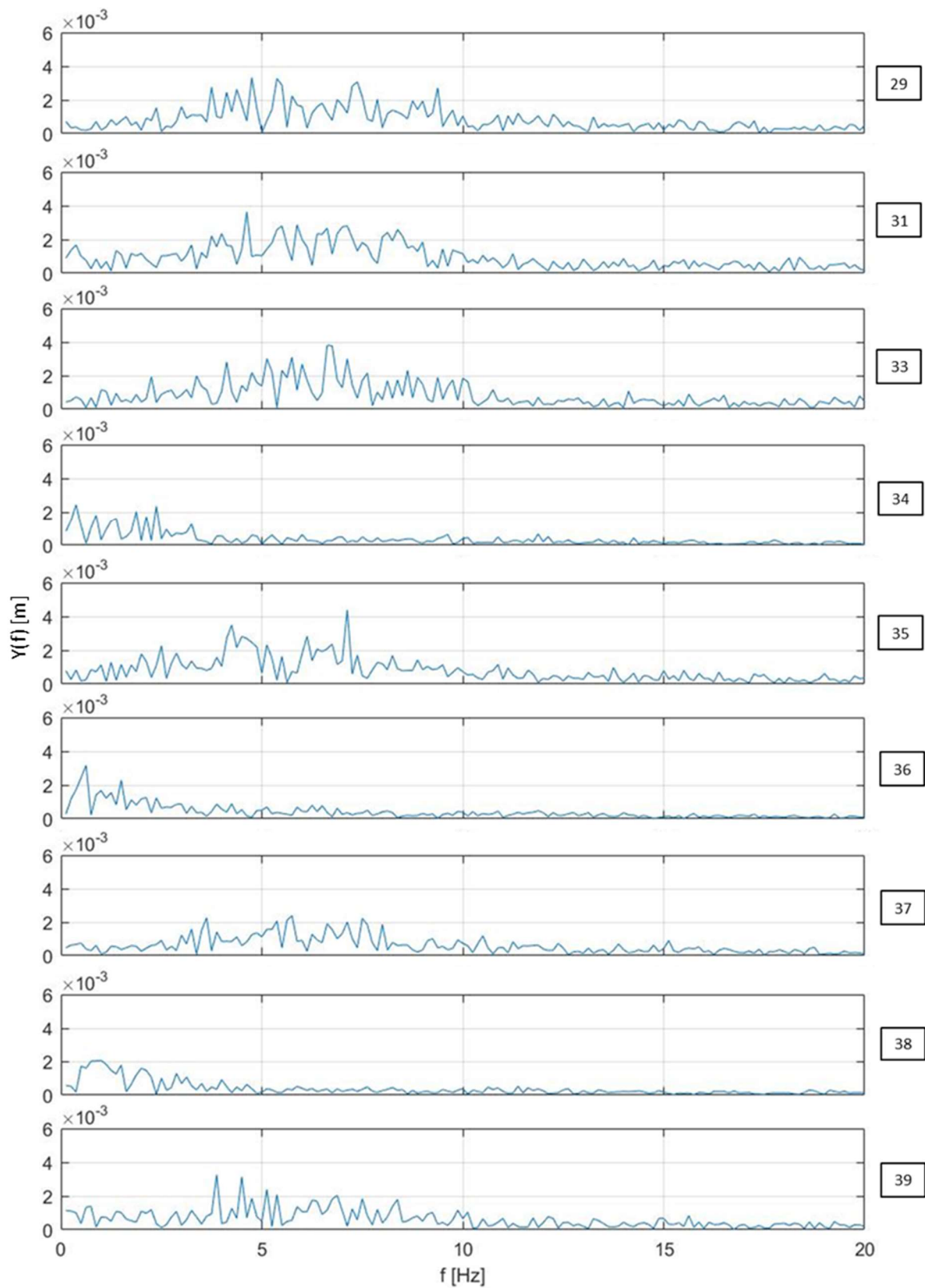




Appendix 4 – Single-sided amplitude spectrum of remaining experimental points.







Appendix 5 – Power spectral density PSD of remaining experimental points.

